

**A NEW SENSOR CONCEPT FOR SIMULTANEOUS MEASUREMENT
OF PRESSURE, TEMPERATURE AND THICKNESS OF PLATE
STRUCTURES USING MODIFIED WAVE PROPAGATION THEORY**

A Thesis

by

TZU-WEI LO

Submitted to the Office of Graduate Studies of
Texas A&M University
in partial fulfillment of the requirements for the degree of

MASTER OF SCIENCE

August 2005

Major Subject: Mechanical Engineering

**A NEW SENSOR CONCEPT FOR SIMULTANEOUS MEASUREMENT
OF PRESSURE, TEMPERATURE AND THICKNESS OF PLATE
STRUCTURES USING MODIFIED WAVE PROPAGATION THEORY**

A Thesis

by

TZU-WEI LO

Submitted to the Office of Graduate Studies of
Texas A&M University
in partial fulfillment of the requirements for the degree of

MASTER OF SCIENCE

Approved by:

Chair of Committee,	Chii-Der S. Suh
Committee Members,	Won-Jong Kim
	Wayne N. P. Hung
Head of Department,	Dennis L. O'Neal

August 2005

Major Subject: Mechanical Engineering

ABSTRACT

A New Sensor Concept for Simultaneous Measurement of Pressure, Temperature and Thickness of Plate Structures Using Modified Wave Propagation Theory. (August 2005)

Tzu-Wei Lo, B.S., Chang Gung University, Tao-Yuan, Taiwan

Chair of Advisory Committee: Dr. Chii-Der S. Suh

This thesis presents a multi-purpose sensor concept viable for the simultaneous measurement of pressure, temperature and thickness of plate structures. It also establishes the knowledge base necessary for future sensor design. Thermal-Acousto Photonic Non-Destructive Evaluation (TAP-NDE) is employed to remotely initiate and acquire interrogating ultrasonic waves. Parameters including pressure, temperature and plate thickness are determined through exploring the dispersion features of the interrogating waves. A theoretical study is performed, through which a modified wave propagation theory applicable to homogeneous, isotropic, linear elastic materials is formulated along with an associated numerical model. A numerical scheme for solving the model is also developed using FEMLAB, a finite element based PDE solver. Gabor Wavelet Transform (GWT) is employed to map numerical time waveforms into the joint time-frequency domain. Wave time-frequency information enables dispersion curves to be extracted and material pressure, temperature and thickness to be determined. A sensor configuration design integrating the wave generation and sensing components of the proven TAP-NDE technology is also developed.

Conclusions of the research are drawn from wave dispersion obtained corresponding to the following ranges of parameters: 300-500kHz for frequency, 25-300°C for temperature, 1-3mm for plate thickness, and $1 \times 10^6 - 1 \times 10^7$ N/m for pressure. Each of the three parameters considered in the study has a different level of impact on plate wave dispersion. Plate thickness is found to have the most impact on wave dispersion, followed by temperature of the plate. The effect attributable to pressure is the least prominent among the three parameters considered. Plate thickness and temperature can be readily measured while simultaneously resolved using dispersion curves. However, pressure variation can only be differentiated when the plate is smaller than 1mm in

thickness. It is observed that the thicker the plate, the faster the frequency group velocity. Also, the group velocities of all frequency components considered are seen to increase with increasing temperature, but decrease with increasing pressure.

ACKNOWLEDGEMENTS

I would like to express my deepest gratitude to my thesis advisor, Dr. Chii-Der S. Suh, who inspired me with the desire to develop independent research ability. I am also grateful to my thesis committee members - Dr. Won-Jong Kim and Dr. Wayne Hung for their advice and support. Finally, I would like to express my deepest gratitude to my parents and Tsai Yu for their love, understanding and support.

TABLE OF CONTENTS

		Page
ABSTRACT		ii
ACKNOWLEDGEMENTS		v
TABLE OF CONTENTS		vi
LIST OF FIGURES		viii
LIST OF TABLES		xiv
CHAPTER		
I	INTRODUCTION	1
	1.1. Overview	1
	1.2. Thesis Objective	5
	1.3. Thesis Organization	6
II	LASER-OPTIC SYSTEM FOR WAVE GENERATION AND ACQUISITION	7
	2.1. Laser Actuator for Wave Generation	8
	2.2. Fiber Tip Interferometer and a Data Acquisition System	9
III	CONCEPTUAL SENSOR DESIGN	13
	3.1. Need Analysis	13
	3.2. Concept Design	20
	3.3. Final Design	30
IV	MODIFIED FORMULATION OF WAVE PROPAGATION	38
	4.1. Classical Theory of Wave Propagation	38
	4.2. Wavelet Transform	46
	4.3. Modified Equations of Wave Propagation for 2-D, Isotropic, Homogenous Materials	54
	4.4. 2D Theoretical Model	61
	4.5. Summary	63
V	FEMLAB BASED FINITE ELEMENT PLATE WAVE MODEL	64
	5.1. Introduction to FEMLAB	64
	5.2. Model Description	64
	5.3. Forcing Functions for Excitation	69
	5.4. Summary	70
VI	RESULTS OF NUMERICAL INVESTIGATION	73
	6.1. Waveforms as Functions of Pressure	73
	6.2. Waveforms as Functions of Temperature	80
	6.3. Waveforms as Functions of Plate Thickness	85

CHAPTER	Page
6.4. Extraction of Dispersion Curves	91
6.5. Wave Dispersion at Different Pressures	94
6.6. Wave Dispersion at Different Temperatures	101
6.7. Wave Dispersion at Different Thicknesses	106
6.8. Discussions	113
6.9. Summary	116
VII CONCLUSIONS AND FUTURE WORK.....	117
REFERENCES	120
VITA.....	122

LIST OF FIGURES

	Page
Fig. 1.1. Aircraft wing	2
Fig. 1.2. Pressurized chemical tank	2
Fig. 2.1. TAP-NDE.....	8
Fig. 2.2. Laser actuator for wave generation	9
Fig. 2.3. Fiber Tip Interferometer (FTI) system for wave acquisition	11
Fig. 2.4. Data acquisition system.....	12
Fig. 3.1. Multimode patch cable connector (THORLAB Inc.).....	15
Fig. 3.2. GRIN fiber collimator (THORLAB Inc.).....	16
Fig. 3.3. Overall function structure.....	18
Fig. 3.4. Function 1 diagram.....	19
Fig. 3.5. Function 2 diagram.....	19
Fig. 3.6. Function 3 diagram.....	20
Fig. 3.7. Sensor head-concept 1	21
Fig. 3.8. Sensor head-concept 2.....	23
Fig. 3.9. Sensor arm-concept 1	23
Fig. 3.10. Sensor arm-concept 2	24
Fig. 3.11. Sensor arm – concept 3.....	25
Fig. 3.12. Sensor foot-concept 1	26
Fig. 3.13. Sensor foot-concept 2.....	27
Fig. 3.14. Boundary conditions of vertical alignment wheel.....	31
Fig. 3.15. Vertical alignment wheel displacement distribution	31
Fig. 3.16. Vertical alignment wheel factor of safety distribution	32
Fig. 3.17. Boundary conditions of neck gear	33
Fig. 3.18. Neck gear displacement distribution	33
Fig. 3.19. Neck gear factor of safety distribution	34
Fig. 3.20. Boundary conditions of sensor base	35
Fig. 3.21. Sensor base displacement distribution.....	35
Fig. 3.22. Sensor base factor of safety distribution.....	36
Fig. 3.23. The final design configuration of sensor body	37

	Page
Fig. 4.1. Stress components of a stress cube.....	39
Fig. 4.2. Thin plate configuration.....	41
Fig. 4.3. Symmetric and anti-symmetric modes.....	44
Fig. 4.4. Lamb waveform acquired at 15mm from the excitation point.....	45
Fig. 4.5. Lamb waveform acquired at 25mm from the excitation point.....	46
Fig. 4.6. Lamb waveform acquired at 35mm from the excitation point.....	46
Fig. 4.7. Gabor wavelet function corresponds to $a=1$ and $b=0$	48
Fig. 4.8. Gabor wavelet function corresponds to $a=1$ and $b=1$	48
Fig. 4.9. Gabor wavelet function corresponds to $a=0.5$ and $b=0$	49
Fig. 4.10. Gabor Wavelet Function consists of a complex-valued sinusoidal.....	50
Fig. 4.11. Signal A with the sum of two frequencies: 1 Hz and 2 Hz during a time span of 5 seconds.....	51
Fig. 4.12. Signal B during two intervals: 1 Hz from 0-3 second and 2 Hz from 3-5 seconds.....	52
Fig. 4.13. Fourier transform of signal A.....	52
Fig. 4.14. Gabor wavelet transform of signal A.....	53
Fig. 4.15. Fourier transform of signal B.....	53
Fig. 4.16. Gabor wavelet transform of signal B.....	54
Fig. 4.17. Three different states in cartesian coordinate system.....	55
Fig. 5.1. Simplified plate model.....	66
Fig. 5.2. 2-D numerical plate model with forcing conditions.....	66
Fig. 5.3. Boundary conditions for static model.....	68
Fig. 5.4. Boundary conditions for transient model.....	68
Fig. 5.5. Triangular meshes in model.....	69
Fig. 5.6. Gaussian forcing function.....	70
Fig. 6.1. Waveforms of three different pressures at $d=1\text{mm}$ and $T=25^{\circ}\text{C}$	74
Fig. 6.2. Waveforms of three different pressures at $d=1\text{mm}$ and $T=50^{\circ}\text{C}$	74
Fig. 6.3. Waveforms of three different pressures at $d=1\text{mm}$ and $T=100^{\circ}\text{C}$	75
Fig. 6.4. Waveforms of three different pressures at $d=1\text{mm}$ and $T=300^{\circ}\text{C}$	75
Fig. 6.5. Waveforms of three different pressures at $d=1.5\text{mm}$ and $T=25^{\circ}\text{C}$	76

	Page
Fig. 6.6. Waveforms of three different pressures at $d=1.5\text{mm}$ and $T=50^\circ\text{C}$	76
Fig. 6.7. Waveforms of three different pressures at $d=1.5\text{mm}$ and $T=100^\circ\text{C}$	77
Fig. 6.8. Waveforms of three different pressures at $d=1.5\text{mm}$ and $T=300^\circ\text{C}$	77
Fig. 6.9. Waveforms of three different pressures at $d=2.0\text{mm}$ and $T=25^\circ\text{C}$	78
Fig. 6.10. Waveforms of three different pressures at $d=2.0\text{mm}$ and $T=50^\circ\text{C}$	78
Fig. 6.11. Waveforms of three different pressures at $d=2.0\text{mm}$ and $T=100^\circ\text{C}$	79
Fig. 6.12. Waveforms of three different pressures at $d=2.0\text{mm}$ and $T=300^\circ\text{C}$	79
Fig. 6.13. Waveforms of four different temperatures at $d=1.0\text{mm}$ and $P=1 \times 10^6 \text{ N/m}$	80
Fig. 6.14. Waveforms of four different temperatures at $d=1.0\text{mm}$ and $P=5 \times 10^6 \text{ N/m}$..	81
Fig. 6.15. Waveforms of four different temperatures at $d=1.0\text{mm}$ and $P=1 \times 10^7 \text{ N/m}$... 81	81
Fig. 6.16. Waveforms of four different temperatures at $d=1.5\text{mm}$ and $P=1 \times 10^6 \text{ N/m}$... 82	82
Fig. 6.17. Waveforms of four different temperatures at $d=1.5\text{mm}$ and $P=5 \times 10^6 \text{ N/m}$.. 82	82
Fig. 6.18. Waveforms of four different temperatures at $d=1.5\text{mm}$ and $P=1 \times 10^7 \text{ N/m}$... 83	83
Fig. 6.19. Waveforms of four different temperatures at $d=2.0\text{mm}$ and $P=1 \times 10^6 \text{ N/m}$... 83	83
Fig. 6.20. Waveforms of four different temperatures at $d=2.0\text{mm}$ and $P=5 \times 10^6 \text{ N/m}$.. 84	84
Fig. 6.21. Waveforms of four different temperatures at $d=2.0\text{mm}$ and $P=1 \times 10^7 \text{ N/m}$... 84	84
Fig. 6.22. Waveforms of three different thicknesses at $T=25^\circ\text{C}$ and $P=1 \times 10^6 \text{ N/m}$ 85	85
Fig. 6.23. Waveforms of three different thicknesses at $T=25^\circ\text{C}$ and $P=5 \times 10^6 \text{ N/m}$ 86	86
Fig. 6.24. Waveforms of three different thicknesses at $T=25^\circ\text{C}$ and $P=1 \times 10^7 \text{ N/m}$ 86	86
Fig. 6.25. Waveforms of three different thicknesses at $T=50^\circ\text{C}$ and $P=1 \times 10^6 \text{ N/m}$ 87	87
Fig. 6.26. Waveforms of three different thicknesses at $T=50^\circ\text{C}$ and $P=5 \times 10^6 \text{ N/m}$ 87	87
Fig. 6.27. Waveforms of three different thicknesses at $T=50^\circ\text{C}$ and $P=1 \times 10^7 \text{ N/m}$ 88	88
Fig. 6.28. Waveforms of three different thicknesses at $T=100^\circ\text{C}$ and $P=1 \times 10^6 \text{ N/m}$ 88	88
Fig. 6.29. Waveforms of three different thicknesses at $T=100^\circ\text{C}$ and $P=5 \times 10^6 \text{ N/m}$ 89	89
Fig. 6.30. Waveforms of three different thicknesses at $T=100^\circ\text{C}$ and $P=1 \times 10^7 \text{ N/m}$ 89	89
Fig. 6.31. Waveforms of three different thicknesses at $T=300^\circ\text{C}$ and $P=1 \times 10^6 \text{ N/m}$ 90	90
Fig. 6.32. Waveforms of three different thicknesses at $T=300^\circ\text{C}$ and $P=5 \times 10^6 \text{ N/m}$ 90	90
Fig. 6.33. Waveforms of three different thicknesses at $T=300^\circ\text{C}$ and $P=1 \times 10^7 \text{ N/m}$ 91	91

Fig. 6.34. Numerical waveform at position 1 corresponds to $P=1 \times 10^6$ N/m, T=25°C and d=1 mm	92
Fig. 6.35. Numerical waveform at position 2 corresponds to $P=1 \times 10^6$ N/m, T=25°C and d=1 mm	93
Fig. 6.36. GWT of the waveform in Fig. 6.34	93
Fig. 6.37. GWT of the waveform in Fig. 6.35	94
Fig. 6.38. Dispersion curves for three different pressures at d=1.0mm and T=25°C	95
Fig. 6.39. Dispersion curves for three different pressures at d=1.0mm and T=50°C	96
Fig. 6.40. Dispersion curves for three different pressures at d=1.0mm and T=100°C	96
Fig. 6.41. Dispersion curves for three different pressures at d=1.0mm and T=300°C	97
Fig. 6.42. Dispersion curves for three different pressures at d=1.5mm and T=25°C	97
Fig. 6.43. Dispersion curves for three different pressures at d=1.5mm and T=50°C	98
Fig. 6.44. Dispersion curves for three different pressures at d=1.5mm and T=100°C	98
Fig. 6.45. Dispersion curves for three different pressures at d=1.5mm and T=300°C	99
Fig. 6.46. Dispersion curves for three different pressures at d=2.0mm and T=25°C	99
Fig. 6.47. Dispersion curves for three different pressures at d=2.0mm and T=50°C	100
Fig. 6.48. Dispersion curves for three different pressures at d=2.0mm and T=100°C	100
Fig. 6.49. Dispersion curves for three different pressures at d=2.0mm and T=300°C	101
Fig. 6.50. Dispersion curves for four different temperatures at d=1.0mm and P=1 × 10 ⁶ N/m.....	102
Fig. 6.51. Dispersion curves for four different temperatures at d=1.0mm and P=5 × 10 ⁶ N/m	102
Fig. 6.52. Dispersion curves for four different temperatures at d=1.0mm and P=1 × 10 ⁷ N/m.....	103
Fig. 6.53. Dispersion curves for four different temperatures at d=1.5mm and P=1 × 10 ⁶ N/m.....	103
Fig. 6.54. Dispersion curves for four different temperatures at d=1.5mm and P=5 × 10 ⁶ N/m	104

Fig. 6.55. Dispersion curves for four different temperatures at $d=1.5\text{mm}$ and $P=1 \times 10^7 \text{ N/m}$	104
Fig. 6.56. Dispersion curves for four different temperatures at $d=2.0\text{mm}$ and $P=1 \times 10^6 \text{ N/m}$	105
Fig. 6.57. Dispersion curves for four different temperatures at $d=2.0\text{mm}$ and $P=5 \times 10^6 \text{ N/m}$	105
Fig. 6.58. Dispersion curves for four different temperatures at $d=2.0\text{mm}$ and $P=1 \times 10^7 \text{ N/m}$	106
Fig. 6.59. Dispersion curves for three different thicknesses at $T=25^\circ\text{C}$ and $P=1 \times 10^6 \text{ N/m}$	107
Fig. 6.60. Dispersion curves for three different thicknesses at $T=25^\circ\text{C}$ and $P=5 \times 10^6 \text{ N/m}$	107
Fig. 6.61. Dispersion curves for three different thicknesses at $T=25^\circ\text{C}$ and $P=1 \times 10^7 \text{ N/m}$	108
Fig. 6.62. Dispersion curves for three different thicknesses at $T=50^\circ\text{C}$ and $P=1 \times 10^6 \text{ N/m}$	108
Fig. 6.63. Dispersion curves for three different thicknesses at $T=50^\circ\text{C}$ and $P=5 \times 10^6 \text{ N/m}$	109
Fig. 6.64. Dispersion curves for three different thicknesses at $T=50^\circ\text{C}$ and $P=1 \times 10^7 \text{ N/m}$	109
Fig. 6.65. Dispersion curves for three different thicknesses at $T=100^\circ\text{C}$ and $P=1 \times 10^6 \text{ N/m}$	110
Fig. 6.66. Dispersion curves for three different thicknesses at $T=100^\circ\text{C}$ and $P=5 \times 10^6 \text{ N/m}$	110
Fig. 6.67. Dispersion curves for three different thicknesses at $T=100^\circ\text{C}$ and $P=1 \times 10^7 \text{ N/m}$	111
Fig. 6.68. Dispersion curves for three different thicknesses at $T=300^\circ\text{C}$ and $P=1 \times 10^6 \text{ N/m}$	111

Fig. 6.69. Dispersion curves for three different thicknesses at $T=300^{\circ}\text{C}$ and $P=5 \times 10^6 \text{ N/m}$	112
Fig. 6.70. Dispersion curves for three different thicknesses at $T=300^{\circ}\text{C}$ and $P=1 \times 10^7 \text{ N/m}$	112
Fig. 6.71. All 36 dispersion curves extracted from both positions 1 and 2	114
Fig. 6.72. All 36 dispersion curves extracted position 1 only.....	115
Fig. 6.73. All 36 dispersion curves extracted position 2 only.....	115

LIST OF TABLES

	Page
Table 3.1. Sensor head selection matrix	28
Table 3.2. Sensor arm selection matrix.....	28
Table 3.3. Sensor foot selection matrix	28
Table 3.4. Aluminum alloy 6061 material properties.....	29
Table 5.1. Material properties of aluminum alloy 6061-T6.....	67
Table 5.2. Different combinations of parameters	71

CHAPTER I

INTRODUCTION

1.1. Overview

High material stresses could bring about catastrophic results as severe as aircraft crashes or chemical tank explosion. It is important to understand the causes of these incidents in order to prevent future catastrophes. Extensive investigations show that variations in both temperature and pressure are the driving force behind the forming of high stress magnitudes. Fig. 1.1 shows an airplane wing with outer pressure acting on it, and Fig. 1.2 shows a chemical tank with internal pressure acting on it. Failures can also result from hidden corrosion that weakens the integrity of structures. Therefore, to be able detect environmental parameters including pressure, temperature and thickness is a very important issue to avoid structural break-down. Implementing sensors is necessary to address the current status of equipment. Most traditional sensors were designed to detect these parameters by contacting a measured object directly such as piezoelectric transducer sensor, and often had destructive qualities. Additionally, these sensors are usually designed for one parameter of measurement only. For example, strain gage can only measure the stresses of an object. In order to overcome these disadvantages associated with the traditional sensors, a new generation of sensor for detecting multi-parameters without contacting or invading the measured object will be more effective and desirable. To develop a new conceptual sensor is the goal of this research.

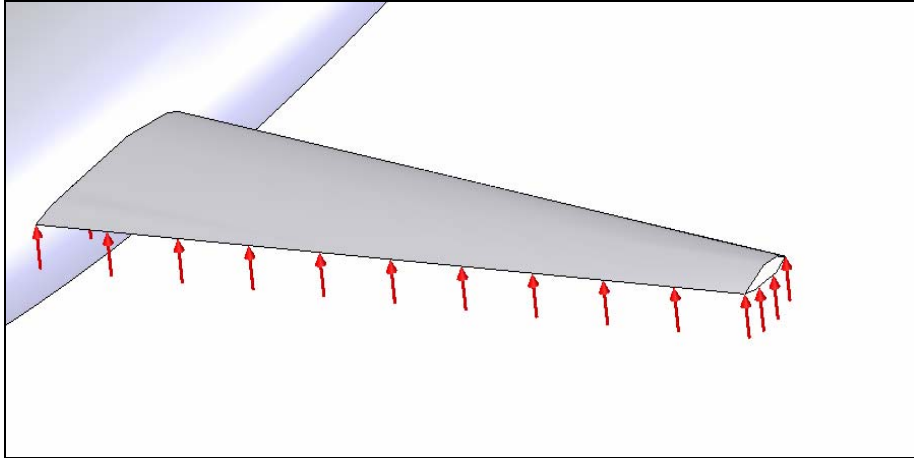


Fig. 1.1. Aircraft wing

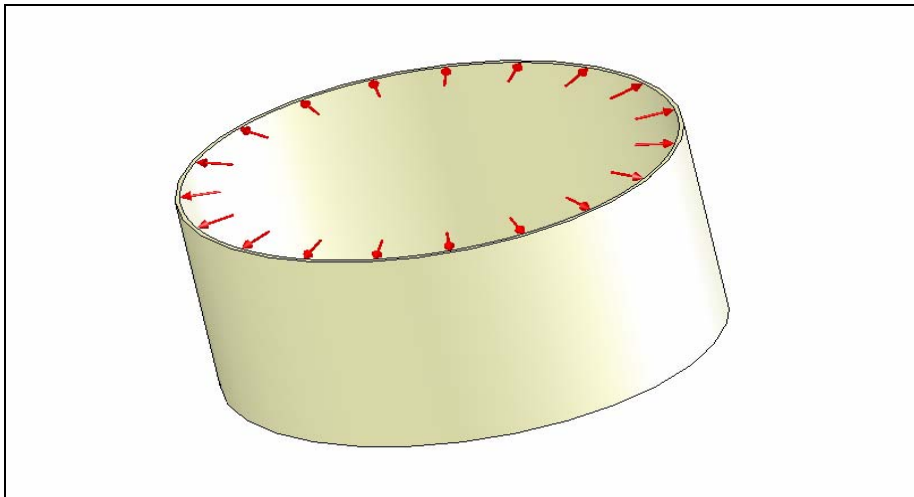


Fig. 1.2. Pressurized chemical tank

An ultrasonic testing method is considered as a way to achieve this goal. In nondestructive evaluation (NDE) [1], the ultrasonic testing method is one of the most widely used techniques. The general idea of ultrasonic testing is to generate propagating ultrasonic wave in the measured object and acquire the wave at a certain distance. These waves are observed to determine material defects, flaws, or environmental parameters. However, the traditional ultrasonic testing sensors always use contacting transducers as actuators for wave generation or receivers for wave acquisition [2]. In this way, the

transducers must be attached to the measured object, thus resulting in a change of state of the measured object and errors in acquired data waveform. Hence, an alternative approach to generate and acquire waves without contacting the measured object is needed. Laser-optical method is one of the NDE techniques that has been successfully applied to profile the thermal state of silicon wafers [3,4,5], to evaluate different thin films material properties [6], to determine the material properties of microstructures [7] and to inspect solder joint defects in flip-chips [8]. A laser-optical technique referred to as the Thermo-Acoustic-Photonic Non-Destructive Evaluation (TAP-NDE) [9] will be adopted to achieve the objectives of the study. TAP-NDE consists of a pulsed Nd:YAG laser for wave generation, fiber tip interferometers (FTIs) for wave acquisition and a PC based data acquisition system. FTI was developed by Burger and his colleagues [10] at Texas A&M University. By applying TAP-NDE technique, a non-contact, non-destructive and multi parameters sensor may be realized. To this end, the correlations of laser-induced ultrasonic waves with environmental parameters will need to be established.

In this thesis, the correlation of ultrasonic waves with multi-environmental parameters; namely, thickness, pressure and temperature of a plate will be studied. In the classical wave propagation theory [11], the ultrasonic wave that propagates in thin structures whose thickness is small compared with length and width is called a Lamb wave. In the past, Lamb waves have been successfully applied to identify damages of plates [12,13]. Lamb waves are dispersive and Lamb dispersion is highly sensitive to the variations of environmental parameters. For example, Lamb dispersion had been successfully explored to measure the thermal state of silicon wafers subject to rapid temperature ramp-ups [4] and the spatial variations of aircraft structures [14]. However, reports on the effect of pressure on wave dispersion are rare. In addition, a theoretical model describing dispersion as functions of pressure needs to be established. Between 1960 and 2000, many research contributions [15] have proven that wave responses are affected by initial stresses fields regardless if the material is incompressible or not. For example, Chai [16] determined the surface wave velocities in a pre-stress anisotropic solid, Rogerson [17] developed a surface wave model for a slightly compressible, finitely deformed elastic media, and Prikazchikov [18] developed a model that enables the

propagation of surface waves in incompressible, transversely isotropic, pre-stressed elastic half-space to be studied.

A modified theoretical model for wave propagation in thin structures subject to simultaneous temperature effect and pre-stresses is formulated. Using the relation between pre-stresses and pressure, waveforms associated with pressure can be obtained. However, it is difficult to solve the modified theoretical model directly. As an alternative, the finite element method (FEM) is appealed to establishing numerical solutions. Specifically, the many powerful features of the commercially available FEM tool, FEMLAB, will be explored. In order to address the response of the thin aircraft wing structure as shown in Fig. 1, the corresponding numerical model can be an idealized flat plate subject to different uniform temperatures, thicknesses and pressures. Resulted numerical waveforms will then be processed using Gabor wavelet transform to extract dispersion information as functions of temperature, pressure and plate thickness.

Wavelet transform is a mathematical transformation that maps time signals into the orthogonal time-frequency domain [19,20]. In order to obtain dispersion information, numerical time waveforms need be resolved in the time-frequency domain. The thesis will adopt the same method that was well documented for the processing of broadband, dispersive waves [21-23]. Since temperature, pressure or thickness changes lead to the changes of wave dispersion; conversely, changes in dispersion are therefore a good indication temperature, pressure or thickness variations. As such, the thermal, pressure and spatial changes of a plate can be simultaneously established via the deployment of interrogating elastic waves.

Knowledge base established in exploring wave dispersion for the determination of pressure, temperature and thickness will then be used to develop a sensor concept. Common design methodologies including need analysis, conceptual design and embodiment design will be followed. In need analysis, all functions required of the sensor design, along with associated design parameters and constraints, will be identified and organized into a hierarchy function structure. The function structure will enable multitude innovative, viable concepts to be formulated. A selection matrix will then be used to evaluate all the developed concepts and to identify one for further design embodiment. In embodiment, a final design configuration will be developed. The final

configuration will be analyzed and optimized using COSMOSWorks and its feasibility will be demonstrated.

1.2. Thesis Objective

The objective of the thesis is to develop a multi-purpose sensor concept for the simultaneous measurement of temperature, pressure and thickness in thin structure. The knowledge base needed for the successful development of such a sensor will be established through the three sequential tasks as follow: (1) formulate a modified wave propagation model that incorporates pre-stress and temperature conditions; (2) develop a corresponding numerical model; and (3) validate the correlation between ultrasonic wave dispersion with temperature, pressure, and thickness. The IIDE design methodologies will be followed to develop several feasible sensor concepts and design software tools including SolidWorks and COSMOSWorks will be employed to demonstrate feasibility. To develop the wave propagation model, considerations for simultaneous pre-stress and thermal effects will be incorporated into the classical theories of elasticity and wave propagation. Since the resulted theoretical model is too complex to suggest close-form solutions, numerical solutions will be attempted instead. To this end, FEMLAB will be used to approximate numerical solutions in response to various boundary and forcing conditions. A Gabor wavelet program will be developed to address Task (3), in which dispersive waves registering mechanical, thermal and spatial changes will be processed for the extraction of temperature, pressure and thickness information.

1.3. Thesis Organization

The need for a multiple-purpose sensor is discussed in Chapter I. TAP-NDE as a viable technology for the characterization of materials are introduced in Chapter II along with its configuration and setup. A sensor concept and the design procedures that will be followed are illustrated in Chapter III. Classical wave theory, definition of dispersion and wavelet transform will be reviewed Chapter IV. A modified wave propagation model will also be derived in the same chapter. Chapter V covers the numerical model along with material properties and boundary and forcing conditions. In Chapter VI numerical results and dispersion curves at different temperatures, thicknesses and pressures are presented in Chapter VI. Finally, Chapter VII summarizes the research endeavor and discusses possible future work.

CHAPTER II

LASER-OPTIC SYSTEM FOR WAVE GENERATION AND ACQUISITION

Thermo-Acousto-Photonic Non-Destructive Evaluation (TAP-NDE) [9] technique was employed for the research. In this chapter, the configuration of TAP-NDE is introduced. The apparatus of TAP-NDE consists of a pulsed laser for ultrasonic wave generation, a dual Fiber Tip Interferometer (FTI) [10] system for wave detection, semiconductor photodetector and a data acquisition system for receiving and converting output signals from the photodetector into digital format. The TAP-NDE system is shown schematically in Fig. 2.1. The components of TAP-NDE will be discussed in the subsequent sections.

2.1. Laser Actuator for Wave Generation

The laser actuator of the sensor concept shown in Fig 2.2 consists of a Nd: YAG laser and an optical fiber which is connected to the sensor body. The pulse width of the pulsed laser which is a Spectra-Physics model DCR-3 Nd:YAG laser is 10 nanoseconds. The maximum single pulse energy from the laser is 1 J at the 1064 nm wavelength. A 532 nm wavelength green light can also be initiated with a harmonic frequency doubler. A pulse of so small a time duration can cause a sharp thermal shock on the surface of the specimen. The induced thermal energy results in out-of-plane surface displacements that propagate out as elastic mechanical waves. However, surface ablation may occur if the energy density levels exceed the ablation threshold of the material. To prevent surface ablation, the spot size of the pulsed laser must be controlled. Laser induced mechanical waves propagate in the specimen and are acquired by the FTI optical sensors.

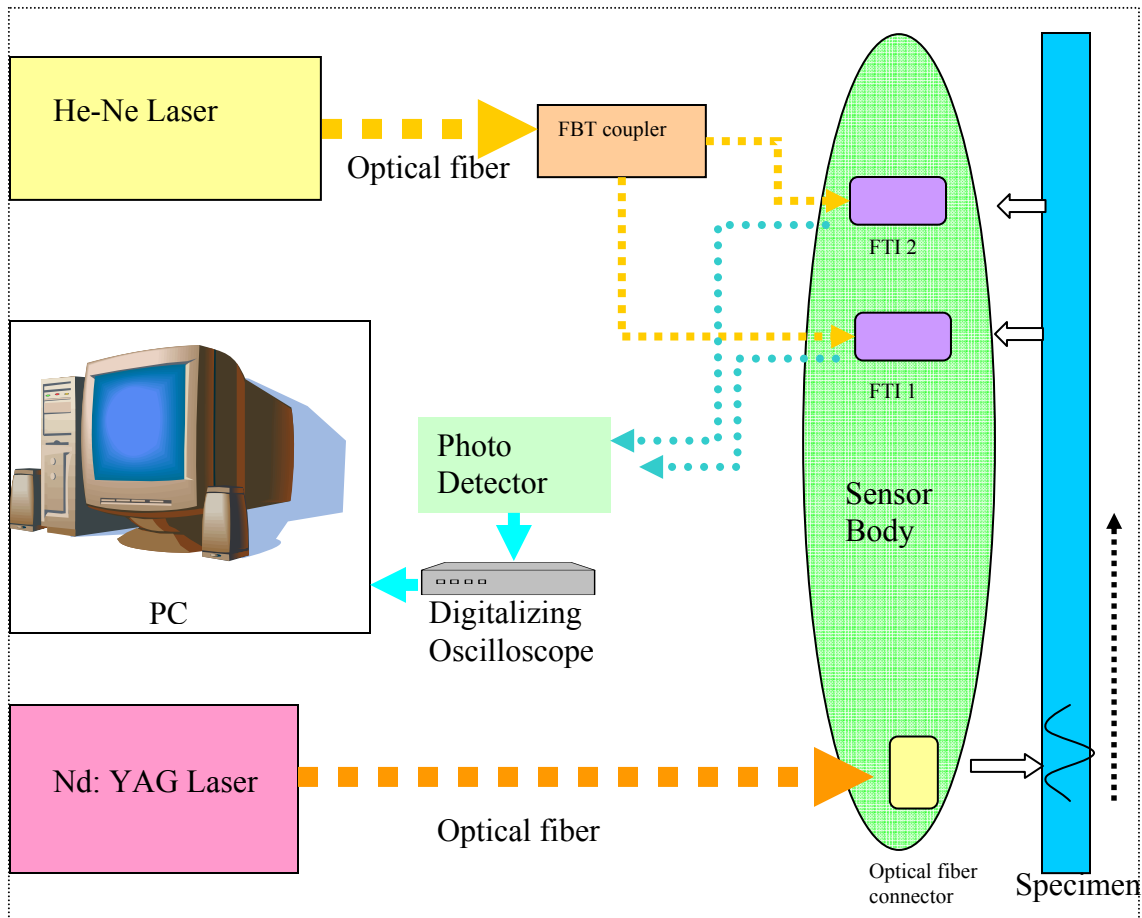


Fig. 2.1. TAP-NDE

2.1. Laser Actuator for Wave Generation

The laser actuator of the sensor concept shown in Fig 2.2 consists of a Nd: YAG laser and an optical fiber which is connected to the sensor body. The pulse width of the pulsed laser which is a Spectra-Physics model DCR-3 Nd:YAG laser is 10 nanoseconds. The maximum single pulse energy from the laser is 1 J at the 1064 nm wavelength. A 532 nm wavelength green light can also be initiated with a harmonic frequency doubler. A pulse of so small a time duration can cause a sharp thermal shock on the surface of the specimen. The induced thermal energy results in out-of-plane surface displacements that propagate out as elastic mechanical waves. However, surface ablation may occur if the energy density levels exceed the ablation threshold of the material. To prevent surface

ablation, the spot size of the pulsed laser must be controlled. Laser induced mechanical waves propagate in the specimen and are acquired by the FTI optical sensors.

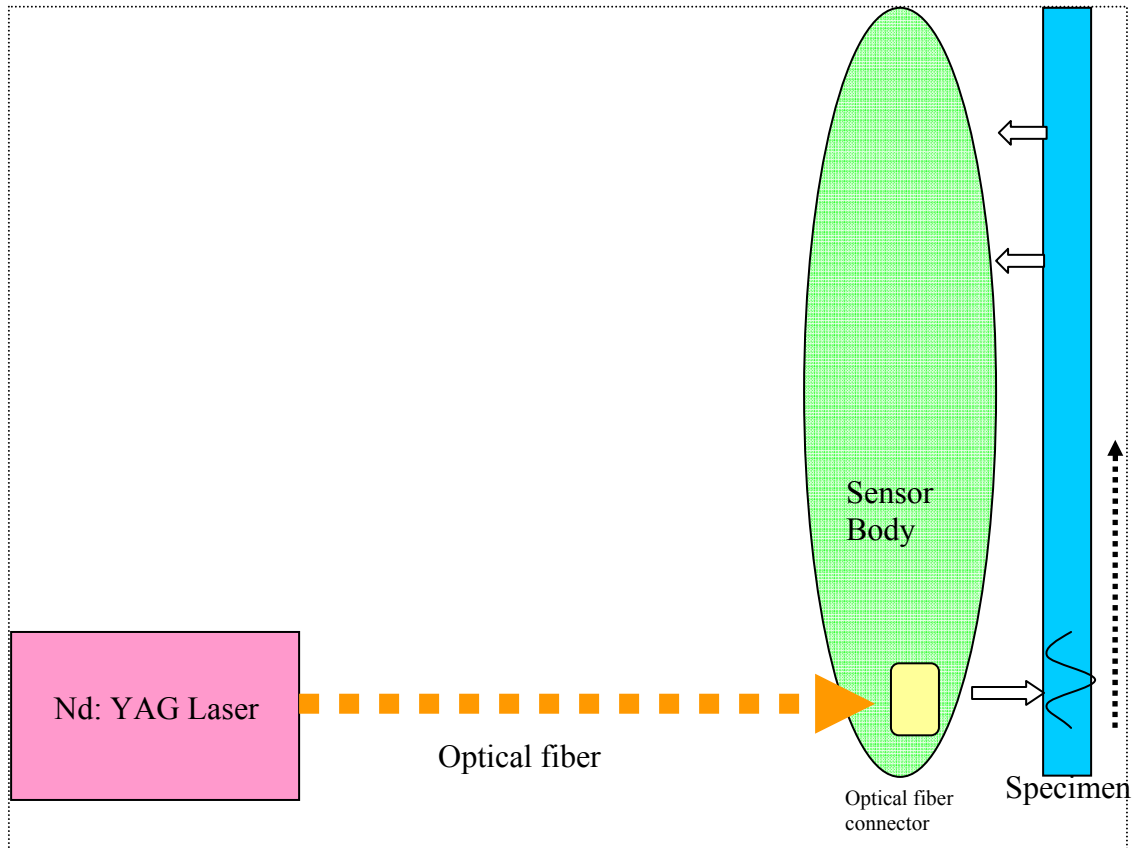


Fig. 2.2. Laser actuator for wave generation

2.2. Fiber Tip Interferometer and a Data Acquisition System

Out of plane displacements resulted from the pulsed laser are detected by a fiber-optic-based, Fizeau type interferometer referred to as the Fiber Tip Interferometer (FTI) [21]. Fig. 2.3 shows a standard Fizeau interferometer. In this research, two FTIs are required because the ultrasonic waves must be detected at two different locations. The FTI sensing system is powered by a 30mJ Ne-Ne laser. The emitted laser beam is split into two separate optical fibers through a Fused Biconical Taper (FBT) coupler. The

GRIN lens used to collect the beam reflected off the object surface is fused to the tip of the optical fiber. When the laser beam reaches the tip of the optical fiber, approximately 4% of the laser beam is sent back into the fiber core as the reference beam. The remaining laser beam leaves the fiber tip, travels through the Fizeau cavity and gets reflected off the surface of the specimen. The small portion of the light re-entering the GRIN lens is called the object beam. The reference beam and the object beam have a constant phase shift which results in an interference pattern that represents the surface displacement of the specimen. This interference pattern can be observed by using a data acquisition system. The data acquisition system shown in Fig. 2.4 includes a photo-detector, a digital oscilloscope, and a computer. The interference pattern is converted into voltaic changes by the photo-detector, which is a broadband device. The voltaic changes are displayed on the digital oscilloscope as waveforms. The digital oscilloscope has a maximum sampling rate of 1GHz per second. Digital data received by the oscilloscope are then transferred to the computer and recorded. After waveform data are obtained, post signal processing is executed to extract dispersion information. From the dispersion information, temperature, pressure and thickness of the specimen are established. Methods for establishing temperature, pressure and thickness of the specimen from wave dispersion will be discussed in Chapter VI.

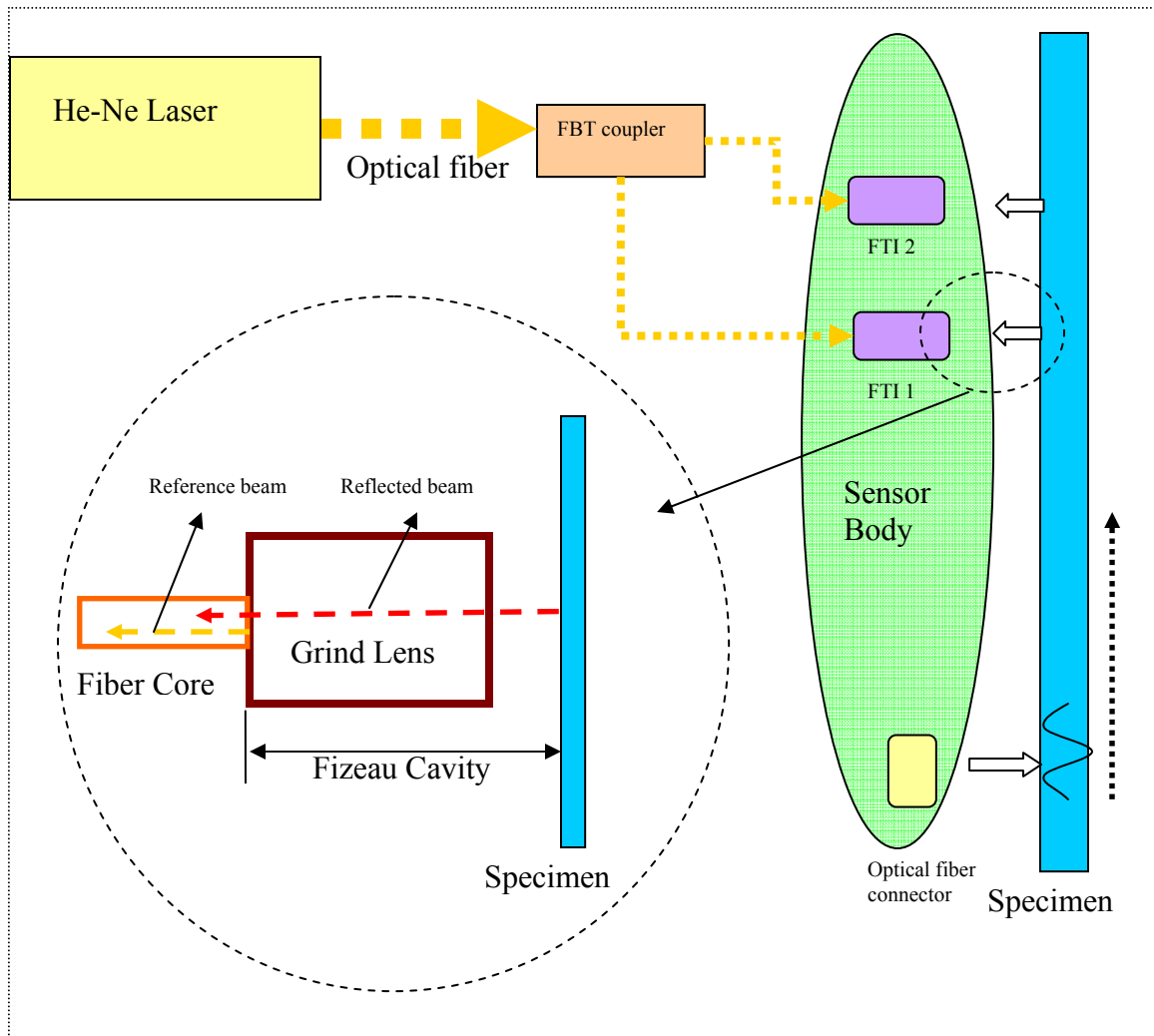


Fig. 2.3. Fiber Tip Interferometer (FTI) system for wave acquisition

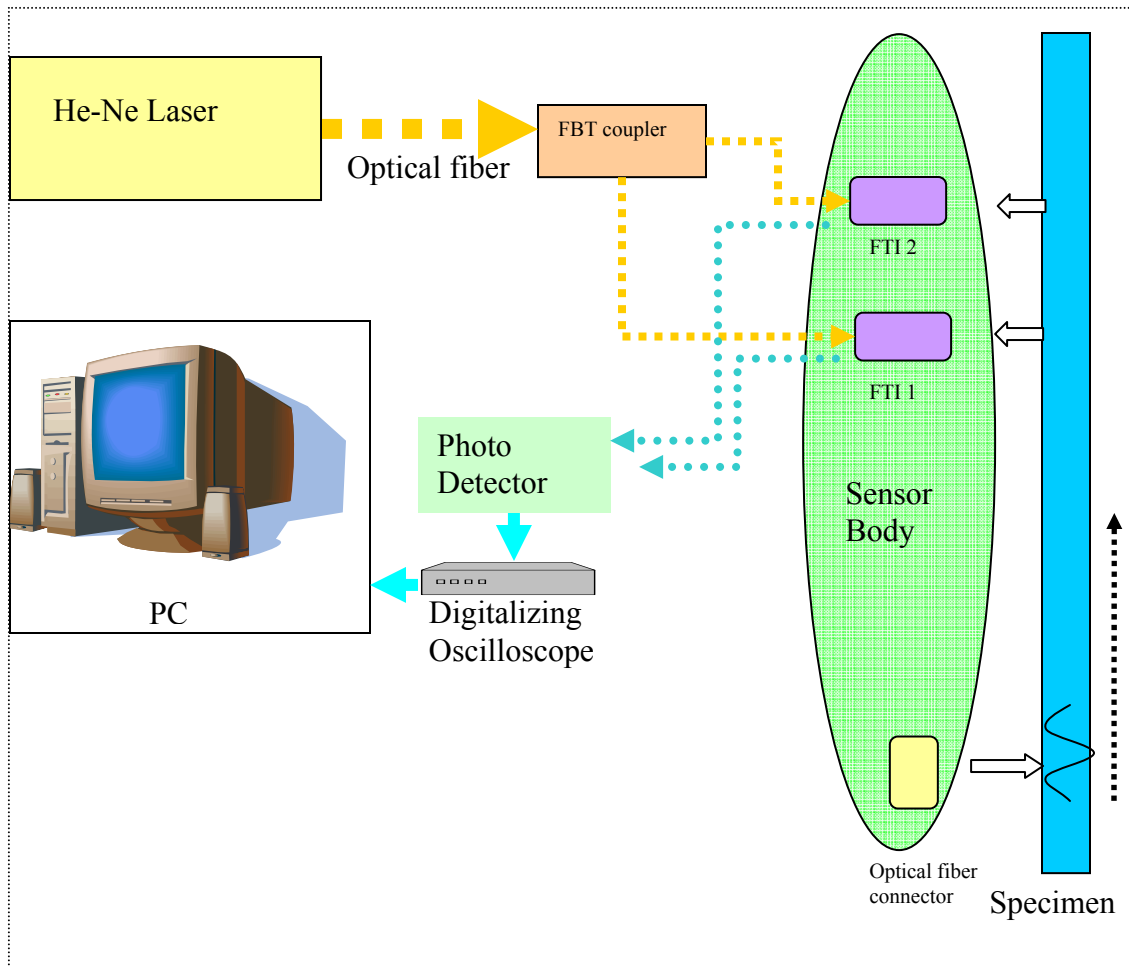


Fig. 2.4. Data acquisition system

CHAPTER III

CONCEPTUAL SENSOR DESIGN

The design process followed for the development of sensor concept is introduced in this chapter. The design process includes three subsequent sections: need analysis, concept development and final design. In need analysis, the primary functions and parameters required to open up the solution set for sensor design are formulated. In concept development, different design concepts satisfying the functions and parameters are developed. In final design, the one viable concept chosen using a selection matrix for further embodiment is developed into a final configuration. Feasibility of the final configuration is also explored. The multi-purpose sensor configuration incorporates a pulsed laser for ultrasonic wave generation and a fiber tip interferometer (FTI) for wave detection as introduced in the proceeding chapter.

3.1. Need Analysis

In this research, the sensor is defined as non-contact and non-destructive sensor. Therefore, all of the needs are addressed by creating a non-contact approach for a sensor body, stabilizing the parts of the sensor body, and providing an adjustment system to calibrate position in order to excite acoustic wave and acquire acoustic wave in a very precise location.

3.1.1. Evolution of need

Abstraction 1

The TAP-NDE method allows acoustic waves to be generated by an Nd:YAG laser and detected by fiber tip interferometer (FTI) system remotely. Non-contact evaluation method is also the basis of the sensor design. Therefore, the first primary function for sensor design is to develop a non-contact approach. The surface condition which the sensor body must locate is very important. A different surface condition may have different non-contact requirements required of the sensor body. Therefore, the associated

constraint is assuming that the surface in which the sensor body must locate is flat. The primary function 1 is to create a non-contact approach for measurement. The primary parameter is a non-contact approach and the primary constrain is the flat surface.

For the primary function number 1, which is to create a non-contact approach for the sensor body, ease of sensor body installation and removal must be considered along with easy sensor body accommodation. Thus easy installation and removal is the first sub-function. In addition, the sub-function implies the use of standard hand tools, for the reasons that most technicians are more familiar with them. Thus, the connection type of the sensor body with the surface is the parameter, and using standard parts to design the sensor body-surface interface is the associated constraint. Easy sensor body accommodation is the second sub-function of this primary function. Since sensor body is oftentimes required to accommodate limited accessible space, the flexibility of the sensor body is the parameter of the sub function, with the volume of the sensor body as its constraint. The sub-function 1-1 is to install and remove sensor body easily. The parameter is the connection type and the constraint is the standard parts. The sub-function 1-2 is to accommodate sensor body easily. The parameter is the flexibility and the constraint is the volume of sensor body.

Abstraction 2

Extremely small out-of-plane displacements are measured by the FTIs system. Since any small disturbance to the sensor body may cause significant measurement errors, it is essential to ensure stability of the sensor body. Hence, the second primary function is addressed by providing stability to all components of the body. A possible disturbance is the deformation of the sensor body resulting from its own weight. The allowed maximum displacement will be the constraint of this primary function. The primary function 2 is to stabilize all components of sensor body. The primary parameter is the deformation and the primary constraint is maximum allowed displacement (0.00001m).

In TAP-NDE apparatus, both the optical fiber connector and GRIN fiber collimator are required to be amounted on the sensor body. The two components that are to be purchased with THORLAB Inc. are shown in Figs. 3.1 and 3.2. Since they are used to

generate and detect ultrasonic waves, interfacing the optical fiber connector and the GRIN fiber collimator with the sensor body is an important issue. All components and all amounting interfaces must be stabilized. Therefore, two sub-functions are defined as follows. The sub-function 2-1 is to connect optical fiber connector. The parameter is the deformation at interface. The constraint is the maximum displacement allowed (0.00001m). The sub-function 2-2 is to connect GRIN fiber collimator. The parameter is the deformation at interface and the constraint is maximum displacement allowed (0.00001m).

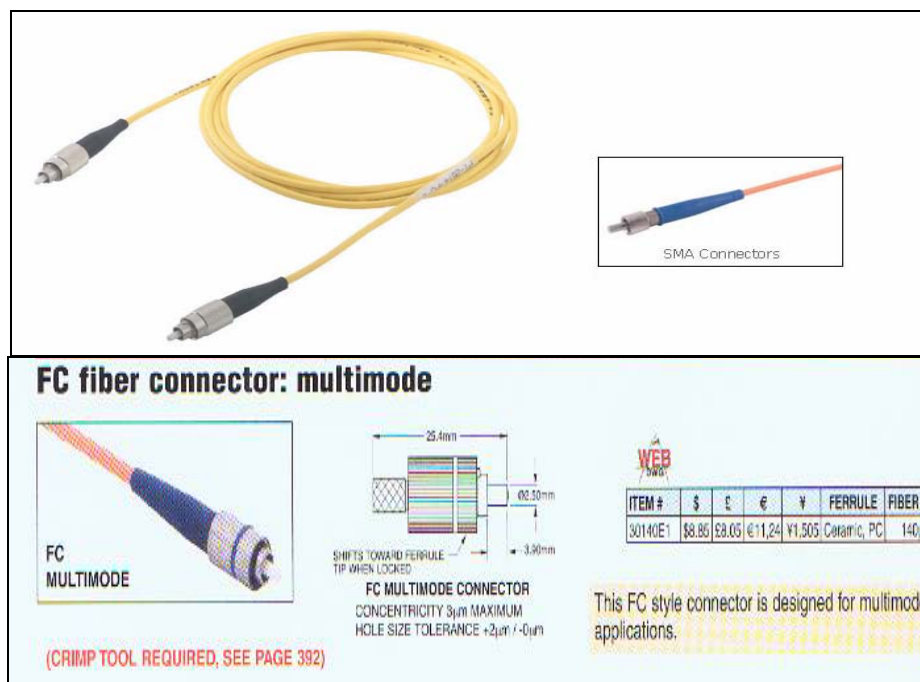


Fig. 3.1. Multimode patch cable connector (THORLAB Inc.)



Fig. 3.2. GRIN fiber collimator (THORLAB Inc.)

Abstraction 3

The location where the optical fiber connected to the Nd:YAG laser for wave generation is different from the location where the GRIN lens is mounted. Allowing for position adjustment is thus an important issue. The third primary function is to provide an adjustment system for the calibration of optical fibers and GRIN lens. The adjustment scales play an important role in the overall system adjustment. Smaller the adjustment scales, better precise positioning can be achieved. Thus, the minimum adjustment scale is the constraint of the primary function. The primary function 3 is to provide adjustment system allowing for precise optical fiber and Grin lens positioning. The primary parameter is to provide the adjustment system and the primary constraint is maximum allowed adjustment scale (1.0mm).

Providing an adjustment system for precision positioning is a global need. However, the location of the adjustment system is of great concern. The optical fiber connector and GRIN fiber collimator are required to have two degrees of freedom adjustment because they need to be positioned in the horizontal and vertical directions. Additionally, the sensor body is supposed to have only one adjustment system which is height. The maximum adjustment scale which is 1.0mm is the constraints of the adjustment system.

The three sub-functions are defined as follows. The sub-function 3-1 is to provide two degrees of freedom adjustment for optical fiber connector. The parameter is the adjustment scale and the constraint is maximum allowed adjustment scale (1.0mm). The sub-function 3-2 is to provide two degrees of freedom adjustment for GRIN fiber collimator. The parameter is the adjustment scale and the constraint is maximum allowed adjustment scale (1.0mm). The sub-function 3-3 is to provide at least one degree of freedom for sensor body. The parameter is the adjustment scale and the constraint: maximum allowed adjustment scale (1.0mm).

3.1.2. Function structure

Function structure is used to determine the true need of the design while identifying the scope and range in which it should effectively perform. A function structure for the sensor design has been developed in the previous chapter. This function structure takes into consideration the primary functions required of the conceptual sensor body design.

A functional diagram is a way to visualize the function structure. It starts with the need statement being placed on top of the hierarchy tree. The need statement is developed by identifying the primary functions and constraints (PC). The tree then branches off into the primary functions which identify the properties implied in the need statement. Each function is split into sub-functions. Each sub function must be independent from all others. Constraints and design parameters (DP) associated with the sub-functions are also identified. Fig. 3.3 is the completely developed function structure (functional diagram) for the sensor body. Each function is further broken down into sub-functions, constraints and design parameters, which can be seen in Figs. 3.4, 3.5, and 3.6.

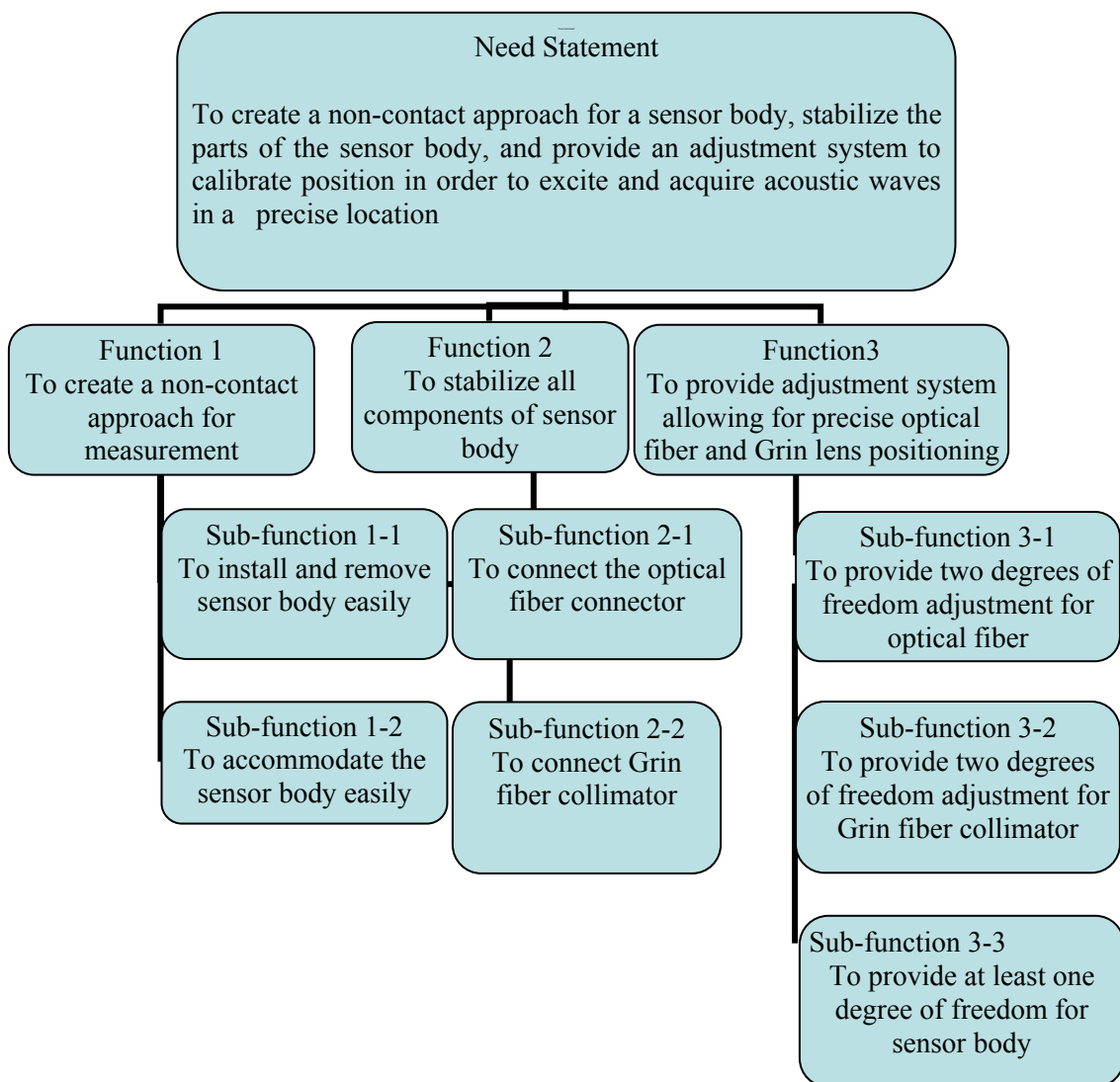


Fig. 3.3. Overall function structure

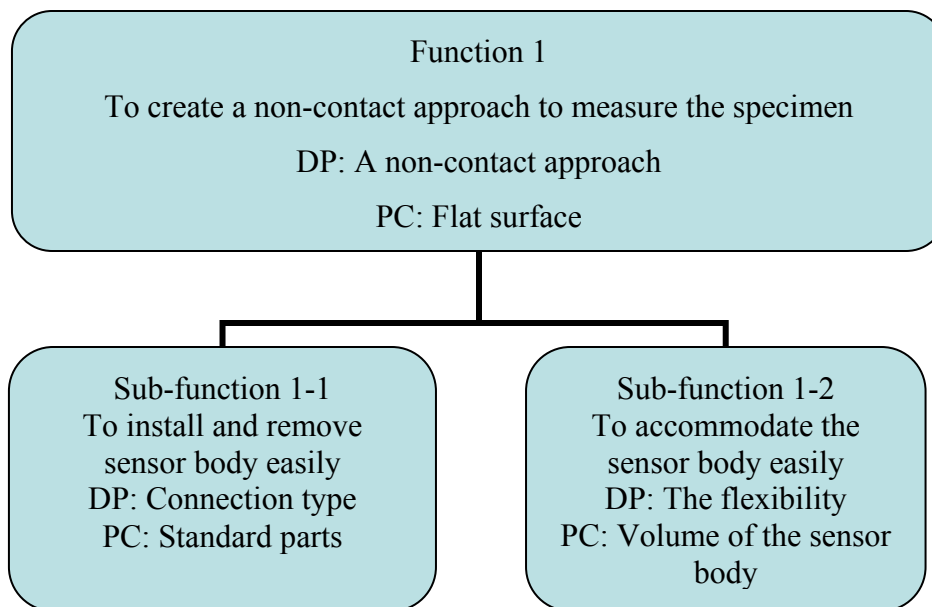


Fig. 3.4. Function 1 diagram

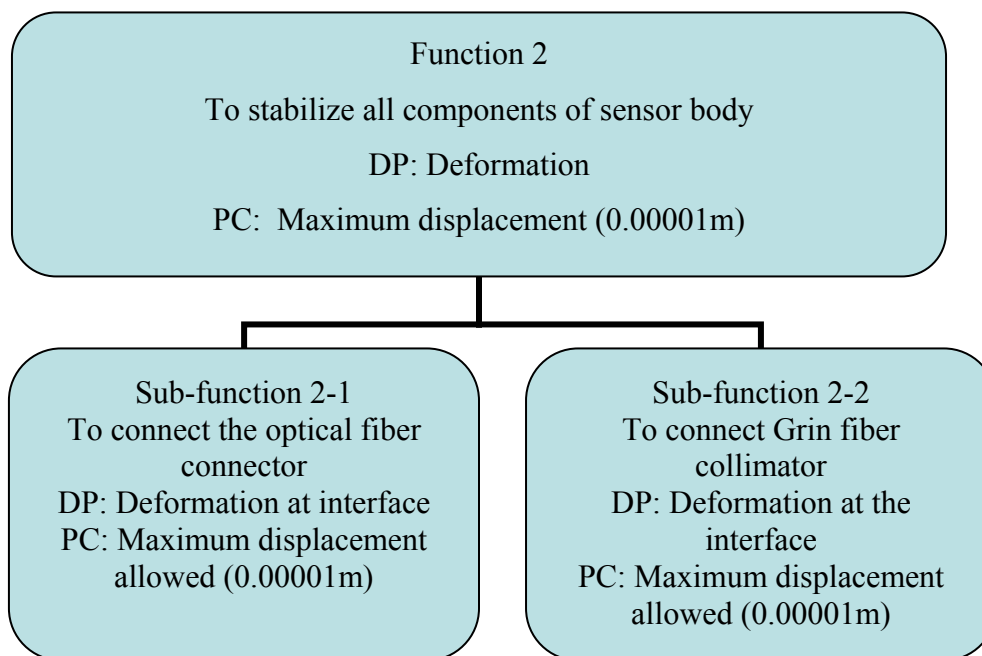


Fig. 3.5. Function 2 diagram

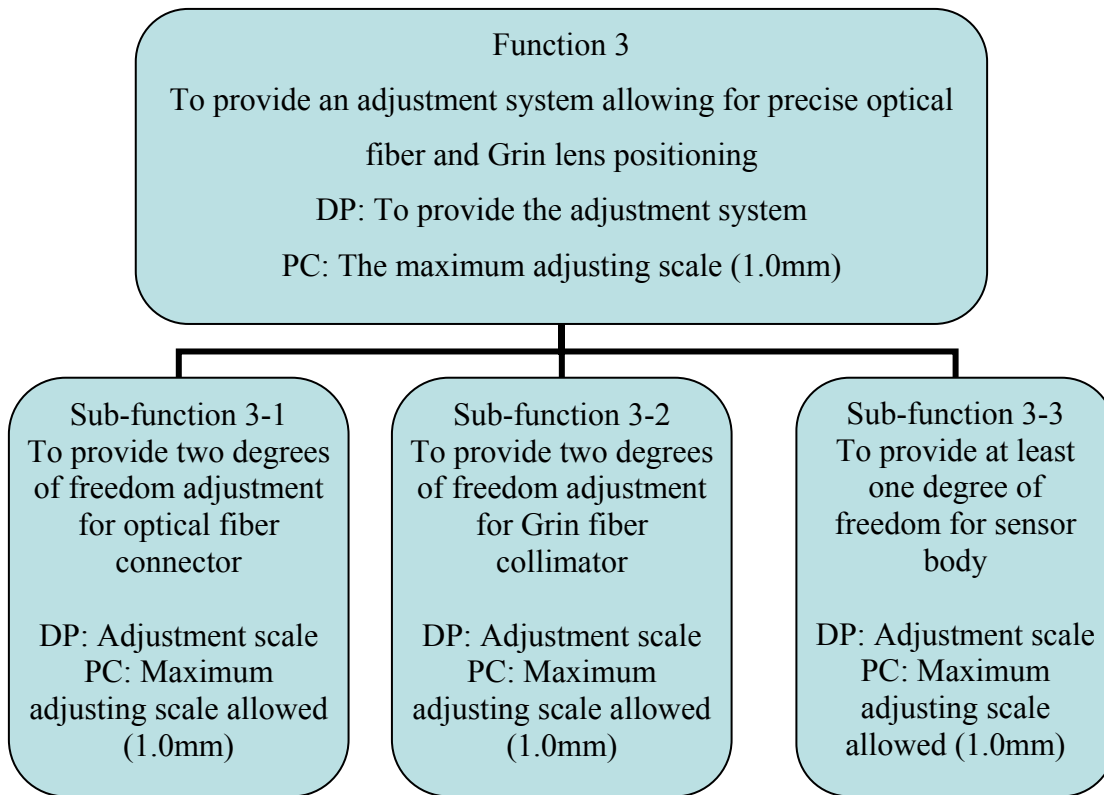


Fig. 3.6. Function 3 diagram

3.2. Concept Design

After evaluating the functions for the sensor design, several different design concepts are created. The primary areas identified for design consideration include sensor head, sensor arm and sensor foot. The primary function of the sensor head is to provide interface with the optical fiber connector and GRIN fiber collimator, and to provide position adjustment. Similarly, the primary function of the sensor arm is to provide the connection of the sensor head with the sensor foot. The primary function of the sensor foot is to support the sensor. Two different concepts for the sensor head were resulted along with three sensor arm concepts and two sensor foot concepts.

3.2.1. Sensor head

Concept 1

The concept shown in Fig. 3.7 consists of the following six parts. Optical fiber connector is to provide a platform for connecting optical fiber. GRIN fiber collimator is to provide a platform for connecting GRIN lens. Movable sensor base A is to provide interface with optical fiber connector. Movable sensor base B is to provide interface with GRIN fiber collimator. Chassis is to provide horizontal mobility to sensors A and B. Movable sensor base screws are to control forward and backward motion of movable sensor A and B along horizontal direction.

In this concept, both sides of the movable base A and B have a rack structure. The movable sensor base screw has a pinion structure. The movable bases A and B which can slide in the horizontal direction are controlled by the movable sensor base screws. The heights of the optical fiber connector and GRIN fiber collimator can be adjusted by screwing itself into the sensor bases A and B at different locations. Hence, the sensor head has two degrees of freedom adjustment.

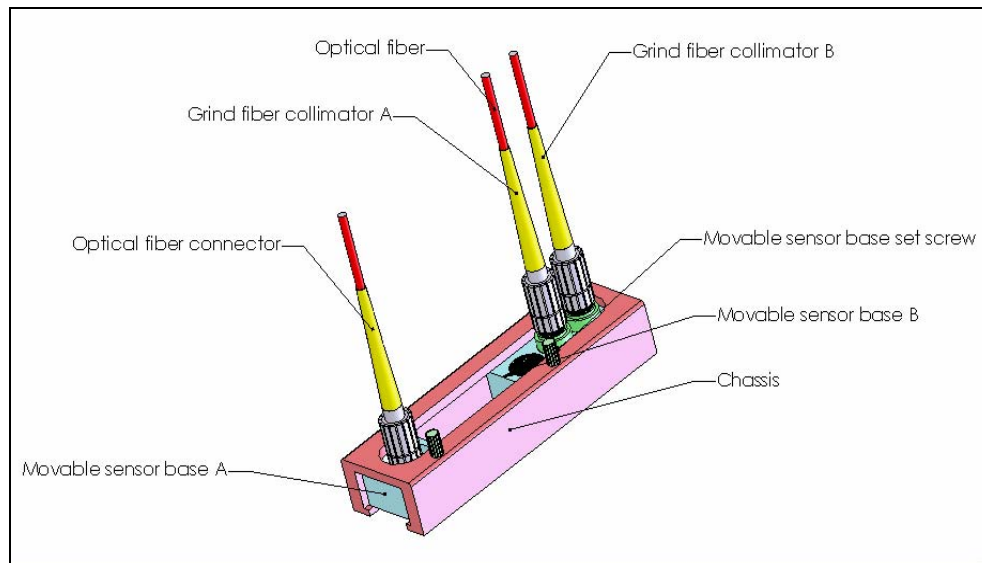


Fig. 3.7. Sensor head-concept 1

Concept 2

The concept shown in Fig. 3.8 consists of the following six parts. Optical fiber connector is to provide a platform for connecting optical fiber. Grin fiber collimator is to provide a platform for connecting GRIN lens. Movable sensor base A is to provide interface with optical fiber connector. Movable sensor base B is to provide interface with GRIN fiber collimator. Inner chassis is to provide horizontal mobility to sensors A and B. Outer chassis is to provide inner chassis with vertical mobility. Movable sensor base screws are to control horizontal mobility of sensors A and B. Vertical alignment wheel is to control vertical mobility of inner chassis.

In this concept, both sides of the movable bases A and B have a rack structure. The movable sensor base screw has a pinion structure. The idea is that the movable bases A and B allowing for horizontal translations are controlled by the movable sensor base screw. Similarly, the inner chassis has a rack structure. The vertical alignment wheel is a gear which couples the rack to the inner chassis. The inner chassis allowing for vertical translation is controlled by the vertical alignment wheel. In addition, the heights of the optical fiber connector and GRIN fiber collimator can be adjusted by turning the sensor base screw. This concept has two degrees of freedom adjustment as well, while allows optical fiber connector and Grin fiber collimator to be adjusted by the vertical alignment wheel at the same time.

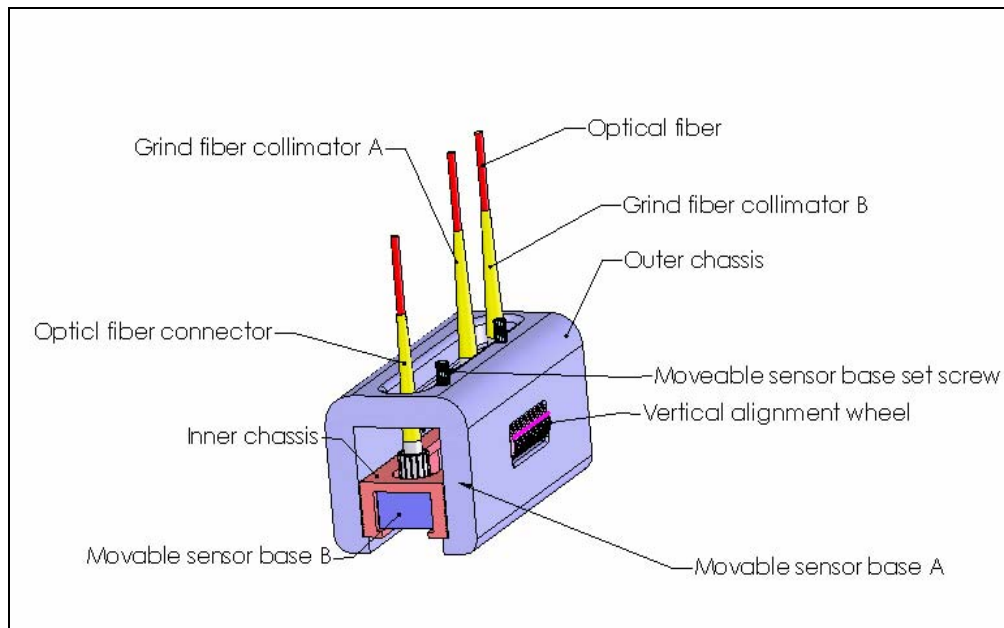


Fig. 3.8. Sensor head-concept 2

3.2.2. Sensor arm

Concept 1

The first sensor arm concept that connects to the sensor head is a simple structure having no adjustment. Fig. 3.9 shows the configuration.

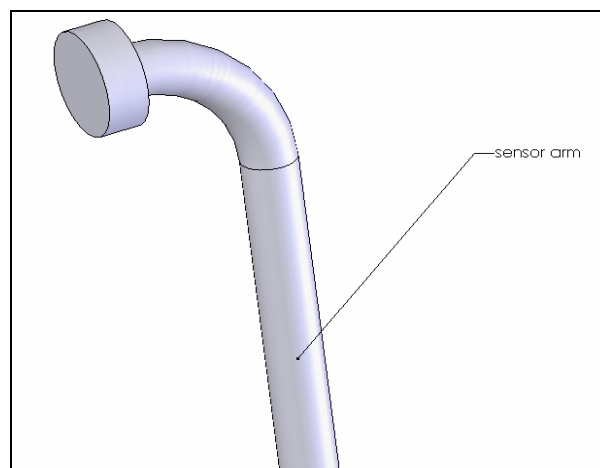


Fig. 3.9. Sensor arm-concept 1

Concept 2

The second sensor arm concept shown in Fig. 3.10 consists of the following six parts. Neck is to support and provide interface with sensor head. Neck gear A is to transmit motion of gear A to the neck. Neck gear B is to transmit the motion of the neck locking screw to gear A. Neck shaft is to connect neck gear A and neck. Neck locking screw is to control scale of rotation of neck. Sensor arm is to support all components.

The idea of the concept is that the neck, while connected to the sensor head, can rotate about the neck shaft. The angle of rotation is controlled by the neck gear B which is connected with the neck locking screw. Hence, the sensor arm concept has only one degree of freedom.

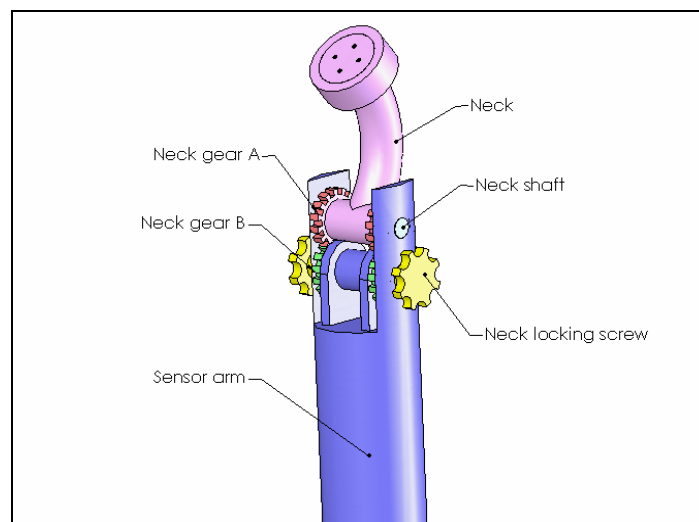


Fig. 3.10. Sensor arm-concept 2

Concept 3

The third sensor arm concept shown in Fig. 3.11 consists of the following eight parts. Chassis interface shaft is to provide interface with sensor head. Single-direction thrust bearing is to allow chassis interface shaft to rotate. Neck is to support sensor head. Neck gear A is to transmit the motion of gear A to the neck. Neck gear B is to transmit the motion of the neck locking screw to the gear A. Neck shaft is to connect neck gear A and

neck. Neck locking screw is to control scale of rotation of the neck. Sensor arm is to support all components.

The idea of the concept is very similar to Concept 2, except that there is a single direction thrust bearing between the neck and the chassis interface shaft. The chassis interface shaft can rotate along the neck axial axis. Therefore, the sensor arm concept has a two-degrees-of-freedom adjustment system.

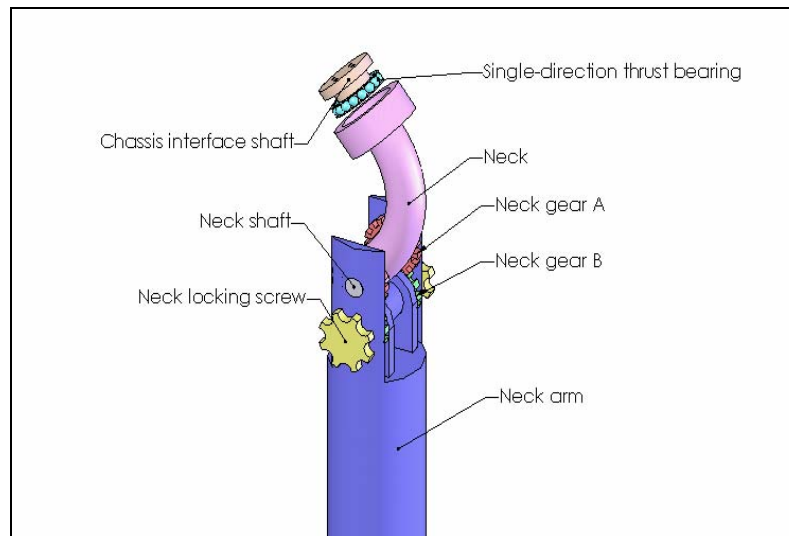


Fig. 3.11. Sensor arm – concept 3

3.2.3 Sensor foot

Concept 1

The first sensor foot concept shown in Fig. 3.12 consists of the following three parts. Sensor arm shell is to provide sliding track for sensor arm. Sensor arm locking screw is to control neck arm movement vertically. Sensor arm base is to support all constituent components of the sensor.

The idea of this concept is that the neck arm can be adjusted in the vertical direction using the sensor arm locking screw. The sensor arm shell is located at the center of the

sensor arm base which is a rectangular plate. Hence, the sensor foot has one degree of freedom.

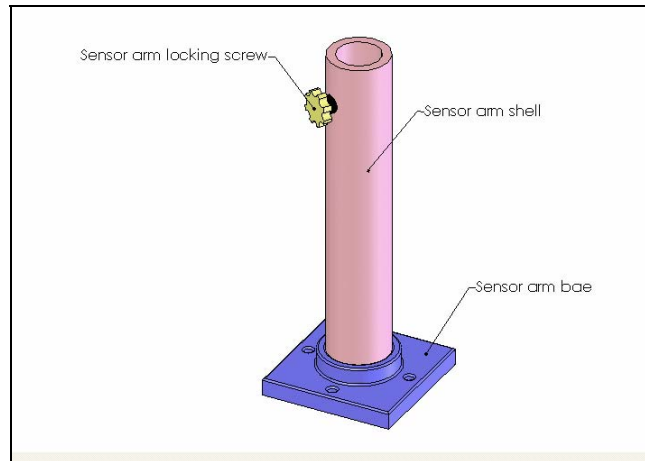


Fig. 3.12. Sensor foot-concept 1

Concept 2

The second sensor foot concept shown in Fig. 3.13 consists of the following three parts. Sensor arm shell: To provide sliding track for neck arm. Sensor arm locking screw is to control neck arm movement vertically. Sensor arm base is to support all constituent components of the sensor.

The idea of this concept is similar to Concept 1. It also provides one degree of freedom, but the difference is that the neck arm shell is located at the biased center of the sensor arm base which is a circular plate.

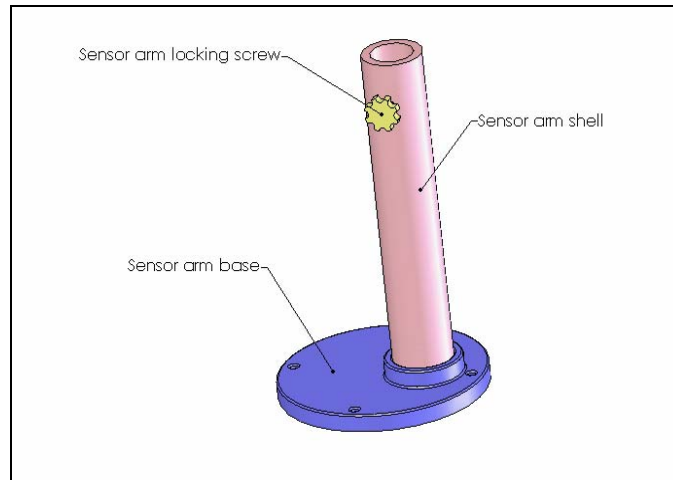


Fig. 3.13. Sensor foot-concept 2

3.2.4. Selection matrices

From among all the design concepts, one design must be chosen for each of the sensor component. Selections are made based on critical design criteria. Using an evaluation matrix, each concept is evaluated against a datum which is either a pre-existing configuration or one that is designated as reference. If a design concept is better than the datum, it receives a plus sign. A minus sign means it is inferior to the datum in that particular design criterion being considered. An S stands for the same. The total of number of pluses and minuses are then tallied at the bottom of the evaluation matrix to identify the best design concept. The evaluation matrices for the selection of the best sensor head, sensor arm, and sensor foot concepts are shown in Tables 3.1, 3.2 and 3.3, respectively.

Table 3.1. Sensor head selection matrix

Evaluation Criteria	Concept 1 movement in vertical direction without adjusting gear (Datum)	Concept 2 movement in vertical direction with adjusting gear
Movement in horizontal direction		S
Movement in vertical direction		+
Assembly time		-
Time of adjustment		+
Total +'s		2
Total -'s		1
Total Score		+1

Table 3.2. Sensor arm selection matrix

Evaluation Criteria	Concept 1 No degree of freedom	Concept 2 One degree of freedom (Datum)	Concept 3 Two degrees of freedom
Rotary movement	-		+
Axial movement	-		S
Assembly time	+		-
Time of adjustment	-		+
Total +'s	1		2
Total -'s	3		1
Total Score	-2		+1

Table 3.3. Sensor foot selection matrix

Evaluation Criteria	Concept 1 Concentric position with rectangular base (Datum)	Concept 2 Biased position with circular base
The flexibility of installation		+
Balancing		-
Assembly time		S
Time of adjustment		S
Total +'s		1
Total -'s		1
Total Score		0

3.2.5. Concept design summary

In summary, several viable design concepts have been presented for each of the following designs: (1) sensor head, (2) sensor arm and (3) sensor arm. Through careful considerations and design evaluations, a sensor body concept was selected. The selected concept has a sensor head design that allows the optical fiber connector and GRIN fiber collimator to move in the horizontal direction individually and in the vertical direction together. In addition, the height of measurement can be adjusted by changing the screw height. The concept also has a sensor arm design that allows the chassis interface shaft to rotate along the neck axis, and the neck to rotate along the neck shaft. It is supported by a foot design that has a circular plate and a sensor arm shell that is placed at a biased position. As is seen in Table 3.4, the material selected for all the components is Aluminum alloy 6061. In the section that follows, design optimization is performed using the COSMOSWorks FEA tool. This is done to also identify possible weak links in the design.

Table 3.4. Aluminum alloy 6061 material properties

Yield Strength (Typical)	8	ksi	55	MPa
Tensile Strength (Typical)	18	ksi	124	MPa
Young's Modulus	10	E6 psi	69	GPa
Shear Modulus	3.75	E6 psi	26	GPa
Poisson's Ratio	0.33			
Thermal Expansion Coefficient	13	E-6 1/F	23.4	E-6 1/C
Density	0.098	lb/(in ³)	2713	kg/(m ³)
Thermal Conductivity	1190	BTU-in/(ft ² -h-F)	172	W/(m-C)
Specific Heat	0.23	BTU/(lbm-F)	0.963	kJ/(kg-C)
Melting Point	1205	F	652	C

3.3. Final Design

After the preferred design concept was selected, the feasibility of each design concept is established. To this end, force analysis for every component of the design concept is performed. Only components that are concerned for possible failure are analyzed. In the sensor head concept, the vertical alignment wheel is the weakest part since the inner chassis is lifted by it. In the sensor arm concept, the neck gear is the weakest since it needs to support the sensor head and neck with a very small contacting area. In the sensor foot design, the connecting area of the sensor arm base with sensor arm shell is the weakest. The following force analyses are carried out to ensure that every part is safe and that weight-induced deflections do not exceed the design tolerance.

3.3.1. Analysis on vertical alignment wheel

Stress analysis is performed to ensure that the deflection of the wheel due to the weight of the movable bases A and B, optical fiber connector, movable sensor base screws, and inner chassis do not exceed the tolerance set in the function structure. The total weight of the movable bases A and B, optical fiber connector, movable sensor base screws, and inner chassis is 0.09 Kg or 0.882 N. The weight force vectors (purple arrows in Fig. 3.14) act on one of the gear faces that contacts with the inner chassis. The boundary condition is that the shaft of the wheel is constrained both translationally and rotationally (green arrows).

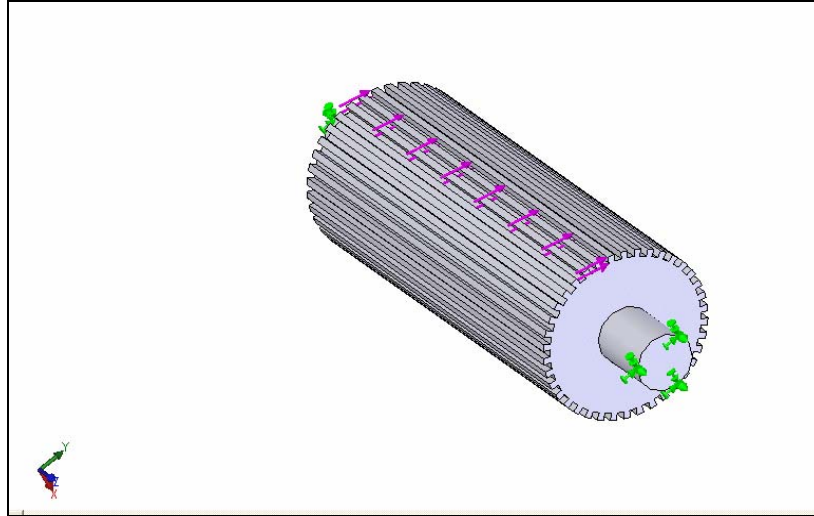


Fig. 3.14. Boundary conditions of vertical alignment wheel

The displacement distribution of the vertical alignment wheel is shown in Fig. 3.15. The maximum displacement is 0.0000001399m, which stays well within the 0.00001m tolerance specified in the function structure.

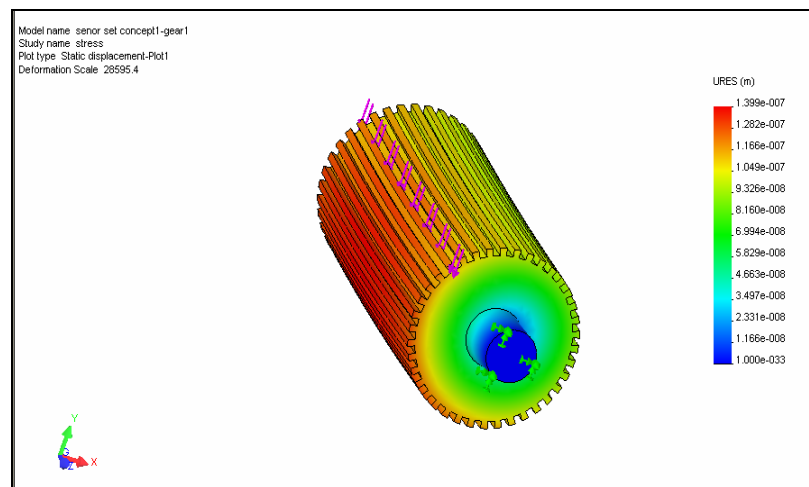


Fig. 3.15. Vertical alignment wheel displacement distribution

The factor of safety (FOS) is defined using material yield stress and von Mises stress as $\frac{\sigma_{vonMises}}{\sigma_{Limit}} < FOS$, where $\sigma_{Limit} = \sigma_{yield} = 55000000(Pa)$. From Fig. 3.16, it can be seen the design has a lowest factor of safety of 100.

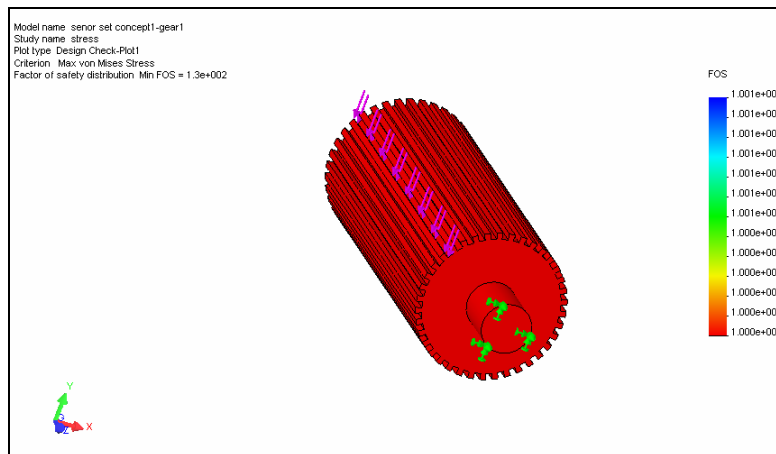


Fig. 3.16. Vertical alignment wheel factor of safety distribution

3.3.2. Analysis on neck gear

Neck gear is also studied using COSMOSWorks to determine if it is strong enough to withstand the applied force. The applied force (red arrows), which equals to the weight sum of the sensor head, chassis interface shaft, neck and two neck gears, is 0.532 Kg or 5.217 N. The applied force is normal to one of the gear faces and the hole for the shaft is treated as a fixed boundary condition in all directions (green arrows) as shown in Fig. 3.17.

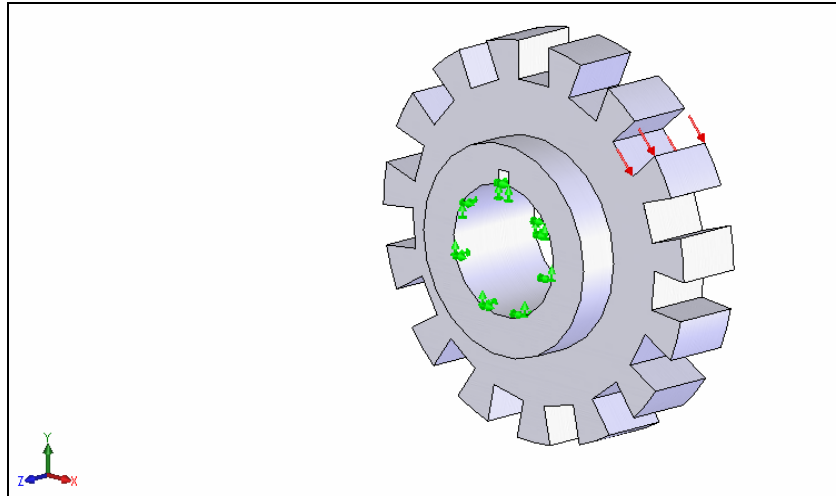


Fig. 3.17. Boundary conditions of neck gear

The displacement distribution of the neck gear is shown in Fig. 3.18. The maximum displacement is $4.866e-8$ m, which does not exceed the $1e-5$ m tolerance set in the function structure.

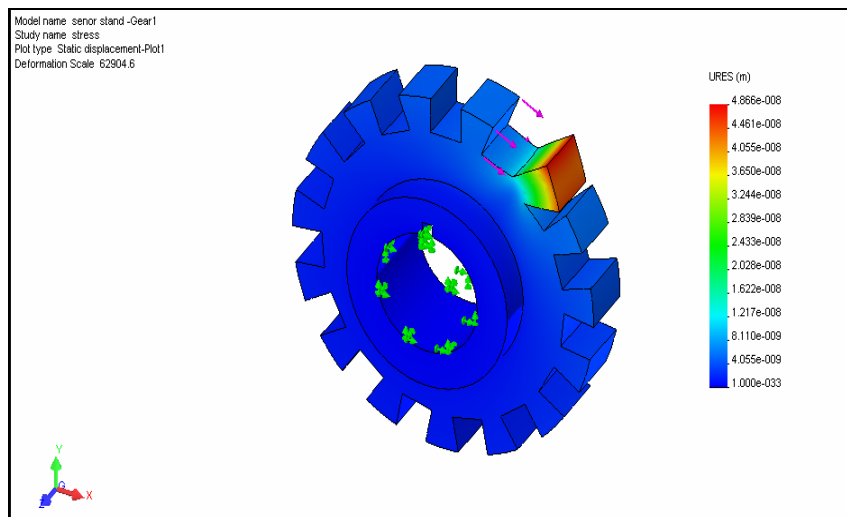


Fig. 3.18. Neck gear displacement distribution

Similarly, using the definition from before, the component is seen to have a minimum FOS of 28 (Fig. 3.19.)

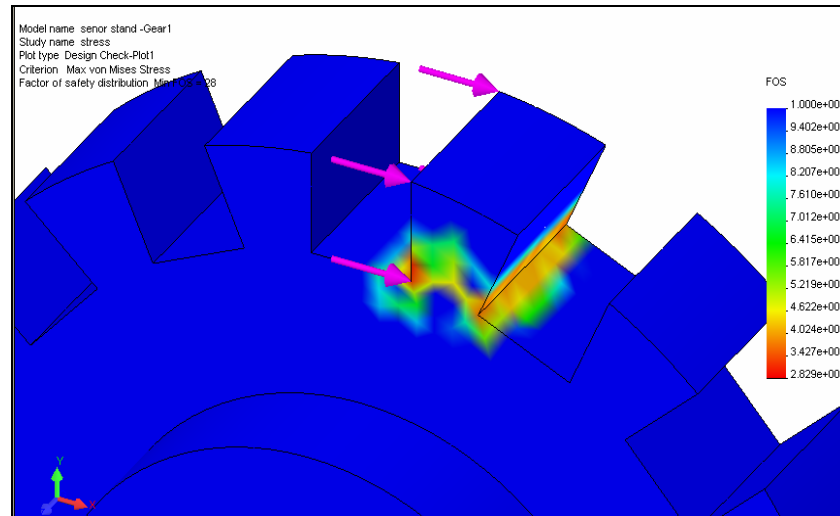


Fig. 3.19. Neck gear factor of safety distribution

3.3.3. Analysis on sensor base

The sensor base is also analyzed in the same way with applied force vectors and constraints. The applied force (purple arrows), which is the total weight of the whole sensor except for the weight of the sensor base, is 4.418 Kg or 43.296 N. It exerts on the internal screws of the sensor base. The four holes that are connected to the ground are fixed in all directions (green arrows). Fig. 3.20 shows the corresponding boundary conditions.

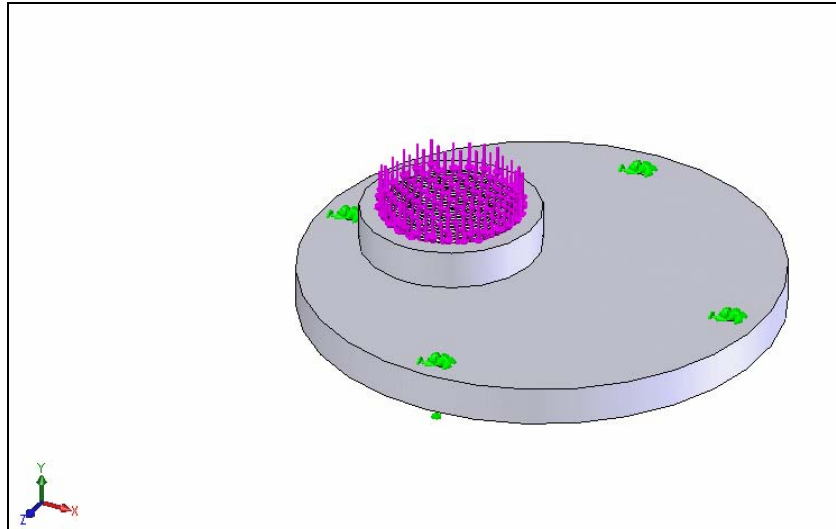


Fig. 3.20. Boundary conditions of sensor base

The displacement distribution of the neck gear is shown in Fig. 3.21. The maximum displacement is 1.879×10^{-7} m which again does not exceed the 1×10^{-5} m tolerance set in the function structure. From Fig. 3.22, it can be seen that the lowest factor of safety is 170.

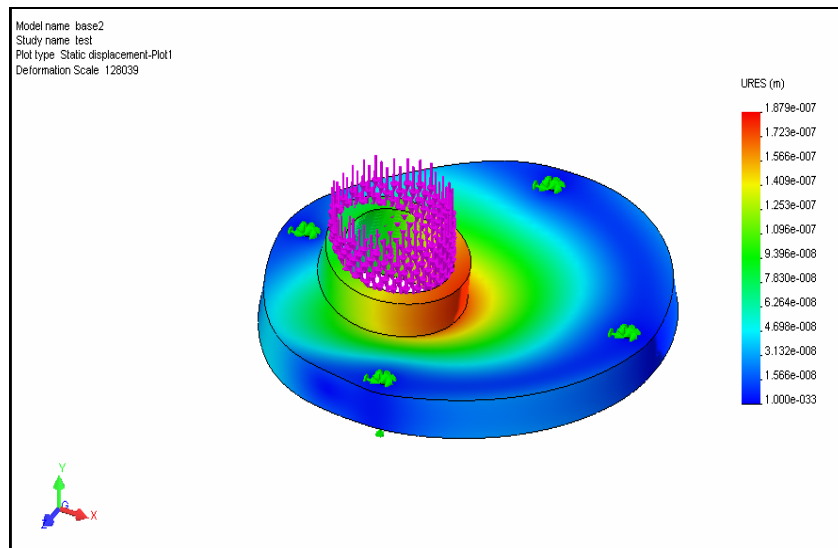


Fig. 3.21. Sensor base displacement distribution

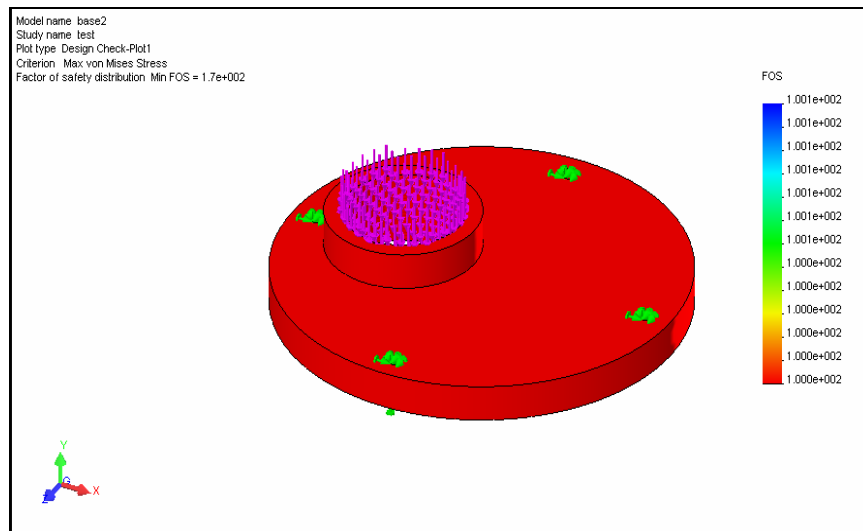


Fig. 3.22. Sensor base factor of safety distribution

3.3.4. Conclusions

The three major components; namely, the vertical alignment wheel, neck gear, and sensor base, have been analyzed using COSMOSWorks FEA. These results showed that components that are potentially prone to mechanical failure were all structurally sound subject to the considered boundary and forcing conditions. Furthermore, these results also established the feasibility of the sensor design. This sensor design is therefore viable for incorporating and supporting the pulsed laser and fiber tip interferometer that were discussed in Chapter 2. In summary, there are three major components of the sensor design. They are the sensor head, sensor arm, and sensor foot. For the sensor head design, it has two degrees of freedom which allows the operator to adjust the laser generation system and the FTI sensing system to the desire location accurately. The scales of all adjustments of the sensor head are 1 mm per revolution. For sensor arm design, it also has two degrees of freedom adjustments which can rotate the sensor head around. The scales of all adjustment of sensor arm are 1 mm per revolution. Finally, the sensor foot has one degree of freedom which allows sensor arm to move up or down. The final configuration of the sensor body design is shown in Fig. 3.23.

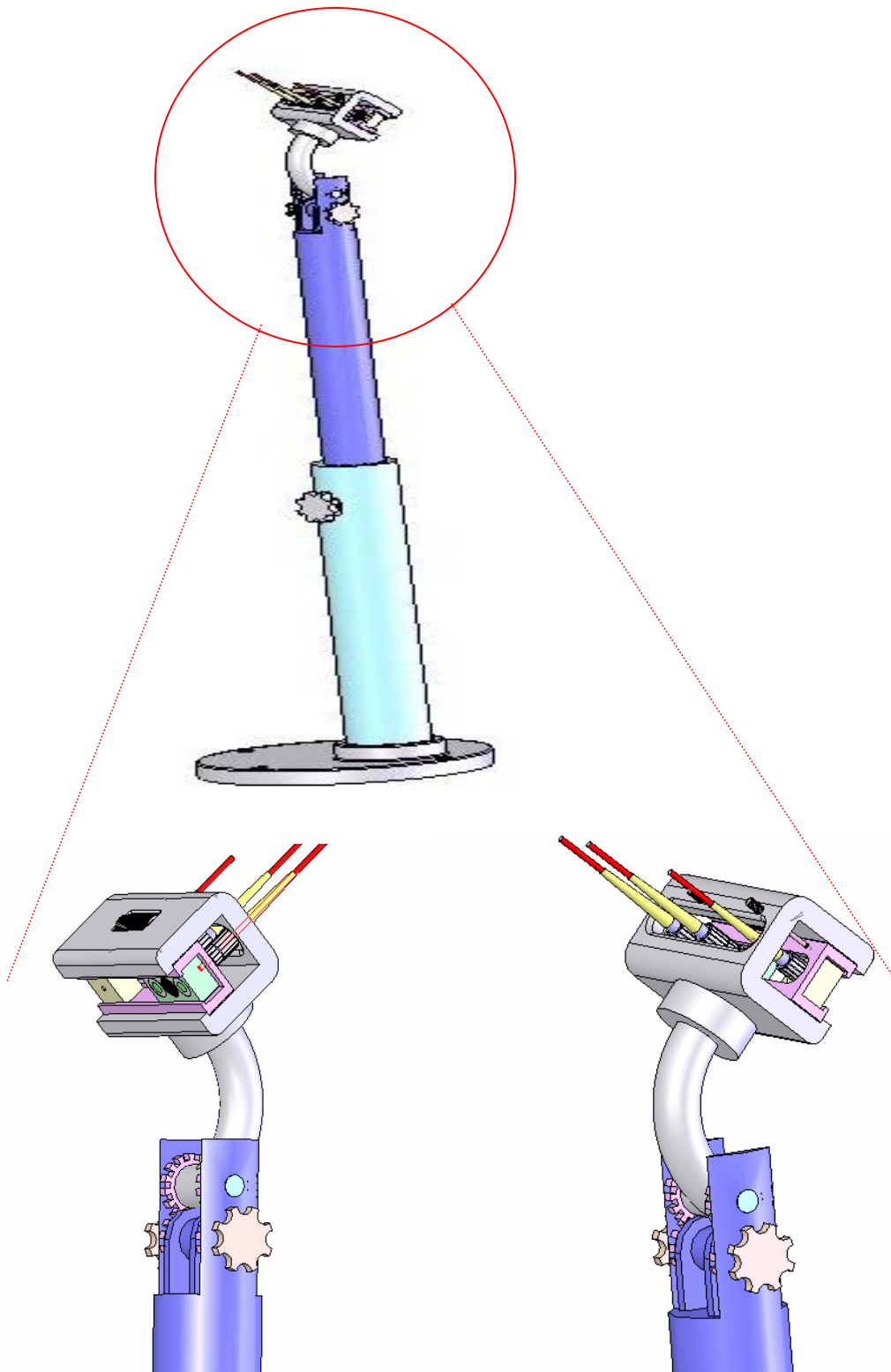


Fig. 3.23. The final design configuration of sensor body

CHAPTER IV

MODIFIED FORMULATION OF WAVE PROPAGATION

In order to find out the relationship of ultrasonic wave dispersion with pressure, temperature and plate thickness, a theoretical model needs to be developed. In this chapter, a modified wave propagation model is introduced. In the subsequent sections, the classical theory of wave propagation is reviewed as the basis for deriving the wave propagation model. Lamb plate waves propagating in thin structures plate are also reviewed. As Lamb wave dispersion is used to resolve temperature, pressure and thickness, specifics regarding how this is accomplished is also discussed. Gabor wavelet transform is reviewed for its use as the tool for extracting feature information. After the classical theory of wave propagation and Gabor wavelet transform are presented, the modified wave propagation model is then derived.

4.1. Classical Theory of Wave Propagation

The classical theory of wave propagation is a fundamental theory from which many different waves including Rayleigh surface waves and Lamb plate waves are derived subject to given boundary. Consider the stress element isolated from the finite plate shown in Figure 4.1, σ_{xx} , σ_{xy} , σ_{xz} are stress components in the xz plane, σ_{zx} , σ_{zy} , σ_{zz} are stress components in the xy plane and σ_{yx} , σ_{yy} , σ_{yz} are stress components in the yz plane. The equations of motion are obtained by applying Newton's Second Law, $\sum F_i = ma_i$,

$$\begin{aligned}
 \frac{\partial \sigma_{xx}}{\partial x} + \frac{\partial \sigma_{xy}}{\partial y} + \frac{\partial \sigma_{xz}}{\partial z} &= \rho \frac{\partial^2 u}{\partial t^2} \\
 \frac{\partial \sigma_{yx}}{\partial x} + \frac{\partial \sigma_{yy}}{\partial y} + \frac{\partial \sigma_{zy}}{\partial z} &= \rho \frac{\partial^2 v}{\partial t^2} \\
 \frac{\partial \sigma_{xz}}{\partial x} + \frac{\partial \sigma_{zy}}{\partial y} + \frac{\partial \sigma_{zz}}{\partial z} &= \rho \frac{\partial^2 w}{\partial t^2}
 \end{aligned} \tag{4.1}$$

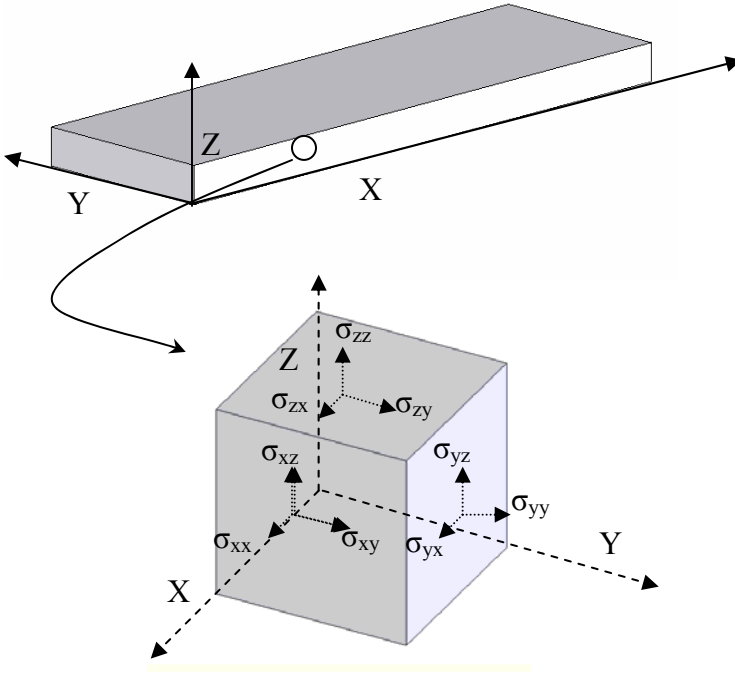


Fig. 4.1. Stress components of a stress cube

where u , v and w are the displacements along the x , y and z direction, respectively, and ρ is the density of the material. The constitutive equation for isotropic material can be written as follows [24]

$$\begin{aligned}
 \sigma_{ij} &= 2\mu\epsilon_{ij} + \lambda\epsilon_{kk}\delta_{ij} \\
 \sigma_{xx} &= \lambda(\epsilon_{xx} + \epsilon_{yy} + \epsilon_{zz}) + 2\mu\epsilon_{xx} \\
 \sigma_{yy} &= \lambda(\epsilon_{xx} + \epsilon_{yy} + \epsilon_{zz}) + 2\mu\epsilon_{yy} \\
 \sigma_{zz} &= \lambda(\epsilon_{xx} + \epsilon_{yy} + \epsilon_{zz}) + 2\mu\epsilon_{zz} \\
 \sigma_{xy} &= \frac{E}{2(1+\nu)}\epsilon_{xy} \\
 \sigma_{xz} &= \frac{E}{2(1+\nu)}\epsilon_{xz} \\
 \sigma_{yz} &= \frac{E}{2(1+\nu)}\epsilon_{yz}
 \end{aligned} \tag{4.2}$$

where ε_{xx} , ε_{yy} , ε_{zz} , ε_{xy} , ε_{xz} and ε_{yz} are strain components, λ and μ are the Lamé constants and ν is the Poisson's ratio. The relation between strains and displacements are

$$\begin{aligned}
\varepsilon_{xx} &= \frac{\partial u}{\partial x} \\
\varepsilon_{yy} &= \frac{\partial v}{\partial y} \\
\varepsilon_{zz} &= \frac{\partial w}{\partial z} \\
\varepsilon_{xy} &= \frac{\partial u}{\partial y} + \frac{\partial v}{\partial x} \\
\varepsilon_{xz} &= \frac{\partial u}{\partial z} + \frac{\partial w}{\partial x} \\
\varepsilon_{yz} &= \frac{\partial v}{\partial z} + \frac{\partial w}{\partial y}
\end{aligned} \tag{4.3}$$

Combining Eqs. (4.2) and (4.3) into (4.1), the governing equations of wave propagation in terms of displacement variables are then obtained,

$$\begin{aligned}
(\lambda + \mu) \frac{\partial}{\partial x} \left(\frac{\partial u}{\partial x} + \frac{\partial u}{\partial y} + \frac{\partial u}{\partial z} \right) + \mu \left(\frac{\partial^2 u}{\partial x^2} + \frac{\partial^2 u}{\partial y^2} + \frac{\partial^2 u}{\partial z^2} \right) &= \rho \frac{\partial^2 u}{\partial t^2} \\
(\lambda + \mu) \frac{\partial}{\partial x} \left(\frac{\partial v}{\partial x} + \frac{\partial v}{\partial y} + \frac{\partial v}{\partial z} \right) + \mu \left(\frac{\partial^2 v}{\partial x^2} + \frac{\partial^2 v}{\partial y^2} + \frac{\partial^2 v}{\partial z^2} \right) &= \rho \frac{\partial^2 v}{\partial t^2} \\
(\lambda + \mu) \frac{\partial}{\partial x} \left(\frac{\partial w}{\partial x} + \frac{\partial w}{\partial y} + \frac{\partial w}{\partial z} \right) + \mu \left(\frac{\partial^2 w}{\partial x^2} + \frac{\partial^2 w}{\partial y^2} + \frac{\partial^2 w}{\partial z^2} \right) &= \rho \frac{\partial^2 w}{\partial t^2}
\end{aligned} \tag{4.4}$$

Eqs. (4.1)-(4.4) are the classical theory of wave propagation. With the application of different boundary and initial conditions, individual wave solution can be obtained. For example, a Rayleigh wave occurs along the stress-free surface of a half-space, while a Lamb wave propagates along the space bounded between two stress-free boundaries. In this research, an isotropic, homogeneous thin plate is used as the specimen configuration, which supports the propagation of Lamb waves.

4.1.1. Lamb waves

Lamb waves are dispersive. The dispersion property of Lamb plate modes is explored in this research. Assuming the plate is very long in the y -direction, thus satisfying the plane-strain assumption. The 3D problem can be simplified to 2D by maintaining a thickness of $2b$ as shown in Fig. 4.2.

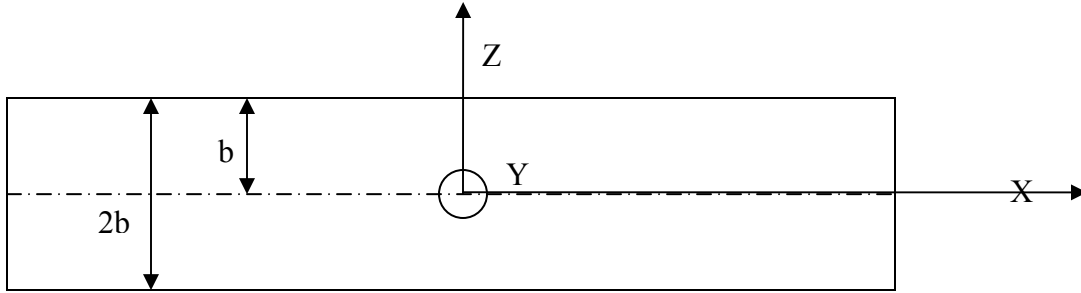


Fig. 4.2. Thin plate configuration

Since the upper and lower surfaces of the plate are traction free, the corresponding boundary conditions are therefore

$$\text{At } Z = \pm b, \sigma_{xz} = \sigma_{yz} = \sigma_{zz} = 0 \quad (4.5)$$

The plane strain assumptions are

$$\begin{aligned} u_x &= u_x(x, z, t) \\ u_z &= u_z(x, z, t) \\ u_y &= 0 \end{aligned}$$

where u_x , u_y and u_z are displacement components along the x , y and z directions, respectively. According to the Helmholtz Representation Theorem, the displacement vector (\vec{u}) can be expressed using two potential functions, ϕ and ψ , as

$$\vec{u} = \vec{\nabla} \phi + \vec{\nabla} \times \psi \quad (4.6)$$

Expanding Eq. (4.6), the displacement vector (\vec{u}) can be written as

$$\vec{u} = \left(\frac{\partial \phi}{\partial x} + \frac{\partial \psi}{\partial z} \right) \hat{i} + \left(\frac{\partial \phi}{\partial z} + \frac{\partial \psi}{\partial x} \right) \hat{k} \quad (4.7)$$

where \hat{i} and \hat{k} are the unit vectors along the x and z directions, respectively. With the plane-strain assumptions, the displacement components along the x and z directions can be expressed as functions of ϕ and ψ as follow:

$$\begin{aligned} u_x &= \left(\frac{\partial \phi}{\partial x} + \frac{\partial \psi}{\partial z} \right) \\ u_z &= \left(\frac{\partial \phi}{\partial z} + \frac{\partial \psi}{\partial x} \right) \end{aligned} \quad (4.8)$$

Substituting Eq. (4.8) into Eqs. (4.2) and (4.3), σ_{xz} , σ_{yz} , σ_{zz} can be expressed as functions of ϕ and ψ as

$$\begin{aligned} \sigma_{xz} &= \mu \left(2 \frac{\partial^2 \phi}{\partial x \partial z} + \frac{\partial^2 \psi}{\partial x^2} - \frac{\partial^2 \psi}{\partial z^2} \right) \\ \sigma_{yz} &= \mu \left(\frac{\partial \phi}{\partial y \partial z} + \frac{\partial \psi}{\partial x \partial y} \right) \\ \sigma_{zz} &= \lambda \left(\frac{\partial^2 \phi}{\partial x^2} + \frac{\partial^2 \phi}{\partial z^2} \right) + 2\mu \left(\frac{\partial^2 \phi}{\partial z^2} + \frac{\partial^2 \psi}{\partial x \partial z} \right) \end{aligned} \quad (4.9)$$

Substituting Eq. (4.9) into Eq. (4-4), one then has

$$\begin{aligned} \nabla^2 \phi &= \frac{1}{C_l^2} \frac{\partial^2 \phi}{\partial t^2} = \left(\frac{k_l}{\omega} \right)^2 \frac{\partial^2 \phi}{\partial t^2} \\ \nabla^2 \psi &= \frac{1}{C_t^2} \frac{\partial^2 \psi}{\partial t^2} = \left(\frac{k_t}{\omega} \right)^2 \frac{\partial^2 \psi}{\partial t^2} \end{aligned} \quad (4.10)$$

Where ω is the angular frequency, $k_l = \left(\omega \sqrt{\frac{\rho}{\lambda + 2\mu}} \right)$, $k_t = \left(\omega \sqrt{\frac{\rho}{\mu}} \right)$ are the wavenumbers of the longitudinal and transverse waves, respectively, and C_l and C_t are the group velocities of longitudinal and transverse waves, respectively. Assuming harmonic solutions for the potential functions ϕ and ψ

$$\begin{aligned} \phi(x, z, t) &= F(z) e^{i(kx - \omega t)} \\ \psi(x, z, t) &= G(z) e^{i(kx - \omega t)} \end{aligned} \quad (4.11)$$

where, again, k is the wavenumber and ω is the angular frequency.

Substituting Eq. (4.11) into Eq. (4.10),

$$\begin{aligned} F''(z) + (k_i^2 - k^2)F(z) &= 0 \\ G''(z) + (k_i^2 - k^2)G(z) &= 0 \end{aligned} \quad (4.12)$$

The general solution of Eqs. (4.12) are

$$\begin{aligned} F(z) &= A_1 \sin(qz) + A_2 \cos(qz) \\ G(z) &= B_1 \sin(sz) + B_2 \cos(sz) \end{aligned} \quad (4.13)$$

where A_1 , A_2 , B_1 and B_2 are arbitrary constants, $q = \sqrt{(k_i^2 - k^2)}$ and $s = \sqrt{(k_i^2 - k^2)}$.

Applying boundary conditions Eq. (4.5), the dispersion equations can then be obtained.

Due to the symmetry and anti-symmetry of the displacement equation, the solutions are separated into symmetric modes and anti-symmetric modes. Fig. 4.3 provides the corresponding mode shapes. Generally speaking, these two different modes depend on the symmetry of the configuration and the boundary conditions. For example, if the excitation at the upper surface and lower surface are symmetric, the symmetric mode will be excited. In contrast, the anti-symmetric mode will be excited if the excitation at the upper surface and lower surface are anti-symmetric.

The dispersion equation for the symmetric mode is

$$\frac{\tan(sb)}{\tan(qb)} = -\frac{4k^2qs}{(k^2 - s^2)^2} \quad (4.14)$$

and the dispersion equation for the anti-symmetric mode is

$$\frac{\tan(sb)}{\tan(qb)} = -\frac{(k^2 - s^2)^2}{4k^2qs} \quad (4.15)$$

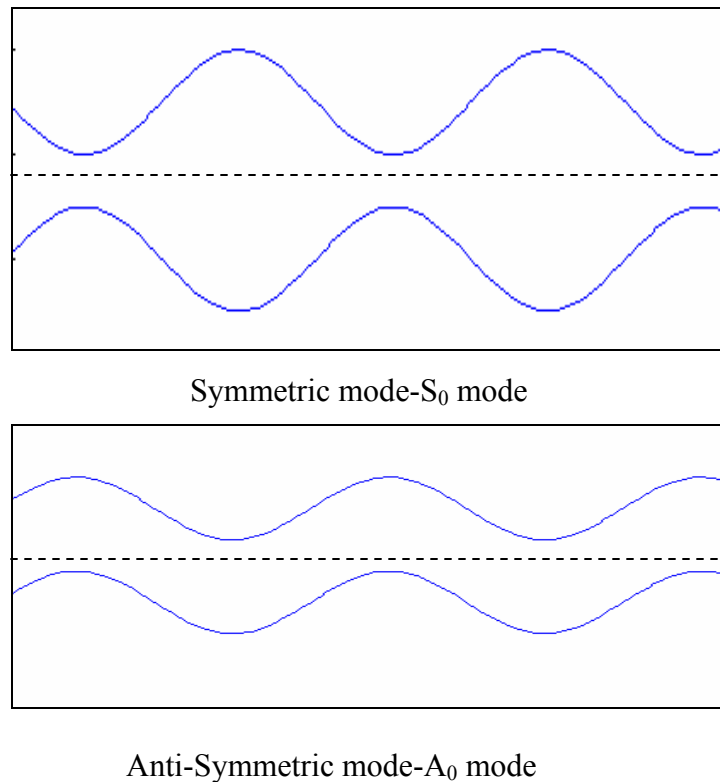


Fig. 4.3. Symmetric and anti-symmetric modes

4.1.2. Dispersion

Using the dispersion Eqs. (4.14) and (4.15), the dispersion curves for symmetric and anti-symmetric modes can be obtained. Dispersion curves can be obtained either through solving the dispersion equation or via processing waveform responses for dispersion extraction. As it is difficult to obtain close-form wave solutions, this research adopts the latter approach for extracting dispersion information from numerical waveforms. Wave dispersion is associated with the time and frequency of a waveform. Different waveform responses reflect different dispersion phenomena. Consider a 0.5mm aluminum alloy 6061 plate with an anti-symmetric impulse forcing function. The boundary conditions are the same as described in Eq. (4.5). An anti-symmetric Lamb wave will result through solving Eq. (4.4). The anti-symmetric waveforms acquired at locations 15mm, 25mm and 35mm away from the point of excitation are shown in Figs.

4.4, 4.5 and 4.6, respectively. The resulted waveforms, though looked similar, are of different shape, indicating that all frequency components of the Lamb wave propagate at different velocities. This phenomenon is called dispersion. On the other hand, if the waves are nondispersive, the group velocities of all spectral components are the same and the waveform maintains the same at all time. In mathematical terms, when the group velocity of the wave is a nonlinear function of frequency, the wave is dispersive. Otherwise, the wave is nondispersive. By using Gabor wavelet transform, dispersive waveforms can be mapped into the time-frequency domain, and from which the relation between frequency and group velocity can then be determined. Plotting of the relation is a dispersion curve.

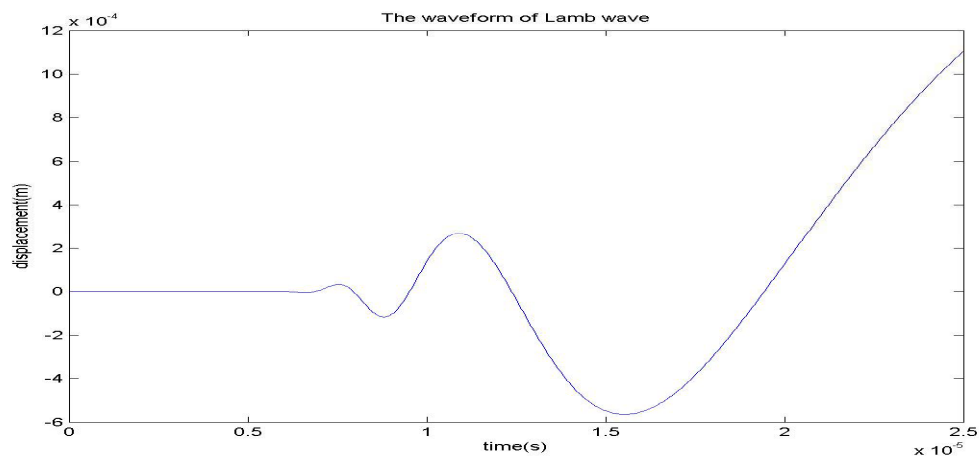


Fig. 4.4. Lamb waveform acquired at 15mm from the excitation point

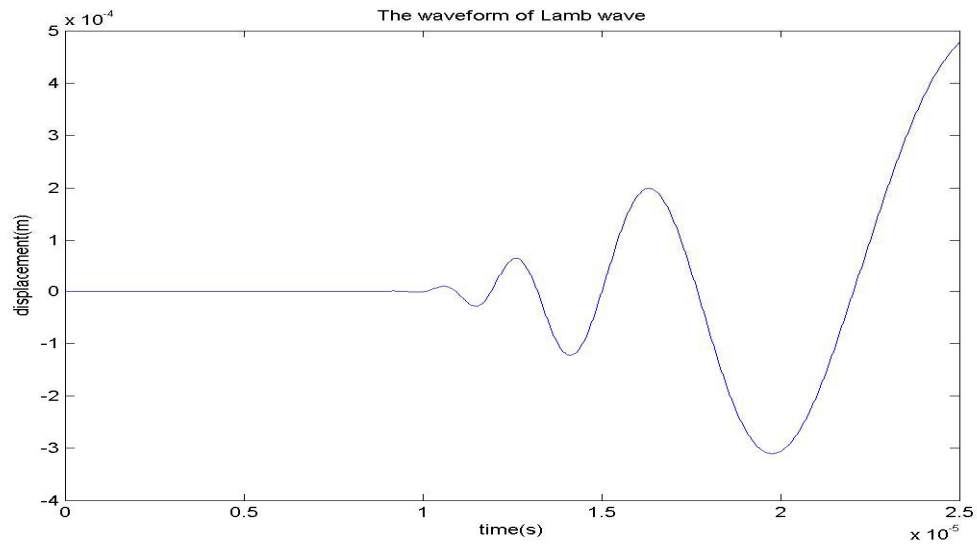


Fig. 4.5. Lamb waveform acquired at 25mm from the excitation point

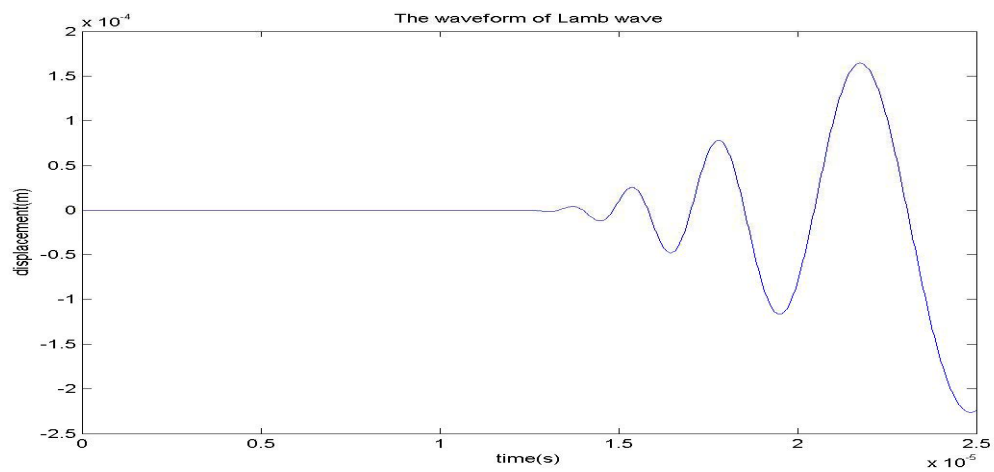


Fig. 4.6. Lamb waveform acquired at 35mm from the excitation point

4.2. Wavelet Transform

Wavelet transform is used to process the wave solutions obtained from numerically solving the theoretical model that is to be derived in the following section. The reason for using Wavelet Transform instead of Fourier Transform is illustrated through

comparing the two mathematical transformations. A time signal, $x(t)$, can be represented using a series of exponential functions of different frequencies as

$$X(f) = \int_{-\infty}^{\infty} x(t)e^{-i\omega t} dt \quad (4.16)$$

where $X(f)$ is the Fourier Transform of the signal $x(t)$ in the frequency domain. By applying the Fourier Transform, the frequency components of a time signal are resolved. However, the major drawback of the Fourier transform is that time domain information of the signal is lost through the transformation. As an alternative, wavelet transform provides both time and frequency information [19]. As such wavelet transform is the preferred tool for processing transient signals. Wavelet transform maps a time signal into the time-frequency domain by analyzing a small section of the signal at a given time. The continuous wavelet transform is defined as

$$W(a,b) = \frac{1}{\sqrt{a}} \int_{-\infty}^{\infty} f(t)\overline{\psi\left(\frac{t-b}{a}\right)} dt \quad (4.17)$$

Where a is a scale parameter, b is a translation parameter and $f(t)$ is a time signal. $\psi(t)$ is the analyzing wavelet function and the over-bar, $\overline{}$, represents the complex conjugate. From Eq. (4.17) it can be seen that wavelet transform is the inner product of a time signal with the analyzing mother wavelet function, ψ . Parameters \mathbf{a} and \mathbf{b} control the shape and location in time of the mother wavelet, respectively. Figs. 4.7-4.9 illustrate 3 different Gabor wavelet functions correspond to 3 sets of \mathbf{a} and \mathbf{b} . Fig. 4.7 shows that the Gabor wavelet function when $a=1$ and $b=0$, which corresponds to no dilatation or translation. Fig. 4.8 is the case there is translation but no dilatation. Fig. 4.9 is when there is compression but no translation.

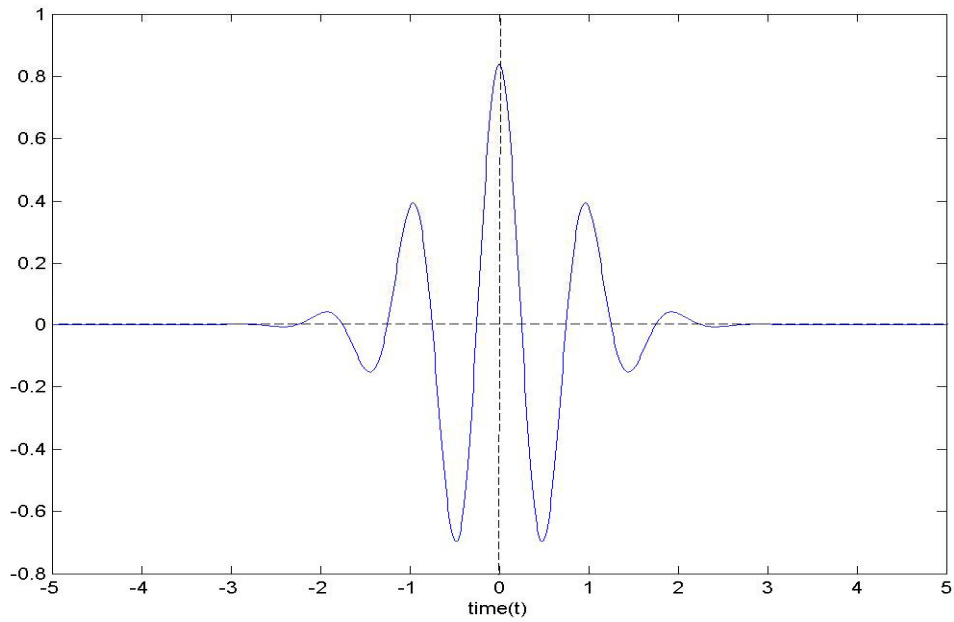


Fig. 4.7. Gabor wavelet function corresponds to $a=1$ and $b=0$

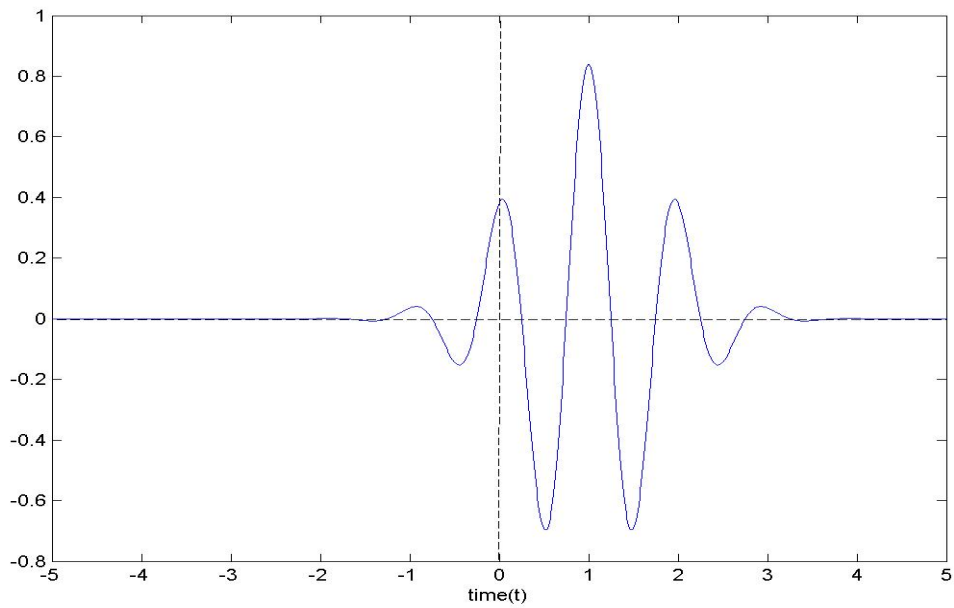


Fig. 4.8. Gabor wavelet function corresponds to $a=1$ and $b=1$

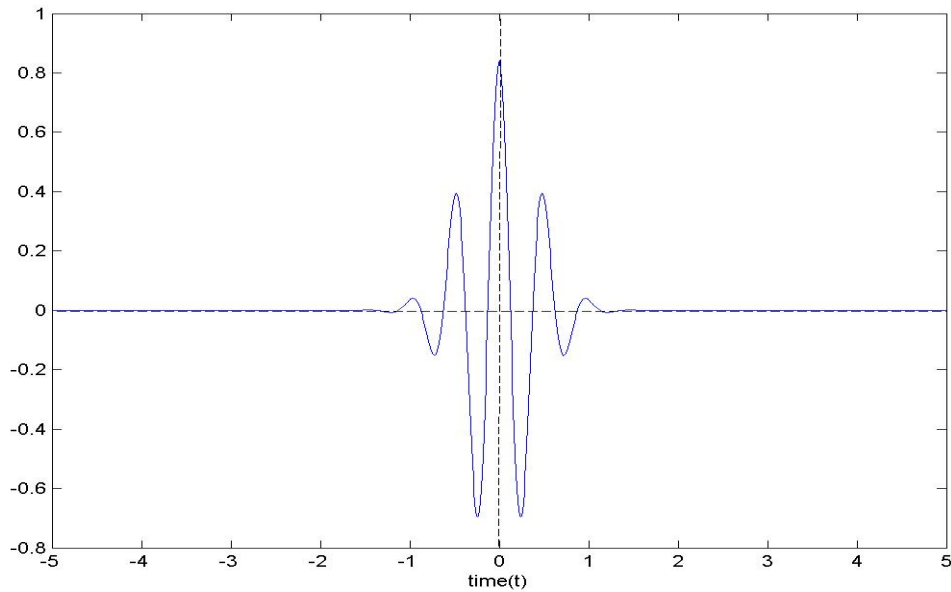


Fig. 4.9. Gabor wavelet function corresponds to $a=0.5$ and $b=0$

From the above figures, it is seen that \mathbf{a} causes dilatation of the wavelet function when $\mathbf{a}>1$ and compression of the function when $\mathbf{a}<1$. \mathbf{b} , on the other hand, causes the translation of the mother wavelet in time. Thus a time signal is approximated along the time axis within a window of changing size. Strictly speaking the wavelet transform domain is a time-scale domain. However, since parameter \mathbf{a} implies frequency, wavelet transform can be applied to resolve simultaneous time-frequency information. It should be noted that a wavelet function possesses specific characteristics [20]. First, wavelet function, $\psi(t)$, must have an average of zero. That is,

$$\int_{-\infty}^{\infty} \psi(t) dt = 0 \quad (4.18)$$

Second, the wavelet $\psi(t)$ must satisfy the admissibility condition requiring that $\psi(t)$ and its Fourier Transform, $\hat{\psi}(\omega)$, must satisfy

$$\int_{-\infty}^{\infty} |t\psi(t)|^2 dt < \infty \quad (4.19)$$

and

$$\int_{-\infty}^{\infty} |\omega \hat{\psi}(\omega)|^2 d\omega < \infty \quad (4.20)$$

where ω is the angular frequency. Gabor function is used as the mother wavelet in this research. Wavelet Transform that employs Gabor function is therefore named the Gabor Wavelet Transform (GWT).

4.2.1. Gabor wavelet transform

The Gabor wavelet function found in Eq. (4.21) and plotted in Fig. 4.10 is a complex-valued sinusoidal function windowed by a Gaussian function centered at the origin. The Fourier Transform of the Gabor function is a Gaussian function centered at $\omega = \omega_0$.

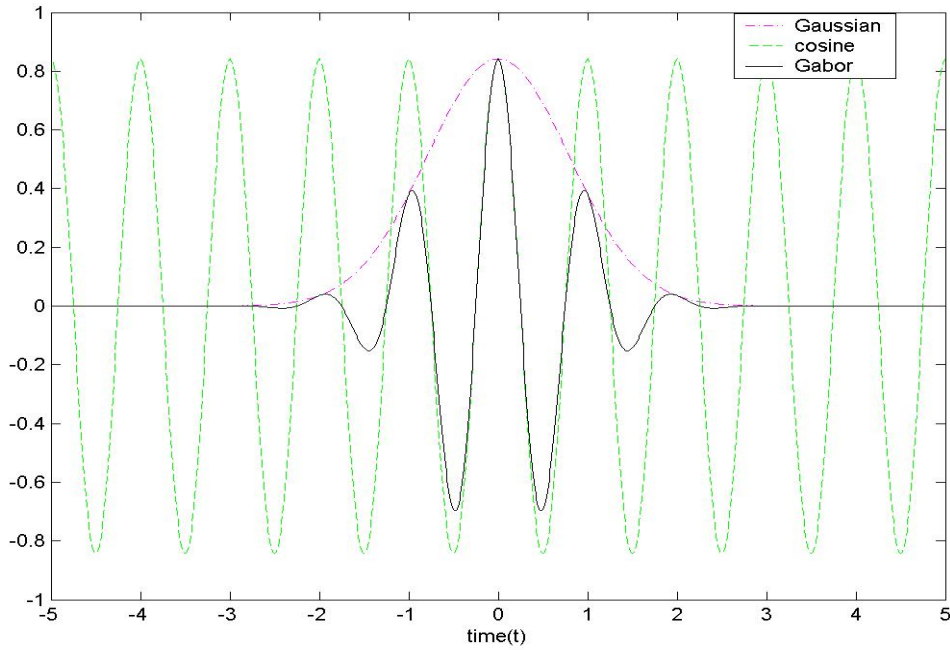


Fig. 4.10. Gabor Wavelet Function consists of a complex-valued sinusoidal

$$\psi_G(t) = \frac{1}{\sqrt[4]{\pi}} \sqrt{\frac{\omega_0}{\gamma}} \exp\left[-\frac{(\omega_0/\gamma)^2}{2} t^2 + i\omega_0 t\right] \quad (4.21)$$

where ω_0 and γ are positive constants. In this research, ω_0 is set to 2π and $\gamma=3$. The reasons for choosing these two numbers are explained in [20].

A Matlab Gabor wavelet transform program was developed for processing numerical wave solutions. A Matlab Fourier Transform program was also developed for the purpose of comparison. The example that follows illustrates the reason why wavelet transform is preferred over Fourier transform for analyzing transient signals. Consider Signals A and B shown in Figs. 4.11 and 4.12, respectively. Signal A has two frequencies, 1 Hz and 2 Hz, in a time-span of 5 seconds. Signal B has a 1 Hz component in the first 3 seconds and a 2 Hz frequency in the next 2 seconds. Figs. 4.13 and 4.14 show the Fourier Transform and Gabor Wavelet Transform of Signal A; while Figs. 4.15 and 4.16 present the corresponding transforms of Signal B. For Signal A, both Fourier Transform and Gabor Wavelet Transform resolve the frequency components of the signal. However, for Signal B, only the Gabor Wavelet Transform can clearly resolve the frequency components at the two different time intervals.

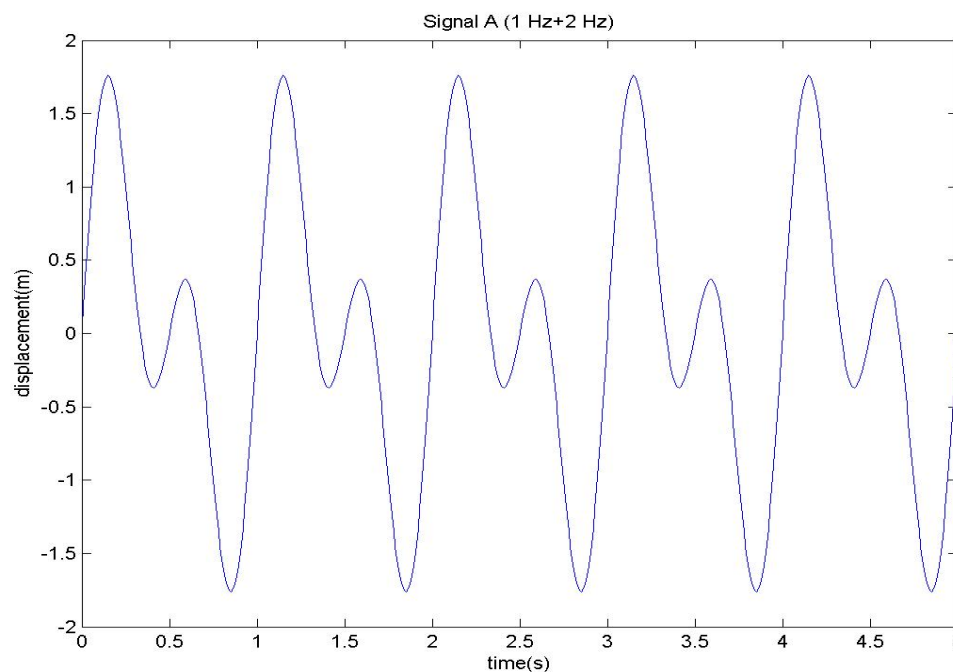


Fig. 4.11. Signal A with the sum of two frequencies: 1 Hz and 2 Hz during a time span of 5 seconds

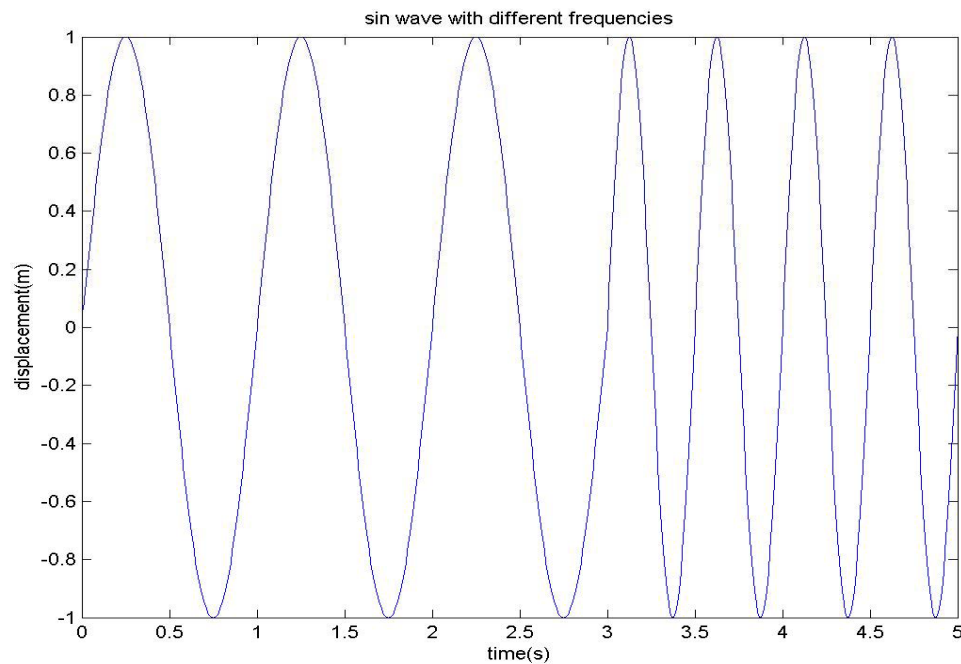


Fig. 4.12. Signal B during two intervals: 1 Hz from 0-3 second and 2 Hz from 3-5 seconds

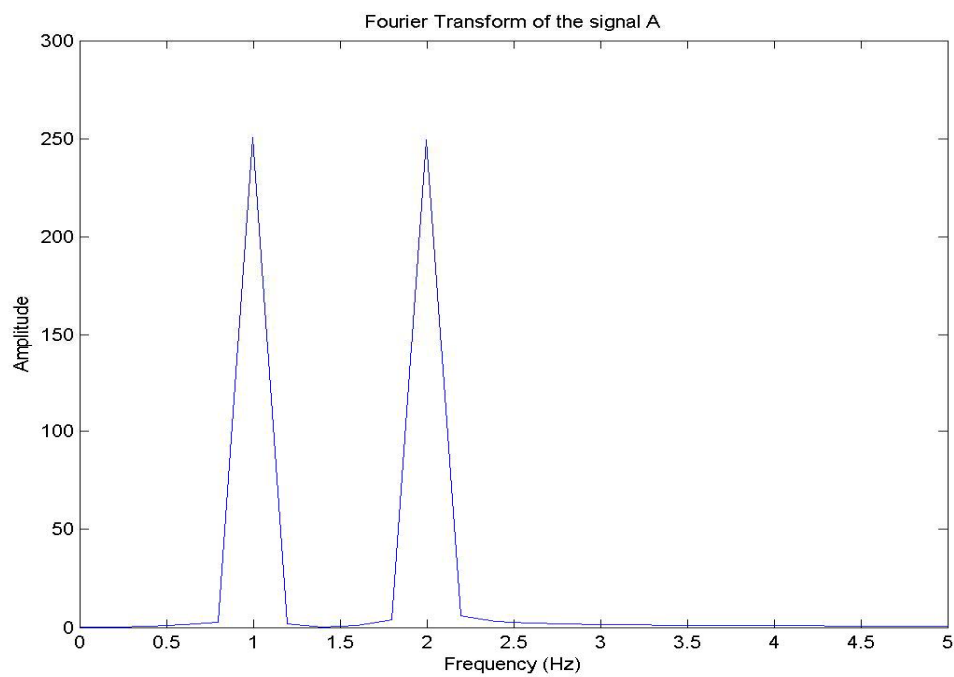


Fig. 4.13. Fourier transform of signal A

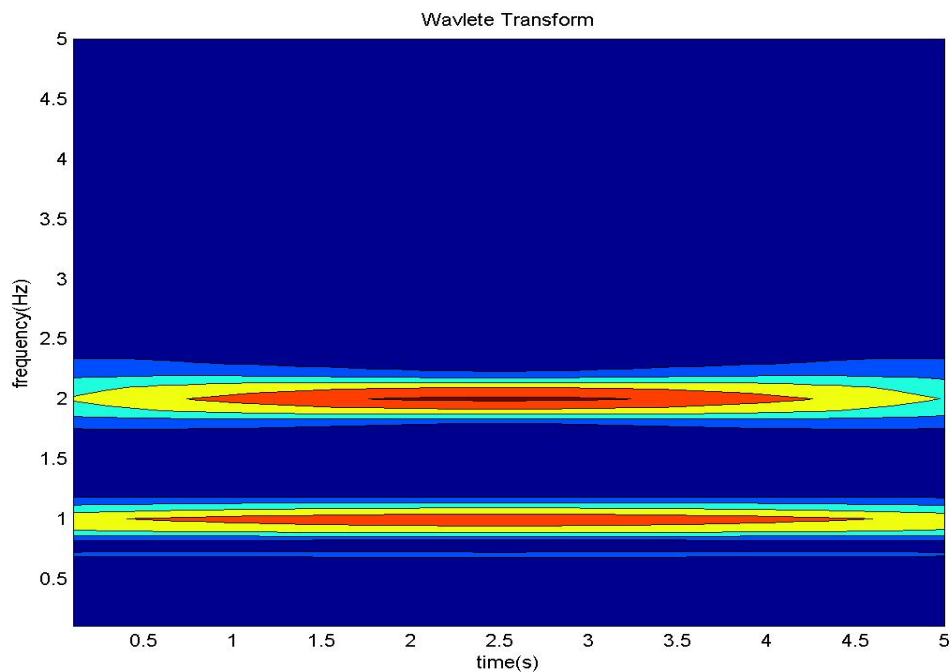


Fig. 4.14. Gabor wavelet transform of signal A

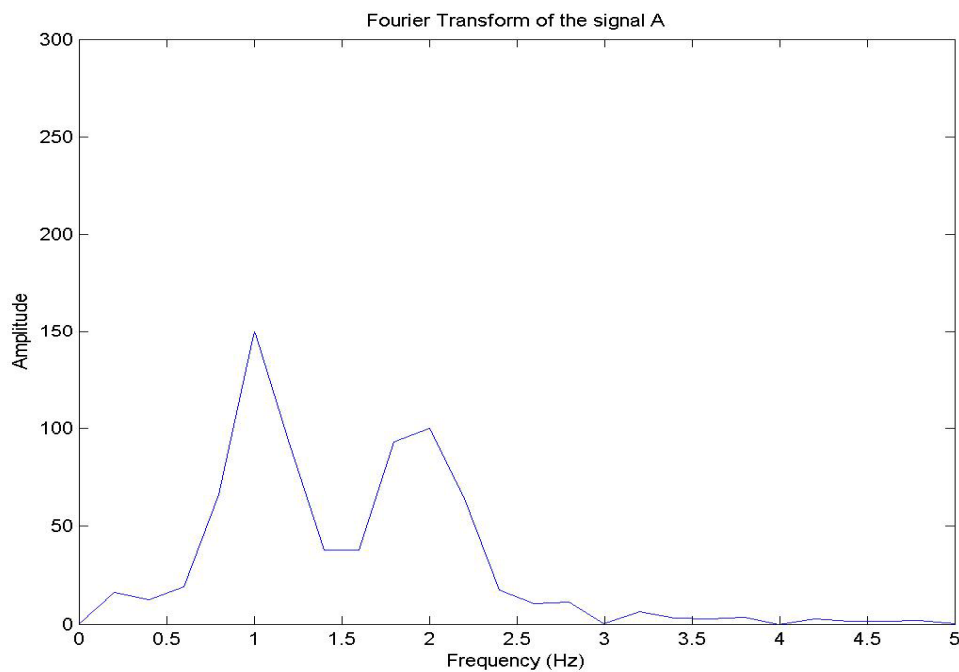


Fig. 4.15. Fourier transform of signal B

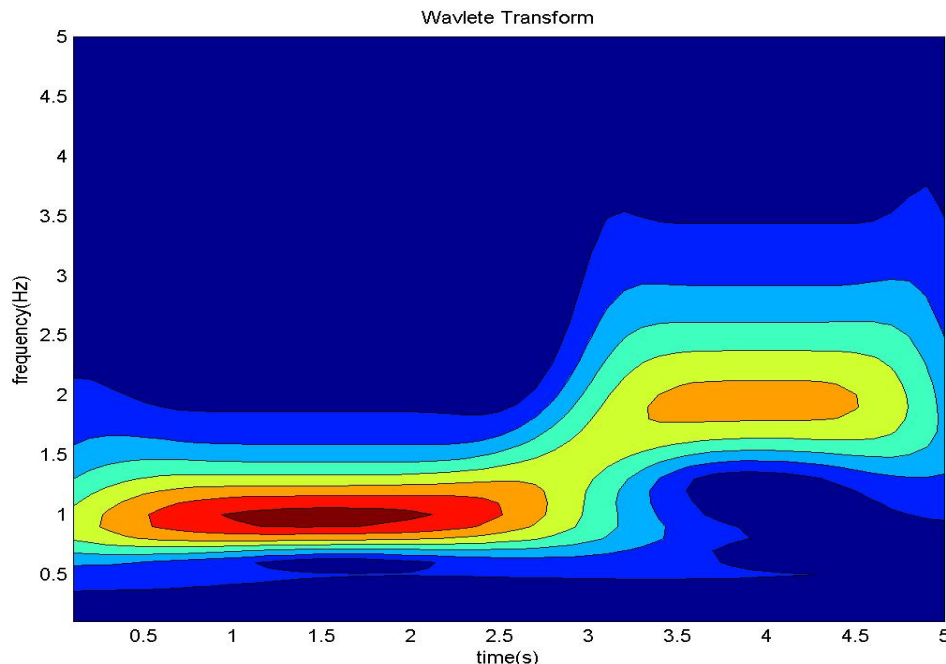


Fig. 4.16. Gabor wavelet transform of signal B

4.3. Modified Equations of Wave Propagation for 2-D, Isotropic, Homogenous Materials

A modified wave formulation is derived based on the classical wave propagation theory and elasticity. The goal is to incorporate temperature and pressure effects into the displacement based formulation. Temperature effects would result in thermal stresses and pressure would cause mechanical stresses. In other words, stress wave propagation can be correlated with temperature and pressure induced pre-stresses. Thus, the relation of displacement with thermal and mechanical pre-stresses is sought in the study.

To derive the modified formulation, three states are defined as shown in Fig. 4.17. First, non-deformed state is the initial state experiencing no deformation. In addition, the assumed position vector is expressed as capital X_I , and the tensors subscripts are expressed as capital letters I, J, K, L, M and N. Secondly, deformed state is defined as the deformed configuration after pressure is applied and pre-stress is resulted. The position vector is expressed as x_i which is a function of the reference (non-deformed state) position vector X_I . The associated tensors are expressed as letters i, j, k, l, m and n.

Thirdly, final state is defined as a secondary deformed configuration after excitation and temperature are both applied. In general, wave propagation occurs between the deformed state and the final state. The position vector is expressed as \underline{X}_α which is a function of deformed position vector, x_i , and the tensors are expressed as Greek letters $\alpha, \beta, \gamma, \delta, \varepsilon$ and η .

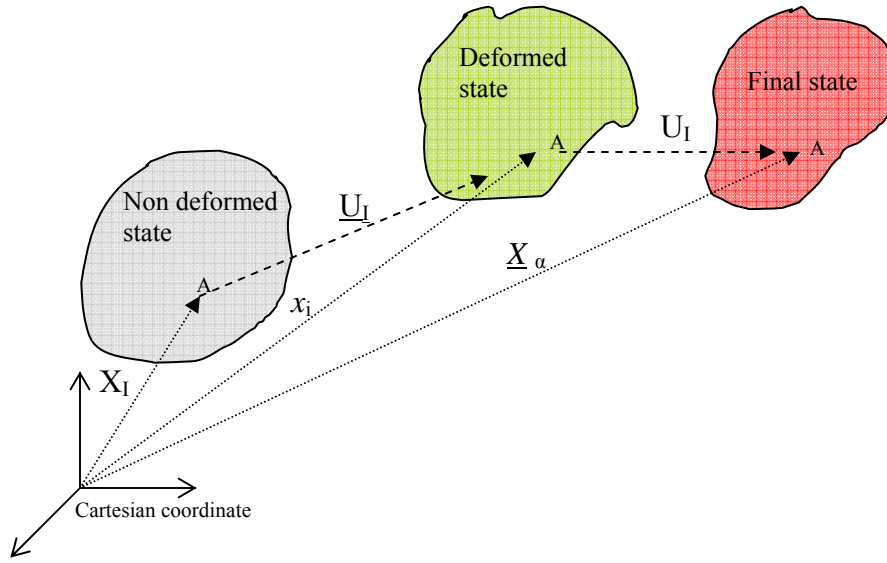


Fig. 4.17. Three different states in cartesian coordinate system

\underline{U}_I is the displacement vector from the non-deformed state to deformed state which can be expressed as $\underline{U}_I = x_i - X_i$. U_I is the displacement vector from the deformed state to final state which can be expressed as $U_I = \underline{X}_i - x_i$. Stresses in the deformed state is denoted as $\sigma_{ij}^{deformed}$ and stresses in the final state as $\sigma_{\alpha\beta}^{final}$. The density in the non-deformed, deformed, and final state are denoted as $\rho, \rho^{deformed}$ and ρ^{final} , respectively. Since the deformed state is a static state, the equilibrium equations [24] in the deformed state are therefore $\sigma_{ij,i}^{deformed} = 0$ (4.22)

Since the final state is a transient state, the final state can be written according to [11] as

$$\sigma_{\alpha\beta,\alpha}^{final} = \rho^{final} \ddot{U}_\beta \quad (4.23)$$

Eqs. (4.22) and (4.23) are in spatial description, and in order to relate the two equations, Eq. (4.23) needs to be in material description. Hence, $\sigma_{\alpha\beta}^{final}$ can be expressed in terms of the second Piola-Kirchhoff stress tensor, S_{ij}^{final} , as [24]

$$S_{ij}^{final} = J F^{-1} \sigma_{\alpha\beta}^{final} F^{-T} \quad (4.24)$$

where J is the Jacobian of the motion from the deformed configuration at $t = t_0$ to the final configuration, and F is the deformation gradient tensor.

Since $d\vec{X} = F d\vec{x}$, $F_{\alpha i} = \frac{dX_{\alpha}}{dx_i}$, Eq. (4.24) can be written as

$$\sigma_{\alpha\beta}^{final} = \frac{1}{J} X_{\alpha,i} X_{\beta,j} S_{ij}^{final} \quad \text{or} \quad \sigma_{\alpha\beta}^{final} = \frac{1}{J} \frac{\partial X_{\alpha}}{\partial x_i} \frac{\partial X_{\beta}}{\partial x_j} S_{ij}^{final} \quad (4.25)$$

Similarly, $\sigma_{ij}^{deformed}$ can be expressed in terms of the second Piola-Kirchhoff stress tensor, $S_{IJ}^{deformed}$, as [24]

$$S_{IJ}^{deformed} = J' F^{-1} \sigma_{ij}^{deformed} F^{-T} \quad (4.26)$$

where J' is the Jacobian of the motion from the non-deformed configuration to the deformed configuration, and F is the deformation gradient tensor.

Since $d\vec{x} = F d\vec{X}$, $F_{iI} = \frac{dx_i}{dX_I}$, Eq. (4.26) can be written as

$$\sigma_{ij}^{deformed} = \frac{1}{J'} x_{i,I} x_{j,J} S_{IJ}^{deformed} \quad \text{or} \quad \sigma_{ij}^{deformed} = \frac{1}{J'} \frac{\partial x_i}{\partial X_I} \frac{\partial x_j}{\partial X_J} S_{IJ}^{deformed} \quad (4.27)$$

For incompressible material, the relation between the density of the material in the deformed state and in the final state is given as follows [24]

$$\rho^{deformed} = J \rho^{final}$$

where

$$J = \frac{1}{1 - U_{k,k}} \quad (4.28)$$

$$\rho = J' \rho^{deformed}$$

$$J' = \frac{1}{1 - U_{K,K}} \quad (4.29)$$

The increment of the stress tensor S_{ij} is defined in the deformed state coordinates as [12]

$$S_{ij} = S_{ij}^{final} - \sigma_{ij}^{deformed} \quad (4.30)$$

or in the non-deformed state coordinates as

$$S_{IJ} = S_{IJ}^{final} - S_{IJ}^{deformed} \quad (4.31)$$

For linear elastic materials, and assuming infinitesimal deformation, the constitutive equations can be written as follow [24]

$$S_{IJ}^{deformed} = C_{IJKL} E_{KL}^{deformed} + C_{IJKL} \alpha \theta_{KL} \quad (4.32)$$

$$S_{IJ}^{final} = C_{IJKL} E_{KL}^{final} \quad (4.33)$$

where C_{IJKL} is the second order elastic constants, and $E_{KL}^{deformed}$ and E_{KL}^{final} are the Lagrange finite strain tensors in the deformed and final states, respectively. α is the thermal expansion coefficient, and θ_{KL} is the temperature tensor. Substituting Eqs. (4.32) and (4.33) into (4.31), S_{IJ} can be expressed as

$$S_{IJ} = C_{IJKL} \left(E_{KL}^{final} - E_{KL}^{deformed} - \alpha \theta_{KL} \right)$$

$$E_{KL}^{deformed} = \frac{1}{2} (\underline{U}_{K,L} + \underline{U}_{L,k}) \quad (4.34)$$

$$E_{kl}^{final} = \frac{1}{2} (U_{k,l} + U_{l,k})$$

Substituting Eqs. (4.34) and (4.28) into (4.27), S_{ij} can be written in the following form

$$S_{ij} = C'_{ijkl} U_{k,l} - C_{ijkl} \alpha \theta_{kl} \quad (4.35)$$

Using the chain rule and neglecting higher order terms, C'_{ijkl} can be written as a function of \underline{U} which is the pressure-induced initial displacement

$$C'_{ijkl} = C_{ijkl} (1 - \underline{U}_{M,M}) + C_{ijkm} \underline{U}_{l,m} + C_{ijml} \underline{U}_{k,m} + C_{imkl} \underline{U}_{j,m} + C_{mjkl} \underline{U}_{i,m} \quad (4.36)$$

Substituting Eq. (4.25) into (4.23) and using the chain rule, one has

$$\frac{\partial \underline{X}_k}{\partial x_j} \frac{\partial S_{ij}^{final}}{\partial x_i} = \rho^{deformed} \ddot{U}_k \quad (4.37)$$

Since $U_k = \underline{X}_k - x_k$, Eq. (4.37) becomes

$$\frac{\partial}{\partial x_i} \left(\frac{\partial U_k}{\partial x_j} S_{ij}^{final} + S_{ik}^{final} \right) = \rho^{deformed} \ddot{U}_k \quad (4.38)$$

Substituting j with l and k with j, Eq. (4.38) becomes

$$\frac{\partial}{\partial x_i} \left(\frac{\partial U_j}{\partial x_l} S_{il}^{final} + S_{ij}^{final} \right) = \rho^{deformed} \ddot{U}_j \quad (4.39)$$

Substituting Eq. (4.30) into (4.39), the following results

$$\frac{\partial}{\partial x_i} \left(\frac{\partial U_j}{\partial x_l} (S_{il} + \sigma_{il}^{deformed}) + \sigma_{ij}^{deformed} + S_{ij} \right) = 0 \quad (4.40)$$

Since small deformation is assumed, the product of $\frac{\partial U_j}{\partial x_l}$ with S_{il} are very small so that it

can be neglected. Since $\frac{\partial}{\partial x_i} (\sigma_{ij}^{deformed}) = 0$ (see Eq. (4.22)), Eq. (4.40) becomes

$$\frac{\partial}{\partial x_i} \left(\frac{\partial U_j}{\partial x_l} S_{il} + S_{ij} \right) = 0 \quad (4.41)$$

Substituting Eq. (4.35) into (4.41), Eq. (4.42) is obtained

$$(C'_{ijkl} + \delta_{jk} \sigma_{il}^{deformed}) U_{k,li} - C_{ijkl} \alpha \theta_{kl,i} = \rho^{deformed} \ddot{U}_j \quad (4.42)$$

Combining Eqs. (4.42) and (4.29), Eq. (4.21) can be written in the following form

$$B_{ijkl} U_{k,li} - C_{ijkl} \alpha \theta_{kl,i} = (1 - \underline{U}_{m,m}) \rho \ddot{U}_j \quad (4.43)$$

where $B_{ijkl} = C'_{ijkl} + \delta_{jk} \sigma_{il}^{deformed}$. The equations of wave propagation incorporating pre-stress and temperature were derived in Eq. (4.43). Next, the formulation is simplified to account for isotropic, homogenous materials subject to plane strain conditions. Models created using the 2D formulation are then used to simulate stress wave propagation in thin plates.

Eq. (4.43) is derived for anisotropic materials. To consider isotropic materials, Eq. (4.43) needs be simplified. All isotropic fourth-order tensors have scalar components of the following form [24]

$$C_{ijkl} = \lambda \delta_{ij} \delta_{kl} + \mu \delta_{ik} \delta_{jl} + \mu \delta_{il} \delta_{jk} \quad (4.44)$$

where λ and μ are independent elastic constants called *Lam'e* constants. Substituting Eq. (4.44) into (4.36), C'_{ijkl} can be expressed using *Lam'e* constants as

$$\begin{aligned} C'_{ijkl} = & \left(\lambda \delta_{ij} \delta_{kl} + \mu \delta_{ik} \delta_{jl} + \mu \delta_{il} \delta_{jk} \right) \left(1 - \underline{U}_{M,M} \right) + \left(\lambda \delta_{ij} \underline{U}_{l,k} + \mu \delta_{ik} \underline{U}_{l,j} + \mu \delta_{jk} \underline{U}_{l,i} \right) \\ & + \left(\lambda \delta_{ij} \underline{U}_{k,l} + \mu \delta_{jl} \underline{U}_{k,i} + \mu \delta_{il} \underline{U}_{k,j} \right) + \left(\lambda \delta_{kl} \underline{U}_{j,i} + \mu \delta_{ik} \underline{U}_{j,l} + \mu \delta_{il} \underline{U}_{j,k} \right) \\ & + \left(\lambda \delta_{kl} \underline{U}_{i,j} + \mu \delta_{jl} \underline{U}_{i,k} + \mu \delta_{jk} \underline{U}_{i,l} \right) \end{aligned} \quad (4.45)$$

For 2-D problems, $i, j, k, l, m = 1$ or 2 and C'_{ijkl} can be written as a 4×4 matrix as

$$C'_{ijkl} = \begin{bmatrix} C'_{1111} & C'_{1112} & C'_{1121} & C'_{1122} \\ C'_{2111} & C'_{2112} & C'_{2121} & C'_{2122} \\ C'_{1211} & C'_{1212} & C'_{1221} & C'_{1222} \\ C'_{2211} & C'_{2212} & C'_{2221} & C'_{2222} \end{bmatrix} \quad (4.46)$$

where

$$C'_{1111} = (\lambda + 2\mu)(3\underline{U}_{1,1} - \underline{U}_{2,2} + 1)$$

$$C'_{1112} = (\lambda + 2\mu)(\underline{U}_{1,2} + \underline{U}_{2,1})$$

$$C'_{1121} = (\lambda + 2\mu)(\underline{U}_{1,2} + \underline{U}_{2,1})$$

$$C'_{1122} = \lambda(\underline{U}_{1,1} + \underline{U}_{2,2} + 1)$$

$$C'_{2111} = (\lambda + 2\mu)(\underline{U}_{1,2} + \underline{U}_{2,1})$$

$$C'_{2112} = \mu(\underline{U}_{1,1} + \underline{U}_{2,2} + 1)$$

$$C'_{2121} = \mu(\underline{U}_{1,1} + \underline{U}_{2,2} + 1)$$

$$C'_{2122} = (\lambda + 2\mu)(\underline{U}_{1,2} + \underline{U}_{2,1})$$

$$C'_{1211} = (\lambda + 2\mu)(\underline{U}_{1,2} + \underline{U}_{2,1})$$

$$C'_{1212} = \mu(\underline{U}_{1,1} + \underline{U}_{2,2} + 1)$$

$$C'_{1221} = \mu(\underline{U}_{1,1} + \underline{U}_{2,2} + 1)$$

$$C'_{1222} = (\lambda + 2\mu)(\underline{U}_{1,2} + \underline{U}_{2,1})$$

$$C'_{2211} = \lambda(\underline{U}_{1,1} + \underline{U}_{2,2} + 1)$$

$$C'_{2212} = (\lambda + 2\mu)(\underline{U}_{1,2} + \underline{U}_{2,1})$$

$$C'_{2221} = (\lambda + 2\mu)(\underline{U}_{1,2} + \underline{U}_{2,1})$$

$$C'_{2222} = (\lambda + 2\mu)(-\underline{U}_{1,1} + 3\underline{U}_{2,2} + 1)$$

Similarly, B_{ijkl} can be written as a 4×4 matrix

$$B_{ijkl} = \begin{bmatrix} B_{1111} & B_{1112} & B_{1121} & B_{1122} \\ B_{2111} & B_{2112} & B_{2121} & B_{2122} \\ B_{1211} & B_{1212} & B_{1221} & B_{1222} \\ B_{2211} & B_{2212} & B_{2221} & B_{2222} \end{bmatrix} = \begin{bmatrix} C'_{1111} + \sigma_{11}^{deformed} & C'_{1112} + \sigma_{12}^{deformed} & C'_{1121} & C'_{1122} \\ C'_{2111} + \sigma_{21}^{deformed} & C'_{2112} + \sigma_{22}^{deformed} & C'_{2121} & C'_{2122} \\ C'_{1211} & C'_{1212} & C'_{1221} + \sigma_{11}^{deformed} & C'_{1222} + \sigma_{12}^{deformed} \\ C'_{2211} & C'_{2212} & C'_{2221} + \sigma_{21}^{deformed} & C'_{2222} + \sigma_{22}^{deformed} \end{bmatrix} \quad (4.47)$$

From the non-deformed state to the deformed state, $\sigma_{ij}^{deformed}$ can be written as the function of \underline{U}

$$\sigma_{il}^{deformed} = \mu(\underline{U}_{i,l}^{deformed} + \underline{U}_{l,i}^{deformed}) + \lambda(\underline{U}_{k,k}^{deformed})\delta_{il} - \beta\theta\delta_{il} \quad (4.48)$$

where λ and μ Lamé constants and $\beta = \alpha(3\lambda + 2\mu)$ with α being the thermal expansion coefficient. Combining Eqs. (4.46)-(4.48), B_{ijkl} can be written as follows

$$B_{ijkl} = \begin{bmatrix} B_{1111} & B_{1112} & B_{1121} & B_{1122} \\ B_{2111} & B_{2112} & B_{2121} & B_{2122} \\ B_{1211} & B_{1212} & B_{1221} & B_{1222} \\ B_{2211} & B_{2212} & B_{2221} & B_{2222} \end{bmatrix} \quad (4.49)$$

where

$$B_{1111} = (\lambda + 2\mu)(3\underline{U}_{1,1} - \underline{U}_{2,2} + 1) + 2\mu\underline{U}_{1,1} + \lambda(\underline{U}_{1,1} + \underline{U}_{2,2}) - \beta\theta$$

$$B_{1112} = (\lambda + 2\mu)(\underline{U}_{1,2} + \underline{U}_{2,1}) + \mu(\underline{U}_{1,2} + \underline{U}_{2,1})$$

$$B_{1121} = (\lambda + 2\mu)(\underline{U}_{1,2} + \underline{U}_{2,1})$$

$$B_{1122} = \lambda(\underline{U}_{1,1} + \underline{U}_{2,2} + 1)$$

$$B_{2111} = (\lambda + 2\mu)(\underline{U}_{1,2} + \underline{U}_{2,1}) + \mu(\underline{U}_{1,2} + \underline{U}_{2,1})$$

$$B_{2112} = \mu(\underline{U}_{1,1} + \underline{U}_{2,2} + 1) + 2\mu\underline{U}_{2,2} + \lambda(\underline{U}_{1,1} + \underline{U}_{2,2}) - \beta\theta$$

$$B_{2121} = \mu(\underline{U}_{1,1} + \underline{U}_{2,2} + 1)$$

$$B_{2122} = (\lambda + 2\mu)(\underline{U}_{1,2} + \underline{U}_{2,1})$$

$$B_{1211} = (\lambda + 2\mu)(\underline{U}_{1,2} + \underline{U}_{2,1})$$

$$B_{1212} = \mu(\underline{U}_{1,1} + \underline{U}_{2,2} + 1)$$

$$B_{1221} = \mu(\underline{U}_{1,1} + \underline{U}_{2,2} + 1) + 2\mu\underline{U}_{1,1} + \lambda(\underline{U}_{1,1} + \underline{U}_{2,2}) - \beta\theta$$

$$B_{1222} = (\lambda + 2\mu)(\underline{U}_{1,2} + \underline{U}_{2,1}) + \mu(\underline{U}_{1,2} + \underline{U}_{2,1})$$

$$B_{2211} = \lambda(\underline{U}_{1,1} + \underline{U}_{2,2} + 1)$$

$$B_{2212} = (\lambda + 2\mu)(\underline{U}_{1,2} + \underline{U}_{2,1})$$

$$B_{2221} = (\lambda + 2\mu)(\underline{U}_{1,2} + \underline{U}_{2,1}) + \mu(\underline{U}_{1,2} + \underline{U}_{2,1})$$

$$B_{2222} = (\lambda + 2\mu)(-\underline{U}_{1,1} + 3\underline{U}_{2,2} + 1) + 2\mu\underline{U}_{2,2} + \lambda(\underline{U}_{1,1} + \underline{U}_{2,2}) - \beta\theta$$

4.4. 2D Theoretical Model

There are four primary variables that need to be defined: U_1 and U_2 are the displacements along the X and Y directions from the non-deformed state to the deformed state, and \underline{U}_1 and \underline{U}_2 are the corresponding displacements from the deformed state to the

final state. The *Lam'e* -Navier equations that governs the state change from the non-deformed to the deformed state is [24]

$$(\lambda + \mu)U_{k,ki} + \mu U_{i,jj} = 0 \quad (4.50)$$

The equations governing the transient state change from the deformed to the final state as Eq. (4.44) is

$$B_{ijkl}U_{k,li} - C_{ijkl}\alpha\theta_{kl,i} = (1 - \underline{U}_{m,m})\rho\ddot{U}_j \quad (4.51)$$

Since the temperature varies uniformly, the term $C_{ijkl}\alpha\theta_{kl,i}$ is zero. Eq. (4.51) can be further simplified as

$$B_{ijkl}U_{k,li} = (1 - \underline{U}_{m,m})\rho\ddot{U}_j \quad (4.52)$$

Eqs. (4.50) and (4.52) are the governing equations for plane strain problems and can be expressed in four equations and four primary variables. From the non-deformed state to the deformed state, the governing equations can be written as follow

$$(\lambda + 2\mu)\frac{\partial^2 U_1}{\partial x^2} + (\lambda + \mu)\frac{\partial^2 U_2}{\partial y\partial x} + \mu\frac{\partial^2 U_1}{\partial y^2} = 0 \quad (4.53)$$

$$(\lambda + 2\mu)\frac{\partial^2 U_2}{\partial y^2} + (\lambda + \mu)\frac{\partial^2 U_1}{\partial x\partial y} + \mu\frac{\partial^2 U_2}{\partial x^2} = 0 \quad (4.54)$$

$$\begin{aligned} & B_{1111}\frac{\partial^2 U_1}{\partial x^2} + B_{1112}\frac{\partial^2 U_1}{\partial y\partial x} + B_{2111}\frac{\partial^2 U_1}{\partial x\partial y} + B_{2112}\frac{\partial^2 U_1}{\partial y^2} + \\ & B_{1121}\frac{\partial^2 U_2}{\partial x^2} + B_{1122}\frac{\partial^2 U_2}{\partial y\partial x} + B_{2121}\frac{\partial^2 U_2}{\partial x\partial y} + B_{2122}\frac{\partial^2 U_2}{\partial y^2} \\ & = \left(1 - \frac{\partial U_1}{\partial x} - \frac{\partial U_2}{\partial y}\right)\rho\ddot{U}_1 \end{aligned} \quad (4.55)$$

$$\begin{aligned} & B_{1211}\frac{\partial^2 U_1}{\partial x^2} + B_{1212}\frac{\partial^2 U_1}{\partial y\partial x} + B_{2211}\frac{\partial^2 U_1}{\partial x\partial y} + B_{2212}\frac{\partial^2 U_1}{\partial y^2} + \\ & B_{1221}\frac{\partial^2 U_2}{\partial x^2} + B_{1222}\frac{\partial^2 U_2}{\partial y\partial x} + B_{2221}\frac{\partial^2 U_2}{\partial x\partial y} + B_{2222}\frac{\partial^2 U_2}{\partial y^2} \\ & = \left(1 - \frac{\partial U_1}{\partial x} - \frac{\partial U_2}{\partial y}\right)\rho\ddot{U}_2 \end{aligned} \quad (4.56)$$

4.5. Summary

A modified wave propagation model was developed using Eqs. (4.53)-(4.56), whose primary variables are displacements \underline{U}_1 , \underline{U}_2 , U_1 , and U_2 . \underline{U}_1 and \underline{U}_2 are the displacements of the deformed state along the X and Y directions, respectively. They can be acquired by solving Eqs. (4.53) and (4.54) subject to boundary conditions described in Chapter V. \underline{U}_1 and \underline{U}_2 are not functions of time since they are solutions corresponding to steady-states. Displacement U_1 is the displacement of the final state along the X-direction and U_2 is the displacement of the final state along the Y-direction. U_1 and U_2 are functions of time that can be solved by Eqs. (4.55) and (4.56) subject to initial and boundary conditions described in Chapter V. Since close-form solutions to these governing equations are difficult to find, numerical solutions will instead be attempted. In the next chapter, a finite element model using the governing equations (4.53) to (4.56) will be developed.

CHAPTER V

FEMLAB BASED FINITE ELEMENT PLATE WAVE MODEL

To the theoretical formulation derived in Chapter IV, a FEMLAB based numerical model is developed. FEMLAB, a commercially available finite element method (FEM) software package, is introduced first. The configuration of the developed FEMLAB model, boundary conditions and material properties are then defined. The forcing functions used to initiate stress waves in the model are also discussed.

5.1. Introduction to FEMLAB

FEMLAB is a FEM software package under the registered trademark of COMSOL AB. It provides a powerful interactive environment for modeling and solving scientific and engineering problems governed by partial differential equations (PDEs). FEMLAB solves PDEs using the proven FEM and it also provides ‘canned’ models for multi-physics problems. FEMLAB models are constructed by defining the relevant physical quantities such as material properties, loads constraints, sources, and fluxes. FEMLAB can handle a wide range of problems including acoustics, electromagnetics, MEMS and quantum mechanics using either built-in models or user-defined PDE models. For user-defined models, the corresponding governing equations need be expressed in a standard FEMLAB form. Using FEMLAB’s hassle-free UGI, specifying and modifying model PDEs are relatively effortless.

5.2. Model Description

The numerical model to be developed in the following is for simulating a finite plate in an aircraft wing structure. The plate is considered as flat and subject to an applied pressure and temperature as shown in Fig. 5.1. The width of the plate is assumed to be infinitely long compared with the length and thickness, thus satisfying the plane-strain condition. As such, the 3D model is then simplified to a 2D one. Material properties,

model configuration, boundary conditions, mesh types and mesh sizes need be specified. As described in Chapter IV that U_1 and U_2 are functions of time but \underline{U}_1 and \underline{U}_2 are not, Eqs. (4.54) and (4.55) are valid for static analysis while Eqs. (4.56) and (4.57) are required for transient analysis. Since FEMLAB provides multi-physics capability allowing two or more different types of physical formulations to be considered simultaneously, static and transient models are constructed in FEMLAB. The two models have identical configurations, material properties, and mesh elements except for different boundary conditions. The 2-D geometric definition of the FEMLAB numerical model is given in Fig. 5.2. Points A and B are the excitation points and Points 1 and 2 are the wave acquisition points. The origin is at the middle of the plate. The model is of 150 mm in length (L) and propagation paths L_1 and L_2 are 35mm and 45mm, respectively. There is a pressure (P) acting vertically on segment BD. Temperature is assumed to be uniform across the plate. Pressure (P), temperature (T) and plate width (d) are variables to be analyzed. The initial temperature is assumed to be 25°C. By varying the variables, responses of plate in the form of propagating plate waves can be investigated. Three different plate thicknesses (2mm, 1.5mm and 1mm), four different temperatures (25°C, 50°C, 100°C, and 300°C) and three different uniform pressures (1×10^6 N/m, 5×10^6 N/m, and 1×10^7 N/m) are considered. The material for the plate is aluminum alloy 6061-T6, whose properties are tabulated in Table 5.1.

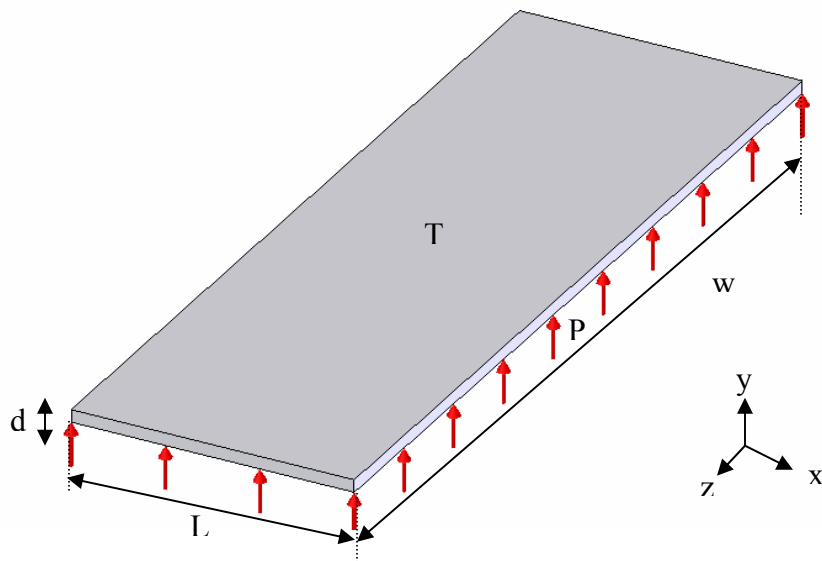


Fig. 5.1. Simplified plate model

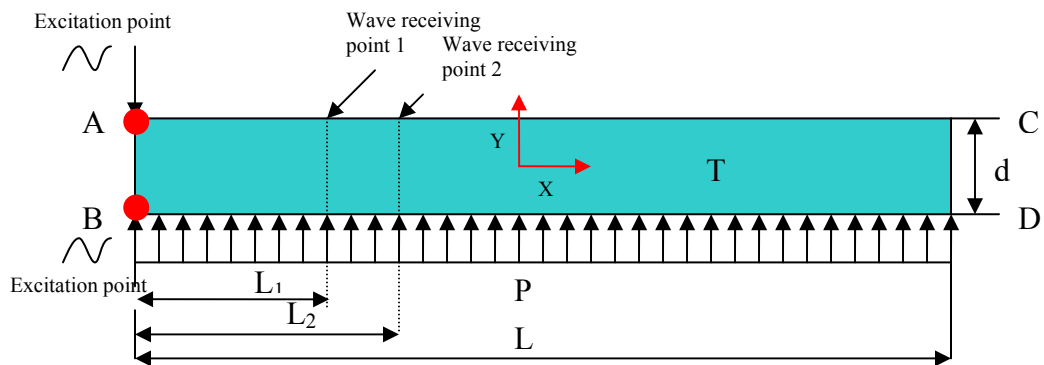


Fig. 5.2. 2-D numerical plate model with forcing conditions

Table 5.1. Material properties of aluminum alloy 6061-T6

	Metric	English
Density (ρ)	2700 kg/m ³	0.0975 lb/in ³
Tensile Strength, Ultimate	310 MPa	45000 psi
Tensile Strength, Yield	275 MPa	39900 psi
Modulus of Elasticity (E)	69 GPa	10000 ksi
Poisson's Ratio (ν)	0.33	0.33
Ultimate Bearing Strength	607 MPa	88000 psi
Bearing Yield Strength	386 MPa	56000 psi
Fatigue Strength	95 MPa	13800 psi
Shear Modulus (G)	26 GPa	3770 ksi
CTE, linear 20°C (α)	23.6 $\mu\text{m/m-}^\circ\text{C}$	13.1 $\mu\text{in/in-}^\circ\text{F}$
CTE, linear 250°C (α)	25.2 $\mu\text{m/m-}^\circ\text{C}$	14 $\mu\text{in/in-}^\circ\text{F}$
Heat Capacitance	0.896 J/g- $^\circ\text{C}$	0.214 BTU/lb- $^\circ\text{F}$
Thermal Conductivity	166.9 W/m-K	1160 BTU/lb- $^\circ\text{F}$
Melting Point	582-652 $^\circ\text{C}$	1080-1210 $^\circ\text{F}$
Lam'e constant ($\lambda = \frac{Ev}{(1+\nu) + (1-2\nu)}$)	50.354 GPa	7301.33 ksi
Lam'e constant ($\mu=G$)	26 GPa	3770 ksi

5.2.1. Boundary conditions

Since different boundary conditions could lead to different responses, boundary conditions imitating that of a wing structure (Fig. 5.3) are carefully selected for the model. Segment AB is constrained as immovable along the X-direction while free to move along the Y-direction. Stress-free segment AC is allowed to move in any direction. Points C and D are constrained as immovable in the Y-direction but allowed to translate along X-direction. Segment BD is subject to uniform pressure P and is free to move in any direction. The boundary conditions specified for the transient model are shown in Fig. 5.4. The forcing functions for exciting stress waves exert at points A and B. Stress-free segment AB is constrained along the X-direction but not the Y-direction. Points C and D are constrained along the Y-direction but free to move along the X-direction. Segment BD is movable in any direction.

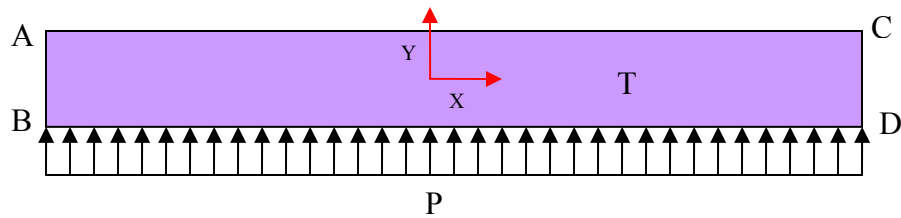


Fig. 5.3. Boundary conditions for static model

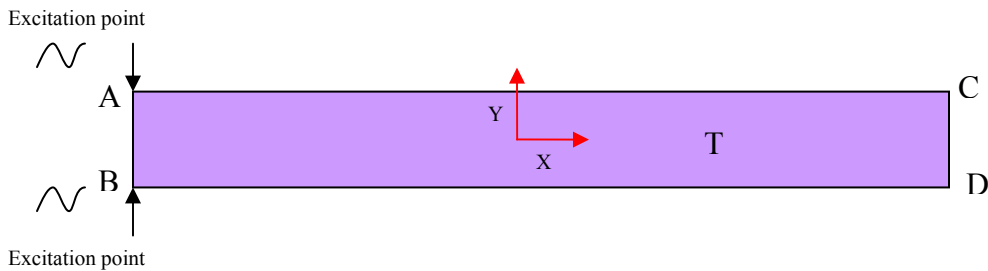


Fig. 5.4. Boundary conditions for transient model

5.2.2. Mesh type and mesh size

Triangular meshes shown in Fig. 5.5 are used in the numerical model. Mesh density needs to be high enough to ensure numerical accuracy. Mesh sizes are estimated by the following formula,

$$C = f\lambda \quad (5.1)$$

where C is wave velocity, f is wave frequency, and λ is wavelength. According to the Nyquist sampling Theorem, sampling frequency is at least two times the wave frequency. As such, the maximum mesh size needs to be half of the wavelength. It is difficult to determine wave velocity and frequency accurately *a priori*. An approximate mesh size can be computed depending on the estimated wave velocity and frequency. In the model, the range of frequency is from 0 to 1MHz, and the wave velocity is slower than the shear wave velocity which is 3,103m/s. Therefore, the approximate wavelength is 0.0031m

and the approximate mesh sizes are (0.00155m)x(0.00155m). Reduction in mesh size is oftentimes required to ensure converged numerical solutions.

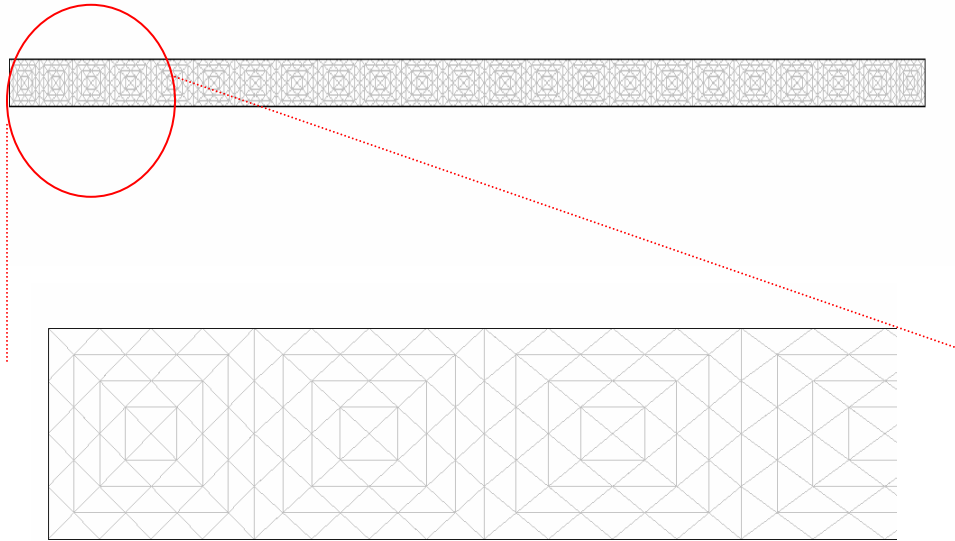


Fig. 5.5. Triangular meshes in model

5.3. Forcing Functions for Excitation

Fig. 5.6 shows the temporal profile of the impulse forcing function that is exerted at points A and B (see Fig. 5.2). The function is defined using a Gaussian function

$$G(t) = \frac{1}{\sqrt{2\pi a}} e^{\frac{-t^2}{2a^2}} \quad (5.2)$$

where a dictates the width of $G(t)$ in both the time and frequency domains. The forcing function is specified as an initial condition in FEMLAB. Different orientation of excitation would result in different modes. If excitation exertions at points A and B are of the same orientation, anti-symmetric modes would result. Otherwise, if excitations at

points A and B are of the opposite orientation, symmetric modes would propagate. In this research, only anti-symmetric modes are investigated.

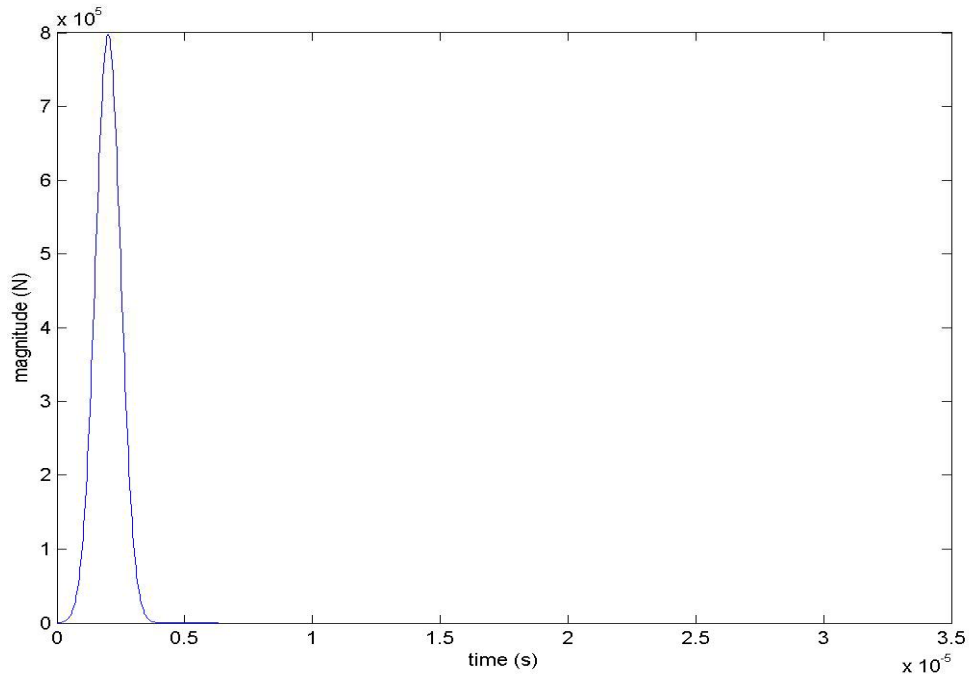


Fig. 5.6. Gaussian forcing function

5.4. Summary

A numerical model has been constructed in FEMLAB. Numerical solutions can be obtained by solving the governing equations developed in Chapter IV subject to boundary and initial conditions. Resulted numerical solutions are propagating Lamb waves in the plate model. The waves are acquired at two different locations that are 10mm apart. To investigate the behavior of ultrasonic plate waves in response to the influences of temperature, pressure and thickness, 36 different combinations of parameters are considered for numerical study using the FEMLAB model. Table 5.2 provides details of these combinations.

Table 5.2. Different combinations of parameters

Excitation type	Thickness (mm)	Temperature (°C)	Pressure (N/m ²)
Anti-symmetric	2	25	1×10^6
Anti-symmetric	2	50	1×10^6
Anti-symmetric	2	100	1×10^6
Anti-symmetric	2	300	1×10^6
Anti-symmetric	2	25	5×10^6
Anti-symmetric	2	50	5×10^6
Anti-symmetric	2	100	5×10^6
Anti-symmetric	2	300	5×10^6
Anti-symmetric	2	25	1×10^7
Anti-symmetric	2	50	1×10^7
Anti-symmetric	2	100	1×10^7
Anti-symmetric	2	300	1×10^7
Anti-symmetric	1.5	25	1×10^6
Anti-symmetric	1.5	50	1×10^6
Anti-symmetric	1.5	100	1×10^6
Anti-symmetric	1.5	300	1×10^6
Anti-symmetric	1.5	25	5×10^6
Anti-symmetric	1.5	50	5×10^6
Anti-symmetric	1.5	100	5×10^6
Anti-symmetric	1.5	300	5×10^6
Anti-symmetric	1.5	25	1×10^7
Anti-symmetric	1.5	50	1×10^7
Anti-symmetric	1.5	100	1×10^7
Anti-symmetric	1.5	300	1×10^7
Anti-symmetric	1	25	1×10^6

Excitation type	Thickness (mm)	Temperature (°C)	Pressure (N/m ²)
Anti-symmetric	1	50	1×10^6
Anti-symmetric	1	100	1×10^6
Anti-symmetric	1	300	1×10^6
Anti-symmetric	1	25	5×10^6
Anti-symmetric	1	50	5×10^6
Anti-symmetric	1	100	5×10^6
Anti-symmetric	1	300	5×10^6
Anti-symmetric	1	25	1×10^7
Anti-symmetric	1	50	1×10^7
Anti-symmetric	1	100	1×10^7
Anti-symmetric	1	300	1×10^7

CHAPTER VI

RESULTS OF NUMERICAL INVESTIGATION

Using the FEMLAB model developed in Chapter V, numerical waveforms are obtained in response to various combinations of parameters and forcing configurations. The numerical waveforms corresponding to different pressures are discussed first in the chapter, followed by waveforms subject to varying temperatures and plate thicknesses. The extraction of dispersion information is then discussed in detailed along with the display of dispersion curves as functions of pressure, temperature and plate thickness.

6.1. Waveforms as Functions of Pressure

As stated, three different pressures; namely, 1×10^6 N/m, 5×10^6 N/m and 1×10^7 N/m, are considered along with four different temperatures, 25°C, 50°C, 100°C and 300°C and three different thicknesses, 1mm, 1.5mm, and 2mm. To illustrate the effects of pressure, waveforms correspond to different pressures at a specific thickness and temperature are presented. Figs. 6.1-6.4 present the waveforms for three different pressures corresponding to thickness $d=1$ mm and temperatures $T=25^\circ\text{C}$, 50°C , 100°C and 300°C , respectively. Waveforms found in Figs. 6.5-6.8 correspond to the same three different pressures and temperatures at $d=1.5$ mm. Waveforms correspond to $d=2$ mm at the same 3 pressures and temperatures are shown in Figs. 6.9-6.12. All waveforms are acquired at Position 1 seen in Fig. 5.2 at time $t=2.5 \times 10^{-5}$ seconds.

Differences in waveforms as seen in Figs. 6.1-6.12 are minor, thus suggesting that pressure is not as dominant as temperature and thickness on affecting plate wave propagation.

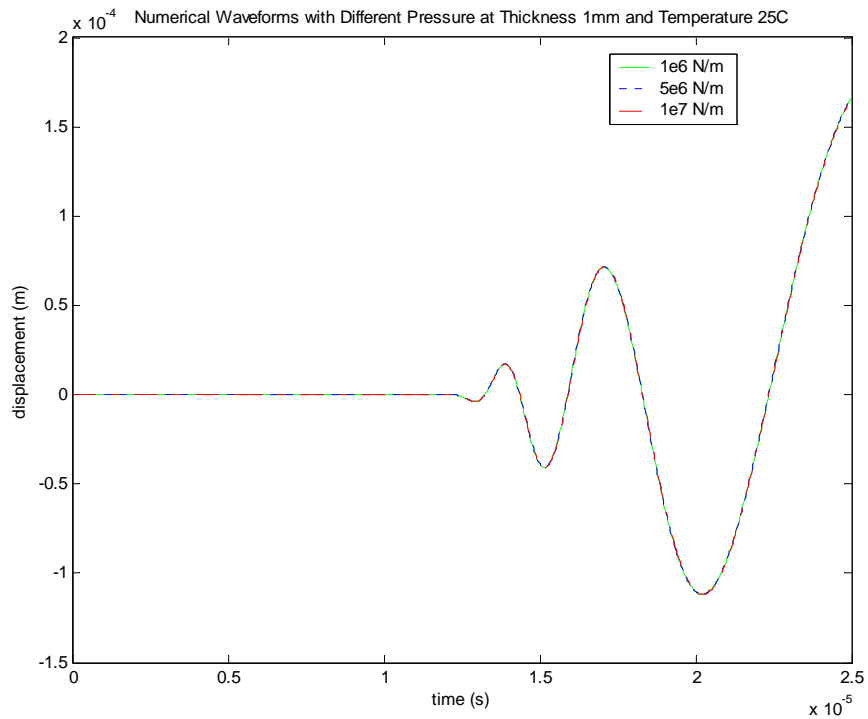


Fig. 6.1. Waveforms of three different pressures at $d=1\text{mm}$ and $T=25^\circ\text{C}$

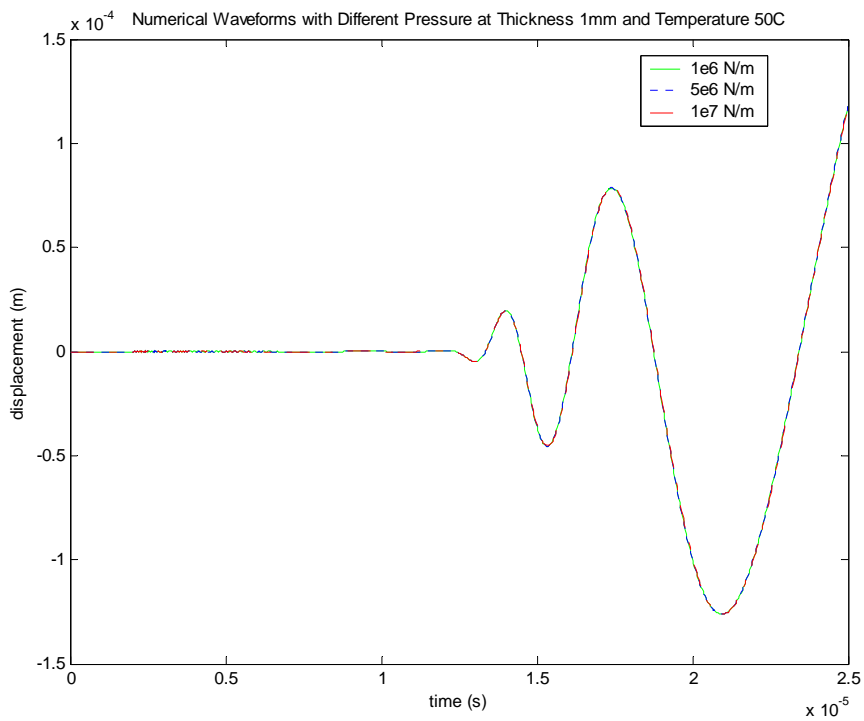


Fig. 6.2. Waveforms of three different pressures at $d=1\text{mm}$ and $T=50^\circ\text{C}$

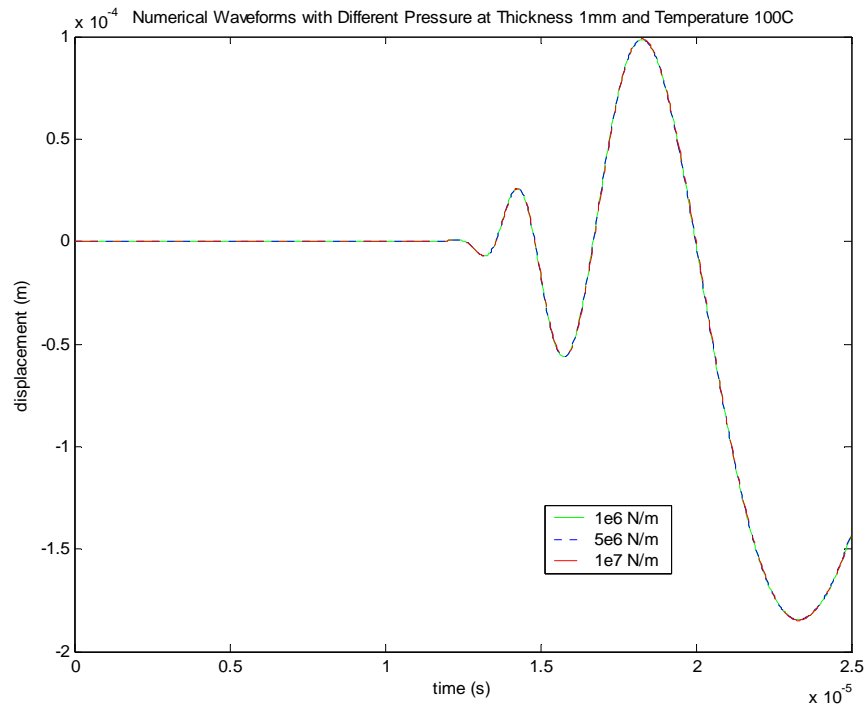


Fig. 6.3. Waveforms of three different pressures at $d=1\text{mm}$ and $T=100^\circ\text{C}$

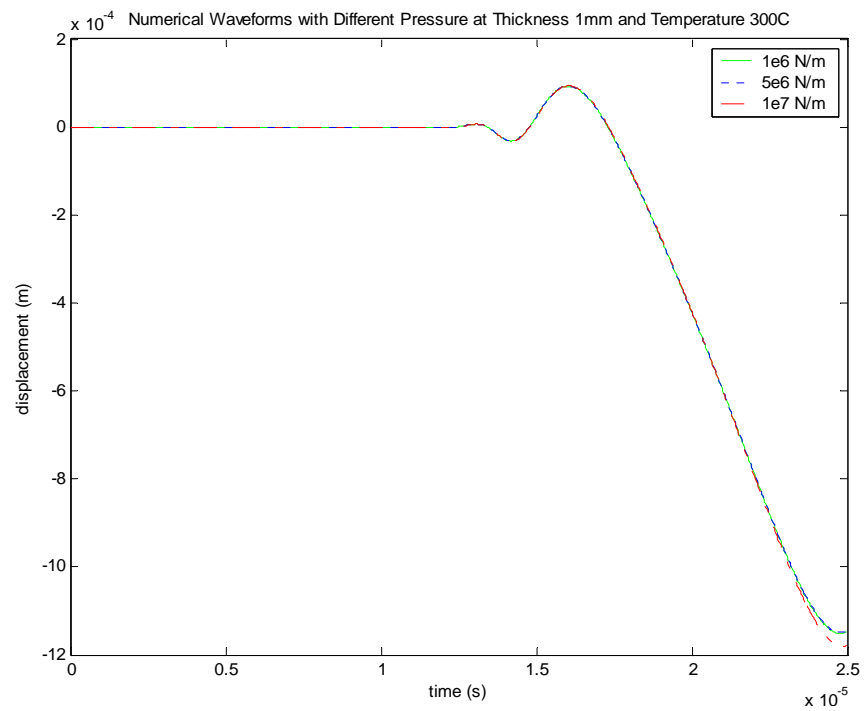


Fig. 6.4. Waveforms of three different pressures at $d=1\text{mm}$ and $T=300^\circ\text{C}$

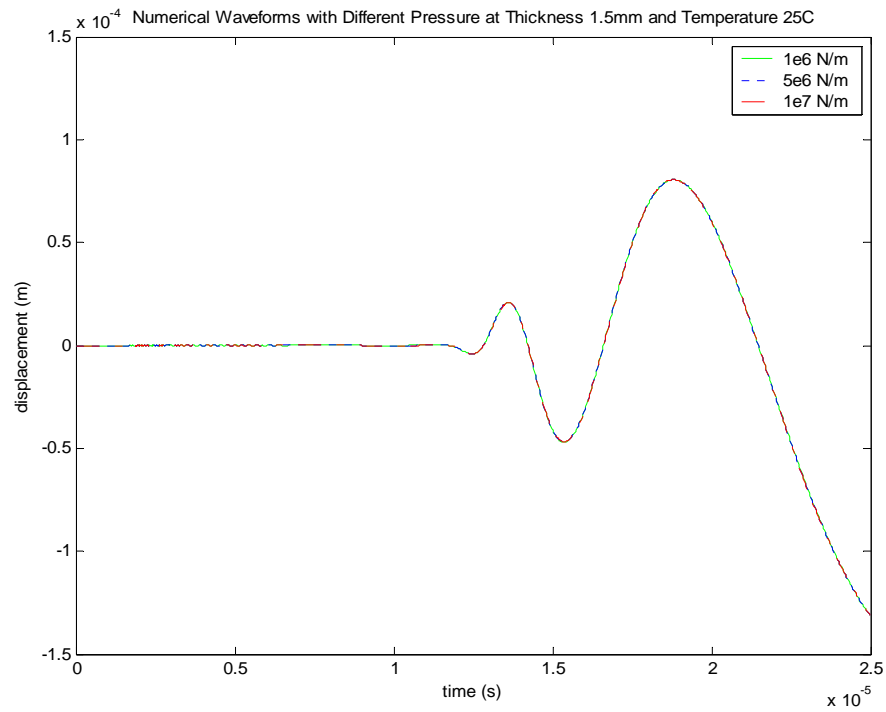


Fig. 6.5. Waveforms of three different pressures at $d=1.5\text{mm}$ and $T=25^\circ\text{C}$

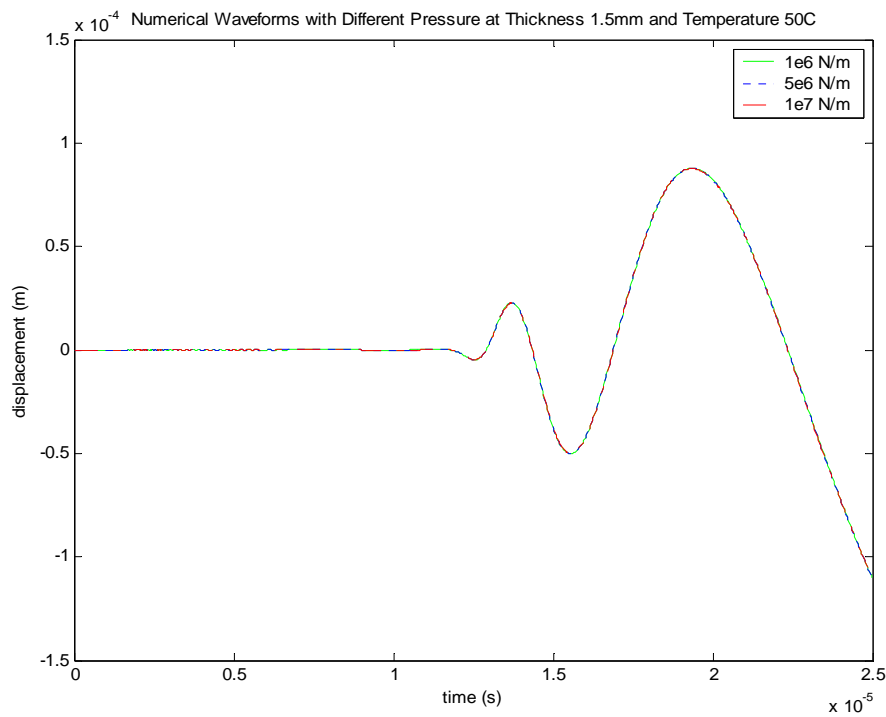


Fig. 6.6. Waveforms of three different pressures at $d=1.5\text{mm}$ and $T=50^\circ\text{C}$

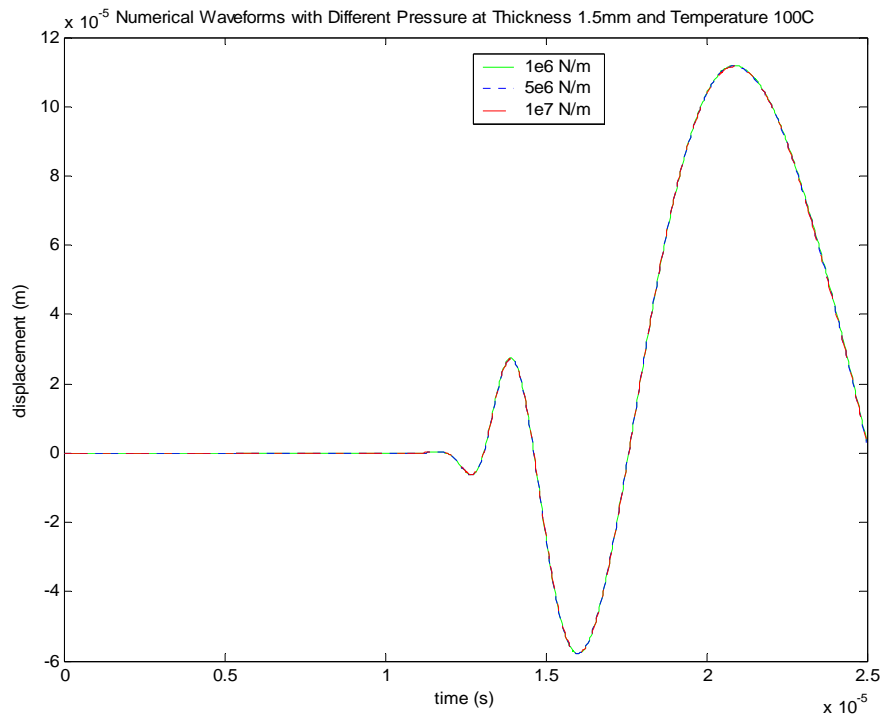


Fig. 6.7. Waveforms of three different pressures at $d=1.5\text{mm}$ and $T=100^\circ\text{C}$

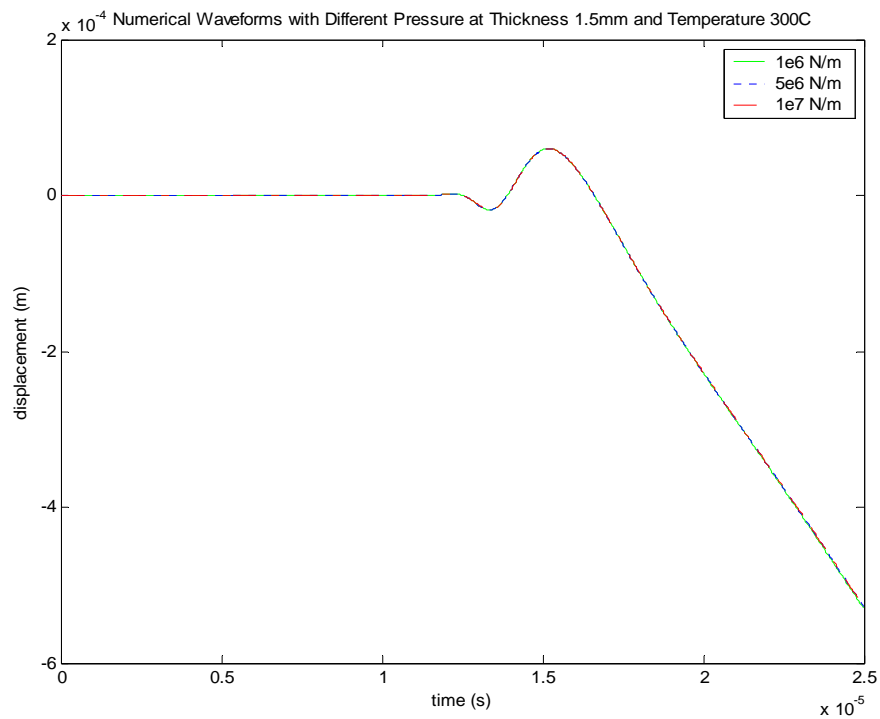


Fig. 6.8. Waveforms of three different pressures at $d=1.5\text{mm}$ and $T=300^\circ\text{C}$

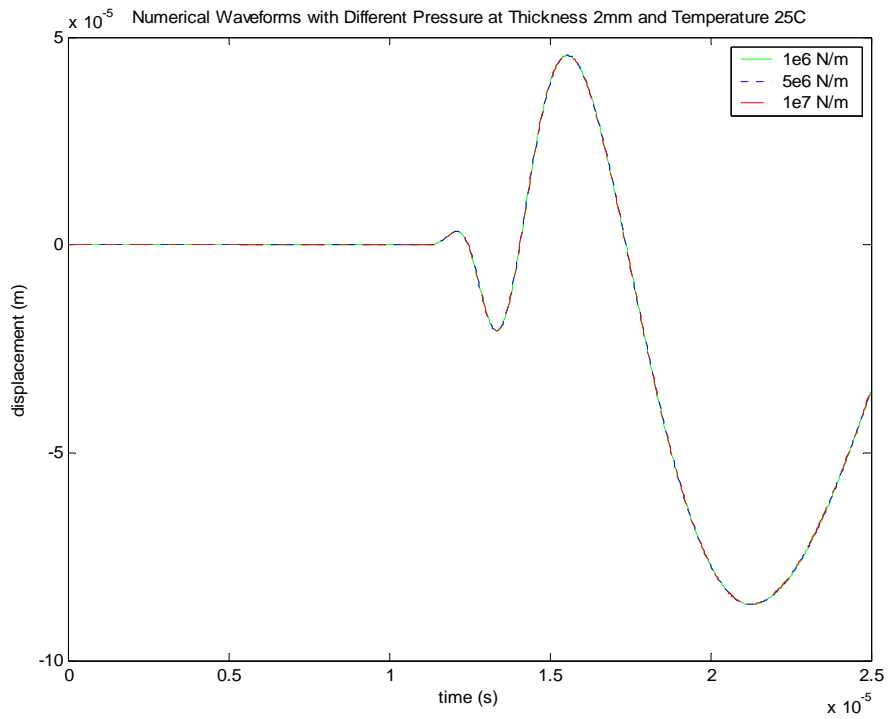


Fig. 6.9. Waveforms of three different pressures at $d=2.0\text{mm}$ and $T=25^\circ\text{C}$

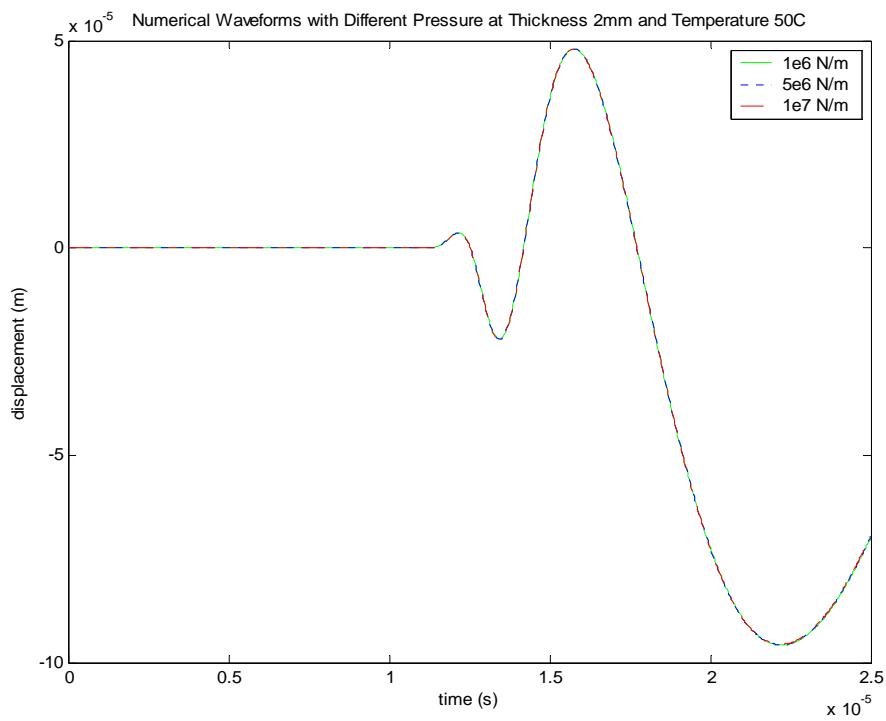


Fig. 6.10. Waveforms of three different pressures at $d=2.0\text{mm}$ and $T=50^\circ\text{C}$

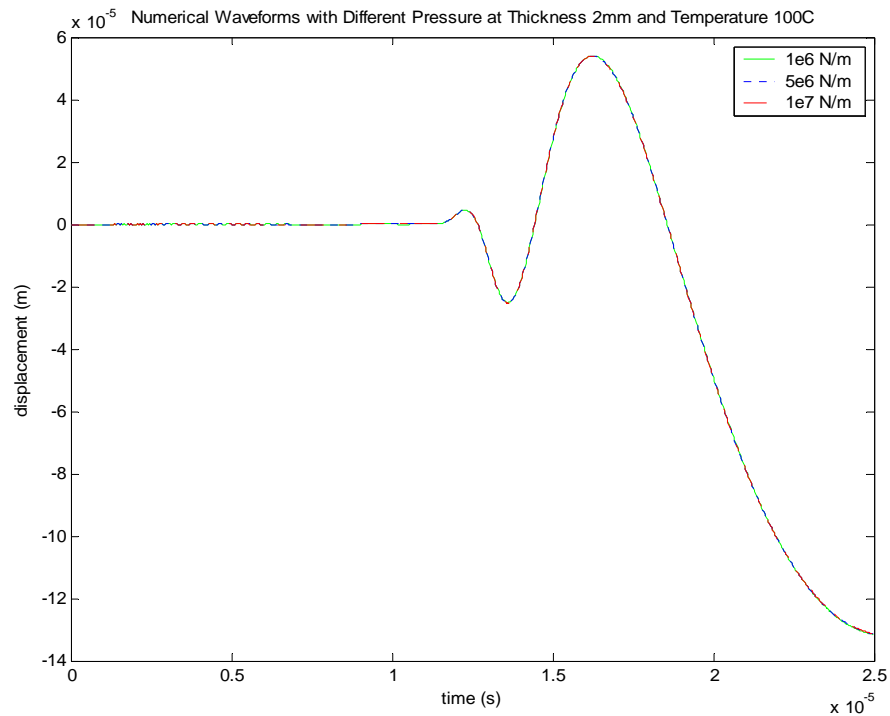


Fig. 6.11. Waveforms of three different pressures at $d=2.0\text{mm}$ and $T=100^\circ\text{C}$

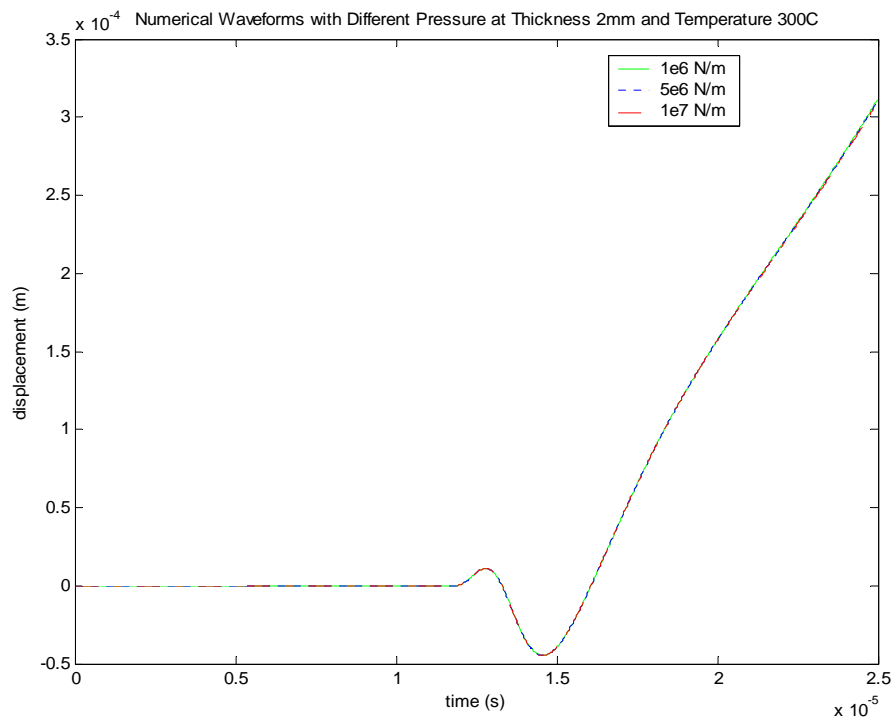


Fig. 6.12. Waveforms of three different pressures at $d=2.0\text{mm}$ and $T=300^\circ\text{C}$

6.2. Waveforms as Functions of Temperature

Numerical waveforms correspond to four different temperatures at a specific pressure and plate thickness are presented in the section. Figs. 6.13-6.15 present the waveforms for the four different temperatures corresponding to thickness $d=1\text{mm}$ and pressure $P=1 \times 10^6 \text{ N/m}$, $5 \times 10^6 \text{ N/m}$ and $1 \times 10^7 \text{ N/m}$, respectively. Waveforms found in Figs. 6.16-6.18 correspond to the same different temperatures and pressure at $d=1.5\text{mm}$. Waveforms correspond to $d=2\text{mm}$ at the same temperatures and pressures are shown in Figs. 6.19-6.21. All waveforms are acquired at Position 1 at time $t=2.5 \times 10^{-5}$ seconds.

It can be seen from Figs. 6.13-6.21 that differences in waveforms are prominent. Wave dispersion is sensitive to increasing temperature. The waveforms at different temperatures also vary with plate thickness, thus indicating that temperature effect is significant regardless of pressure and thickness conditions.

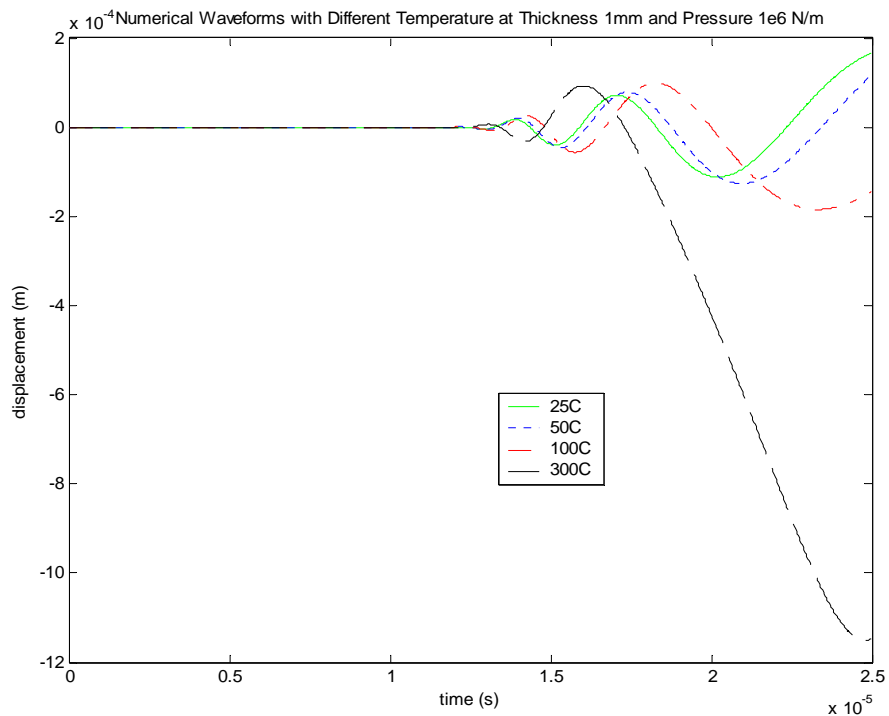


Fig. 6.13. Waveforms of four different temperatures at $d=1.0\text{mm}$ and $P=1 \times 10^6 \text{ N/m}$

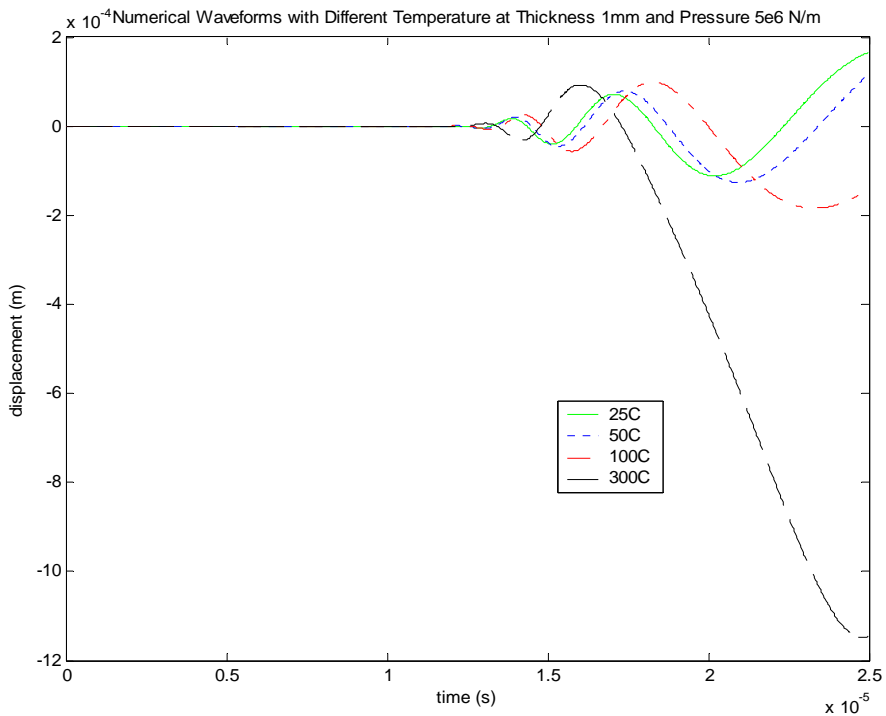


Fig. 6.14. Waveforms of four different temperatures at $d=1.0\text{mm}$ and $P=5 \times 10^6$ N/m

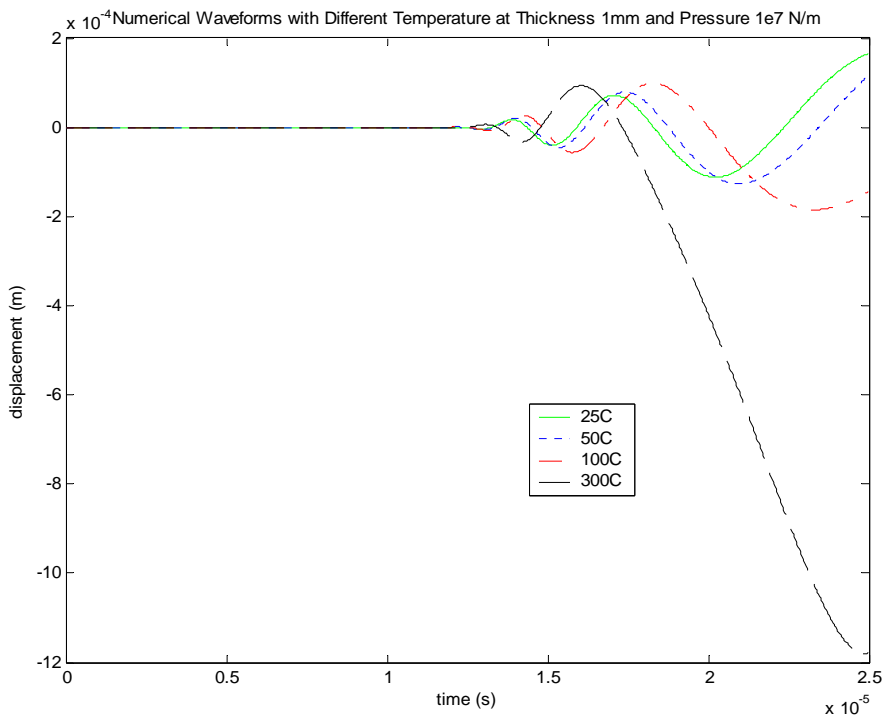


Fig. 6.15. Waveforms of four different temperatures at $d=1.0\text{mm}$ and $P=1 \times 10^7$ N/m

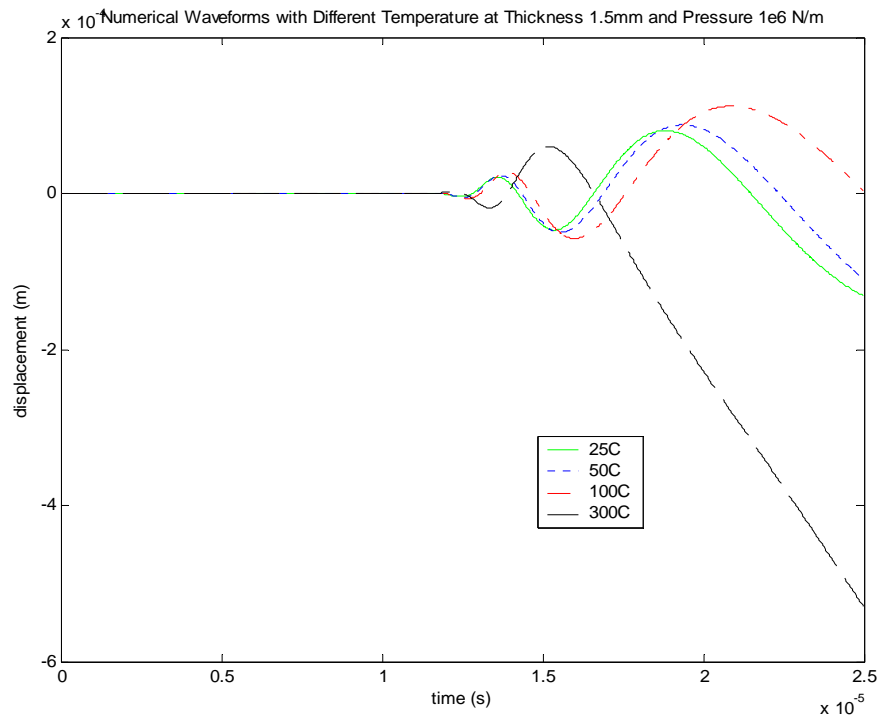


Fig. 6.16. Waveforms of four different temperatures at $d=1.5\text{mm}$ and $P=1 \times 10^6$ N/m

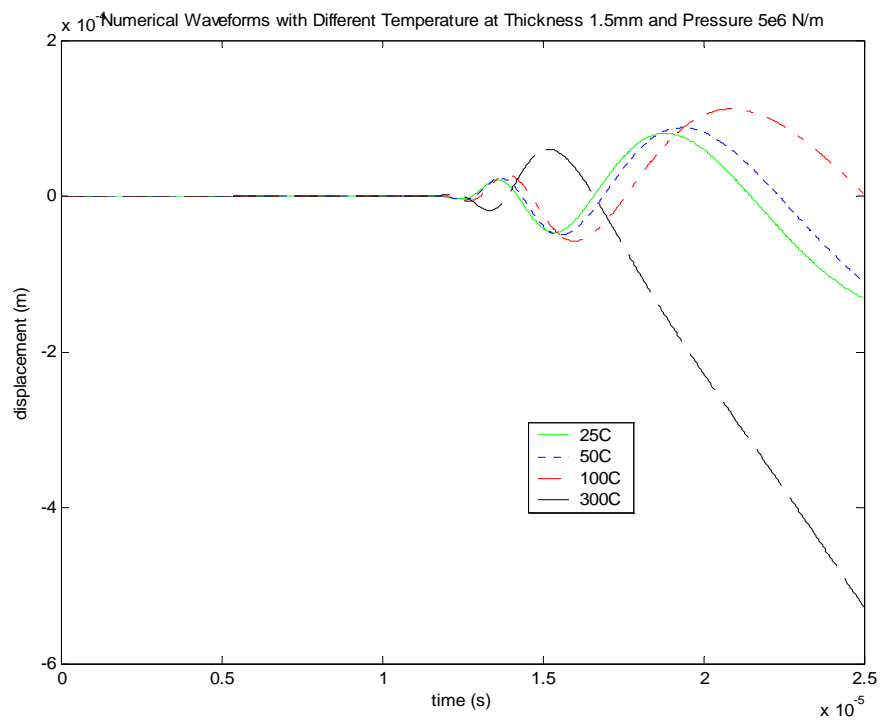


Fig. 6.17. Waveforms of four different temperatures at $d=1.5\text{mm}$ and $P=5 \times 10^6$ N/m

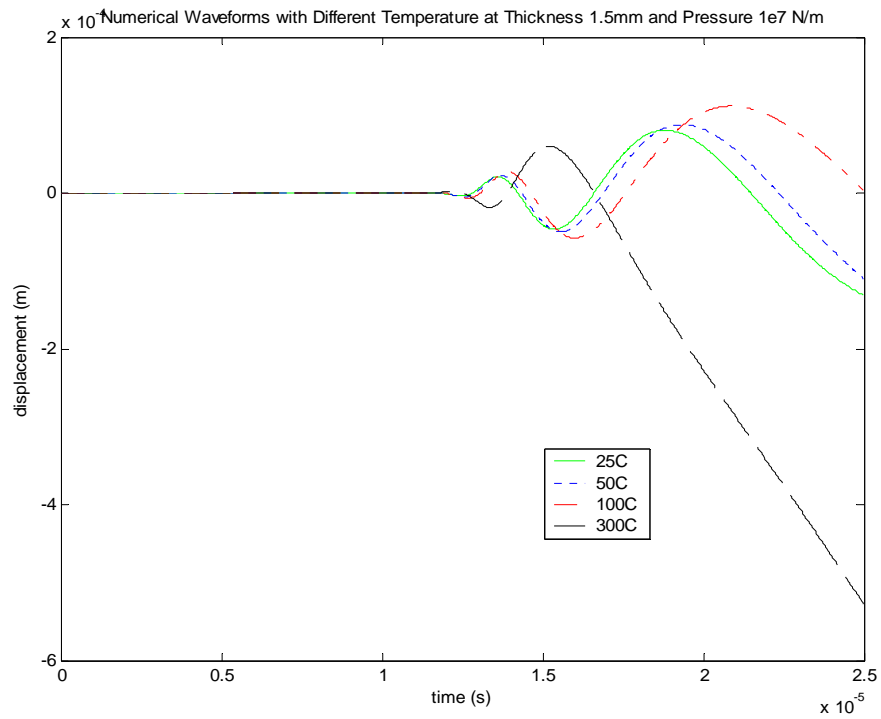


Fig. 6.18. Waveforms of four different temperatures at $d=1.5\text{mm}$ and $P=1 \times 10^7$ N/m

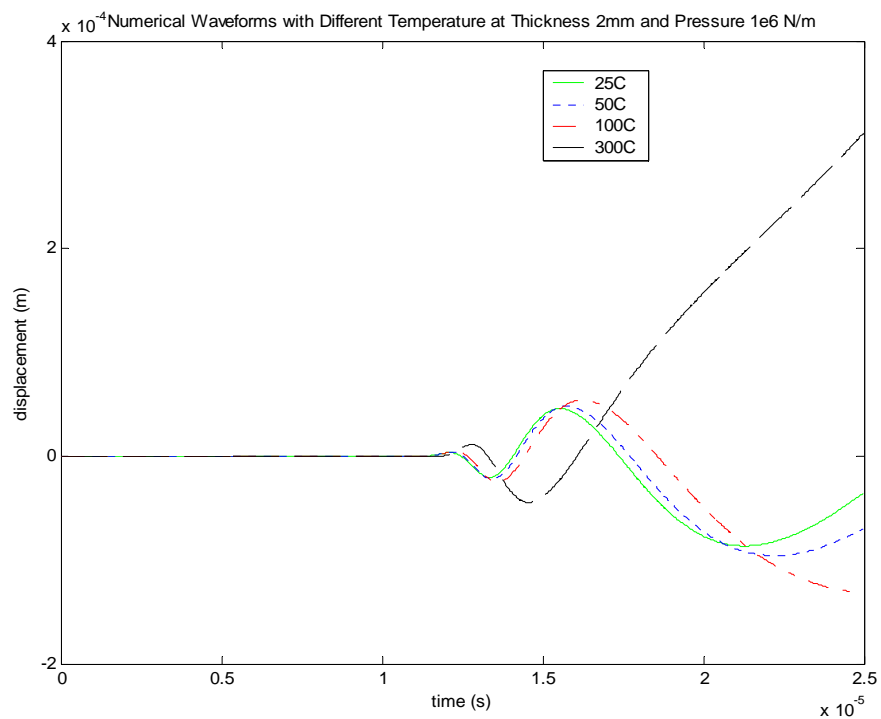


Fig. 6.19. Waveforms of four different temperatures at $d=2.0\text{mm}$ and $P=1 \times 10^6$ N/m

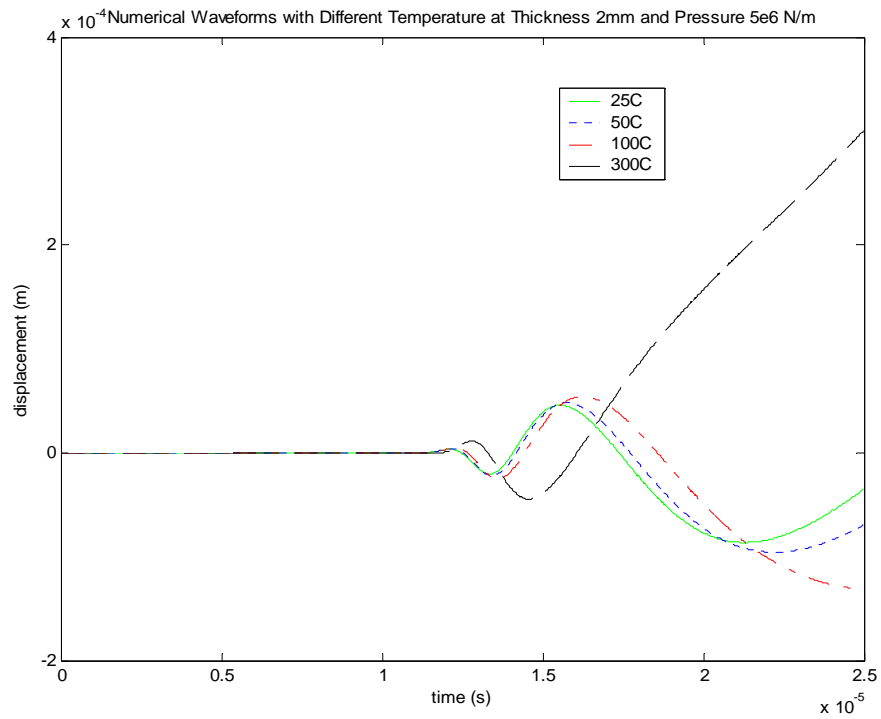


Fig. 6.20. Waveforms of four different temperatures at $d=2.0\text{mm}$ and $P=5 \times 10^6$ N/m

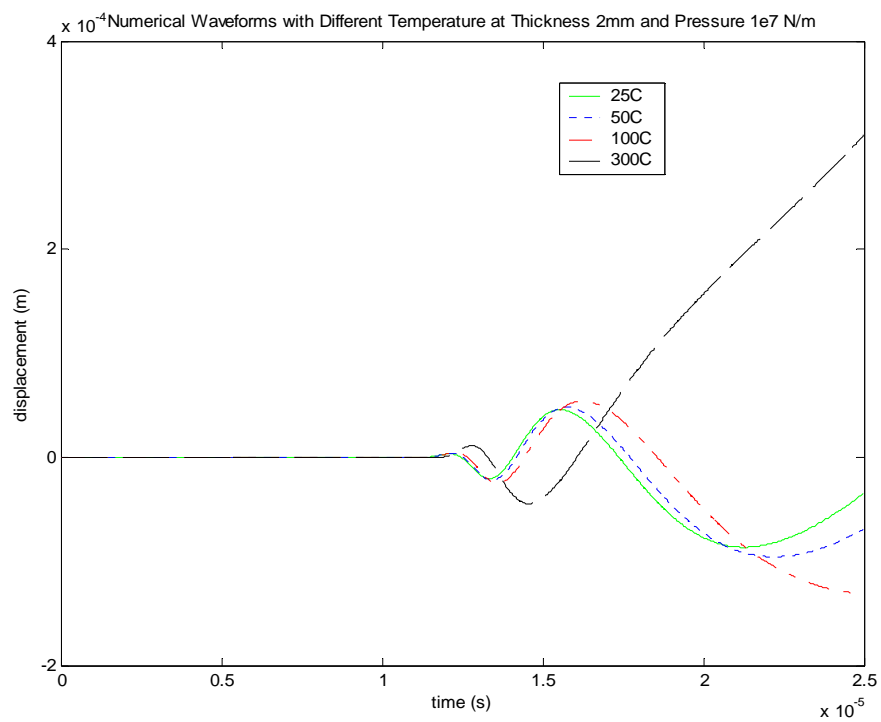


Fig. 6.21. Waveforms of four different temperatures at $d=2.0\text{mm}$ and $P=1 \times 10^7$ N/m

6.3. Waveforms as Functions of Plate Thickness

Numerical waveforms correspond to three different thicknesses at a specific pressure and temperature are considered in the section. Figs. 6.22-6.24 present the waveforms for the three different thicknesses corresponding to temperature $T=25^{\circ}\text{C}$ and pressure $P=1 \times 10^6 \text{ N/m}^2$, $5 \times 10^6 \text{ N/m}^2$ and $1 \times 10^7 \text{ N/m}^2$, respectively. Waveforms shown in Figs. 6.25-6.27 correspond to the same three different thicknesses and pressures at $T=50^{\circ}\text{C}$. Waveforms correspond to $T=100^{\circ}\text{C}$ at the same three thicknesses and three pressures are found in Figs. 6.28-6.30. Lastly, Figs. 6.31-6.33 show the waveforms in response to the same thicknesses and pressures at $T=300^{\circ}\text{C}$. Again, all waveforms are acquired at Position 1 at time $t=2.5 \times 10^{-5}$ seconds.

It can be seen from Figs. 6.22-6.33 that plate thickness is more dominant than temperature and pressure in affecting waveform. The waveforms at different thicknesses also vary with temperature, thus indicating that effects of plate thickness is significant regardless of pressure and temperature conditions.

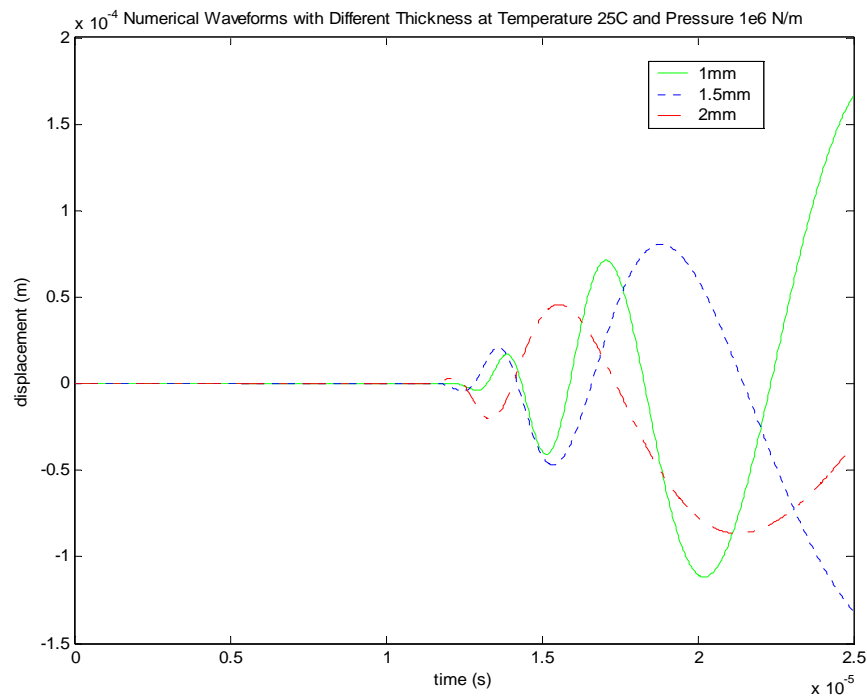


Fig. 6.22. Waveforms of three different thicknesses at $T=25^{\circ}\text{C}$ and $P=1 \times 10^6 \text{ N/m}^2$

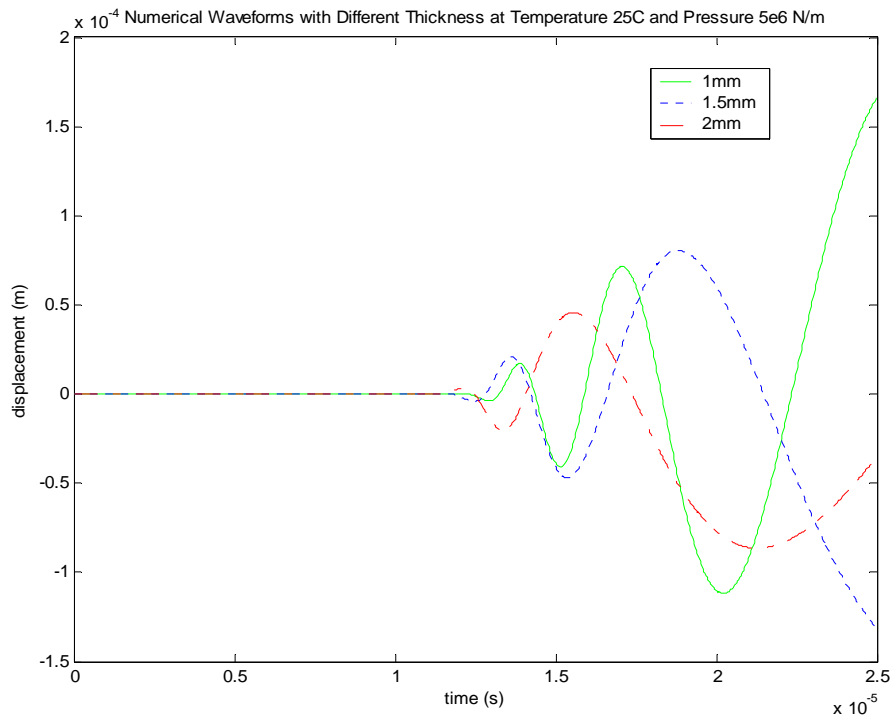


Fig. 6.23. Waveforms of three different thicknesses at $T=25^{\circ}\text{C}$ and $P=5 \times 10^6$ N/m

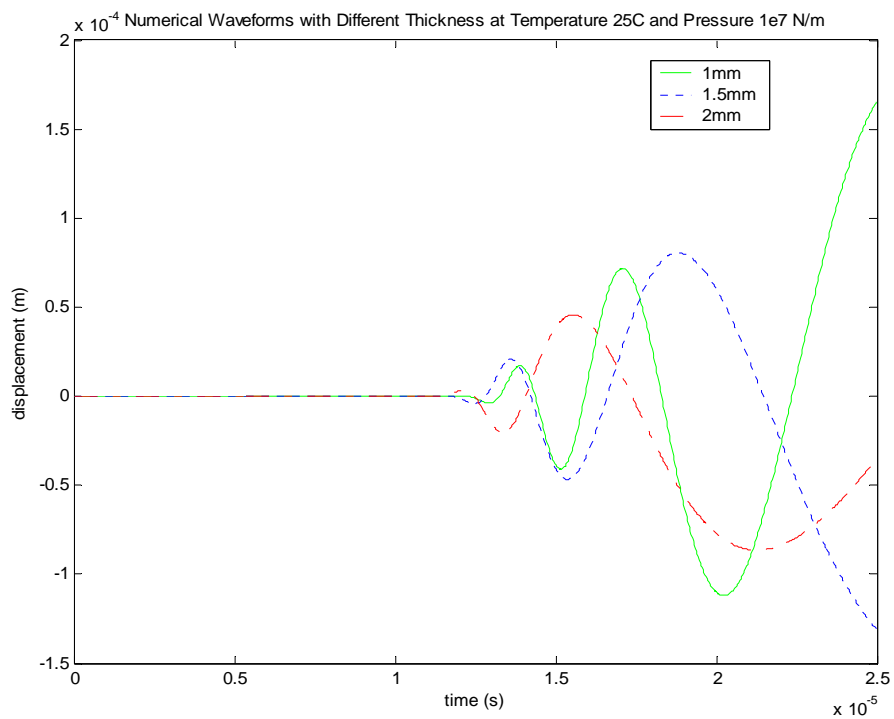


Fig. 6.24. Waveforms of three different thicknesses at $T=25^{\circ}\text{C}$ and $P=1 \times 10^7$ N/m

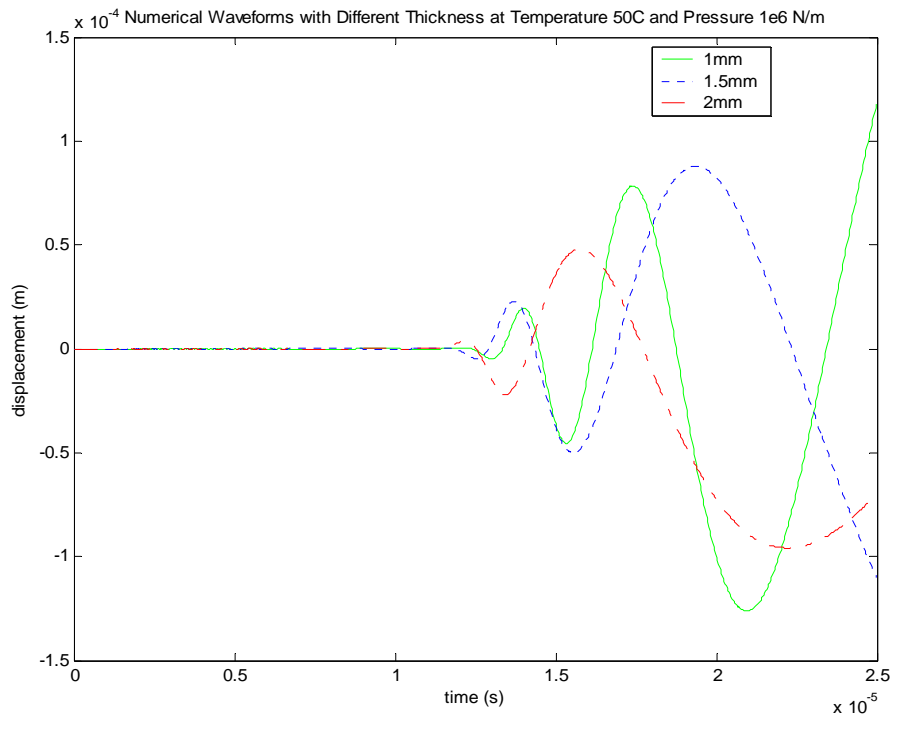


Fig. 6.25. Waveforms of three different thicknesses at $T=50^{\circ}\text{C}$ and $P=1 \times 10^6$ N/m

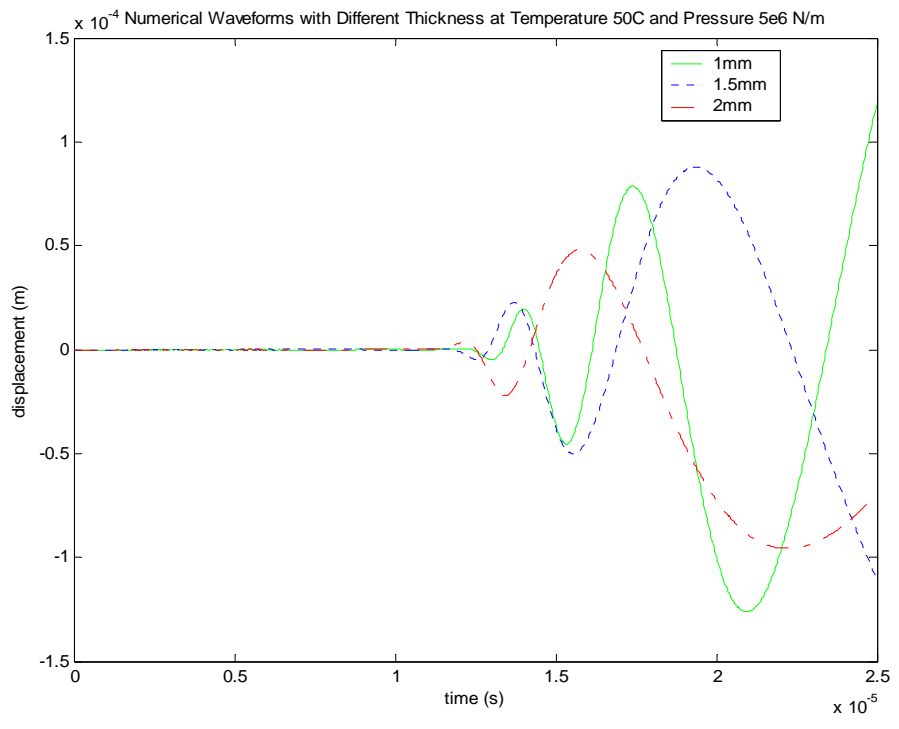


Fig. 6.26. Waveforms of three different thicknesses at $T=50^{\circ}\text{C}$ and $P=5 \times 10^6$ N/m

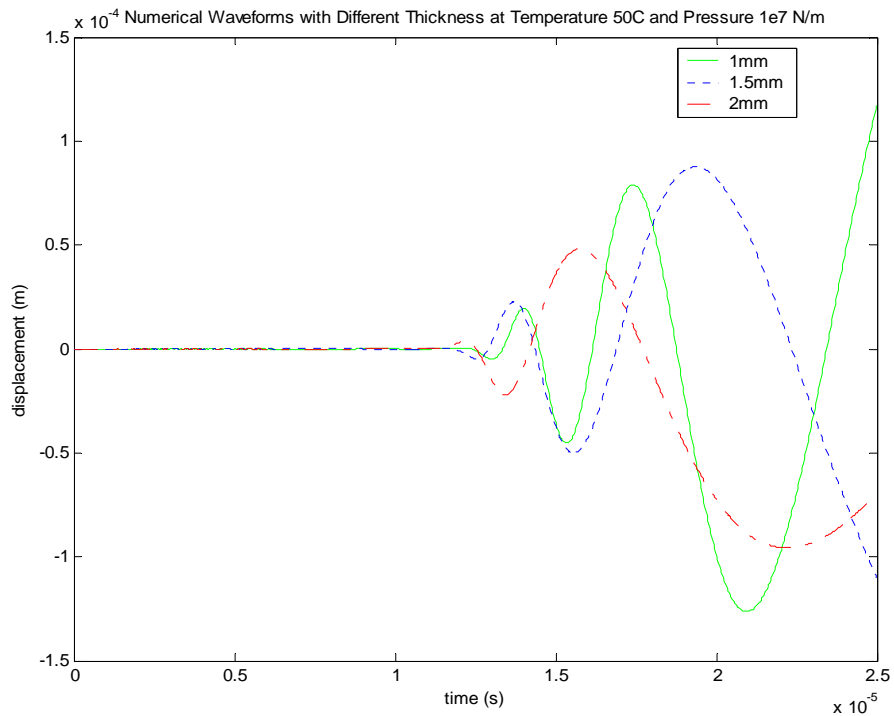


Fig. 6.27. Waveforms of three different thicknesses at $T=50^{\circ}\text{C}$ and $P=1 \times 10^7$ N/m

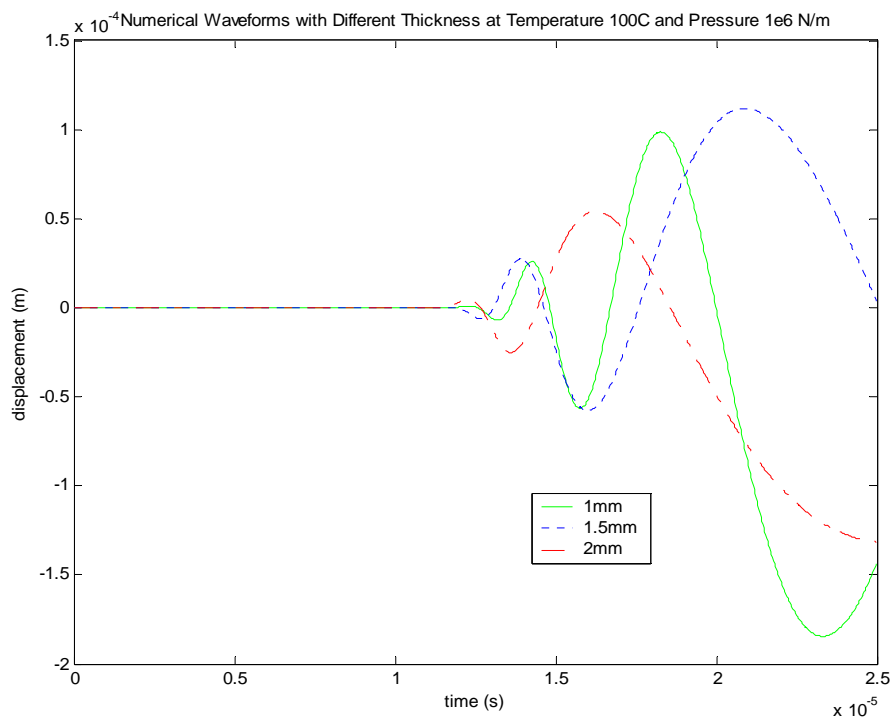


Fig. 6.28. Waveforms of three different thicknesses at $T=100^{\circ}\text{C}$ and $P=1 \times 10^6$ N/m

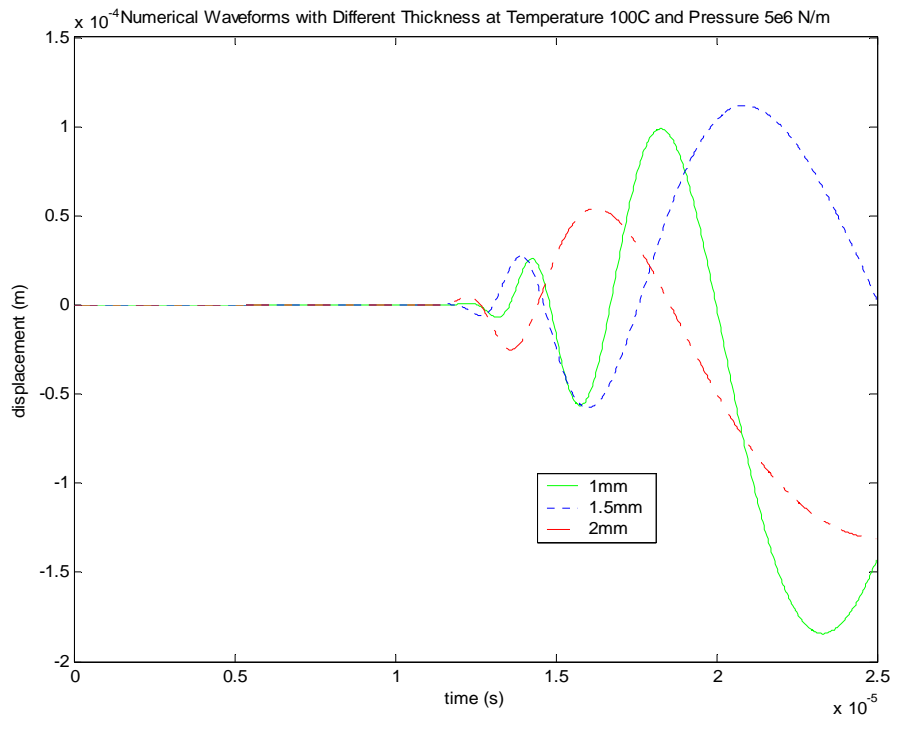


Fig. 6.29. Waveforms of three different thicknesses at $T=100^{\circ}\text{C}$ and $P=5 \times 10^6$ N/m

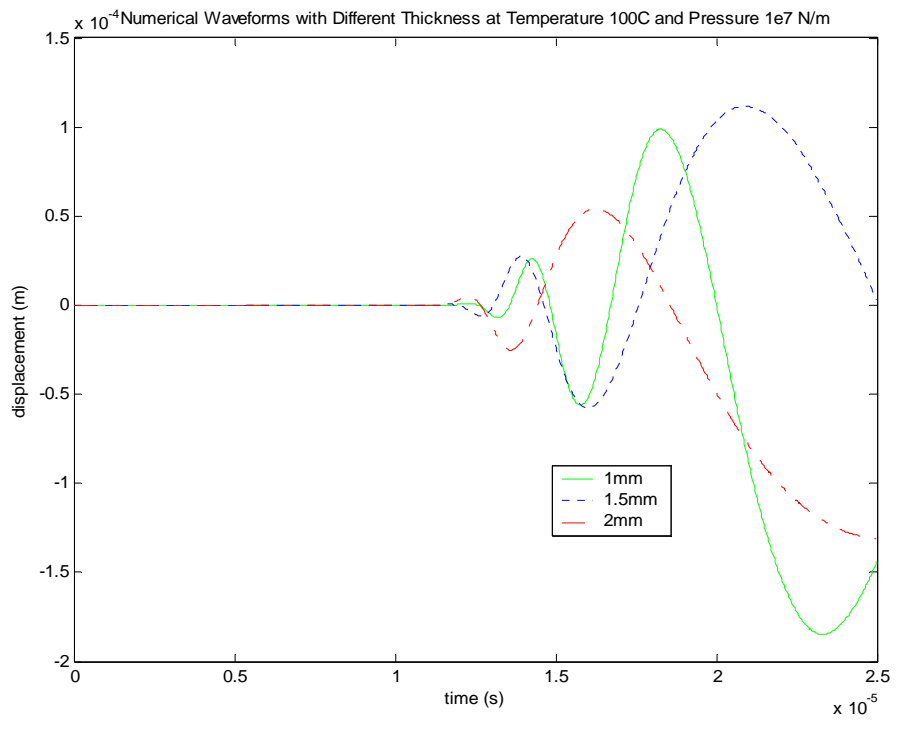


Fig. 6.30. Waveforms of three different thicknesses at $T=100^{\circ}\text{C}$ and $P=1 \times 10^7$ N/m

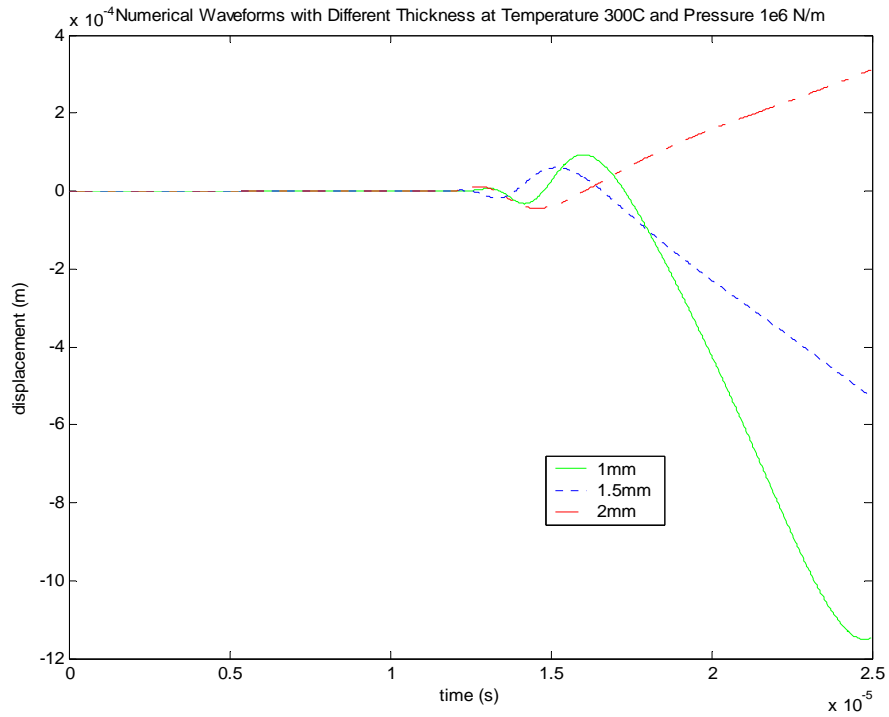


Fig. 6.31. Waveforms of three different thicknesses at $T=300^{\circ}\text{C}$ and $P=1 \times 10^6$ N/m

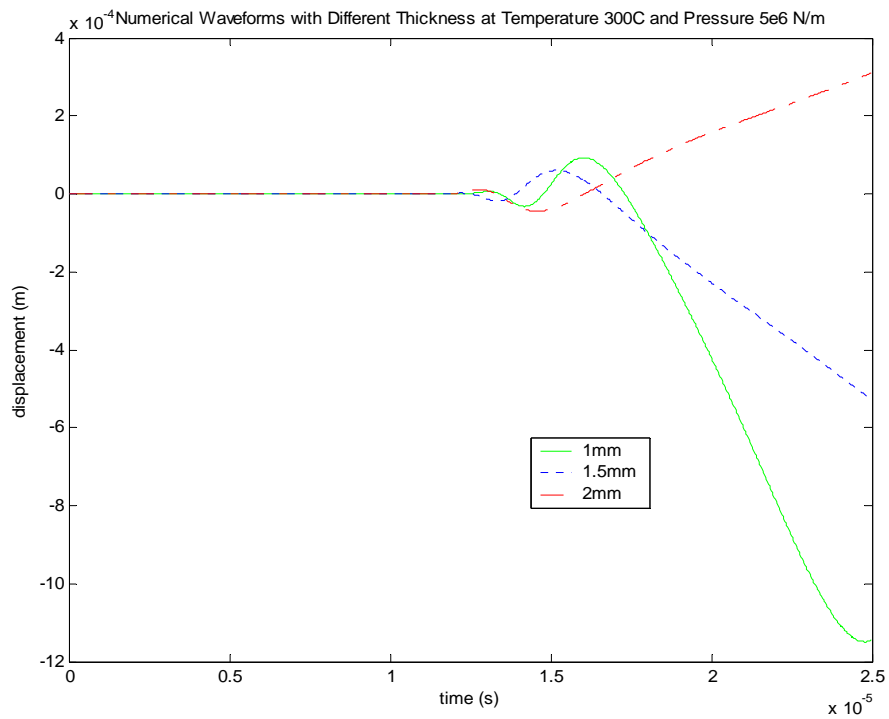


Fig. 6.32. Waveforms of three different thicknesses at $T=300^{\circ}\text{C}$ and $P=5 \times 10^6$ N/m

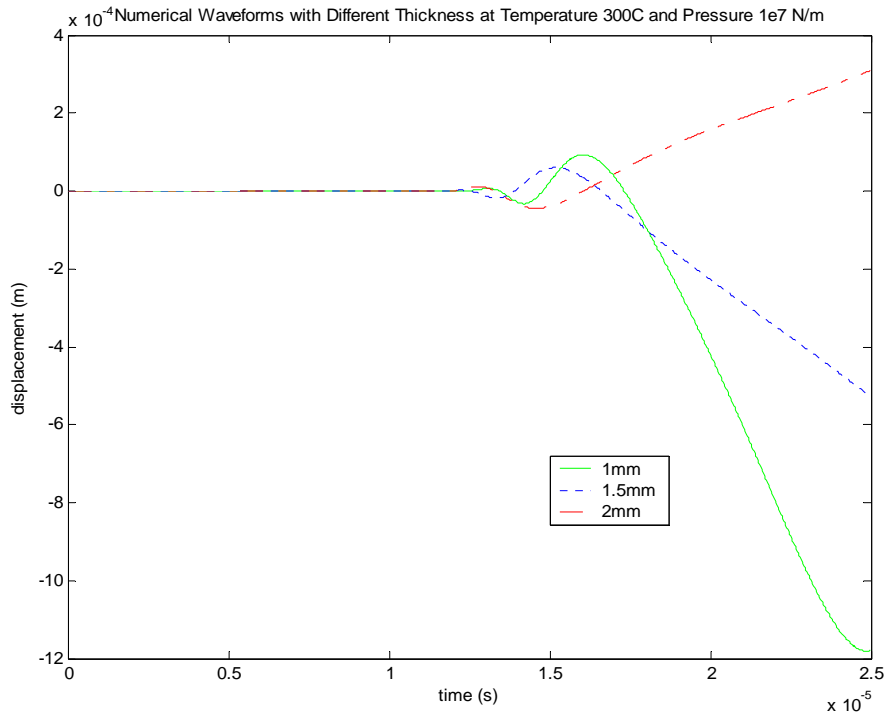


Fig. 6.33. Waveforms of three different thicknesses at $T=300^{\circ}\text{C}$ and $P=1 \times 10^7 \text{ N/m}$

6.4. Extraction of Dispersion Curves

A dispersion curve plots wave group velocities as functions of wave frequency. In order to obtain the dispersion curves for each case considered in Figs. 6.1-6.33, all corresponding numerical waveforms are resolved in the time-frequency domain using the Gabor wavelet transform (GWT). Figs. 6.34 and 6.35 show, respectively, the waveforms acquired from Position 1 and 2, which correspond to $P=1 \times 10^6 \text{ N/m}$, $T=25^{\circ}\text{C}$ and $d=1 \text{ mm}$. The GWT of the two waveforms are given in Figs. 6.36 and 6.37.

The arrival time of a certain frequency component can be determined by finding the maximum GWT coefficient magnitude in time. Once the arrival times of the frequency component at the two acquisition locations are extracted, the time laps taken for the frequency to cover the 10mm propagation path is then used to determine the wave group velocity of the frequency. As an example, assume the arrival time of the frequency component 500 kHz at Position 1 to be t_1 (see Fig. 6.36), the arrival time at Position 2 to

be t_2 (see Fig. 6.37) and the distance between the two positions is D . The group velocity of the 500 kHz component is then

$$V_{group} = D / (t_1 - t_2) \quad (6.1)$$

The wave group velocity $V_{group}(\omega)$ of any frequency component, ω , can be determined using the same approach as

$$V_{group}(\omega) = D / (t_1(\omega) - t_2(\omega)) \quad (6.2)$$

By plotting group velocities as functions of frequency components, dispersion curve are obtained.

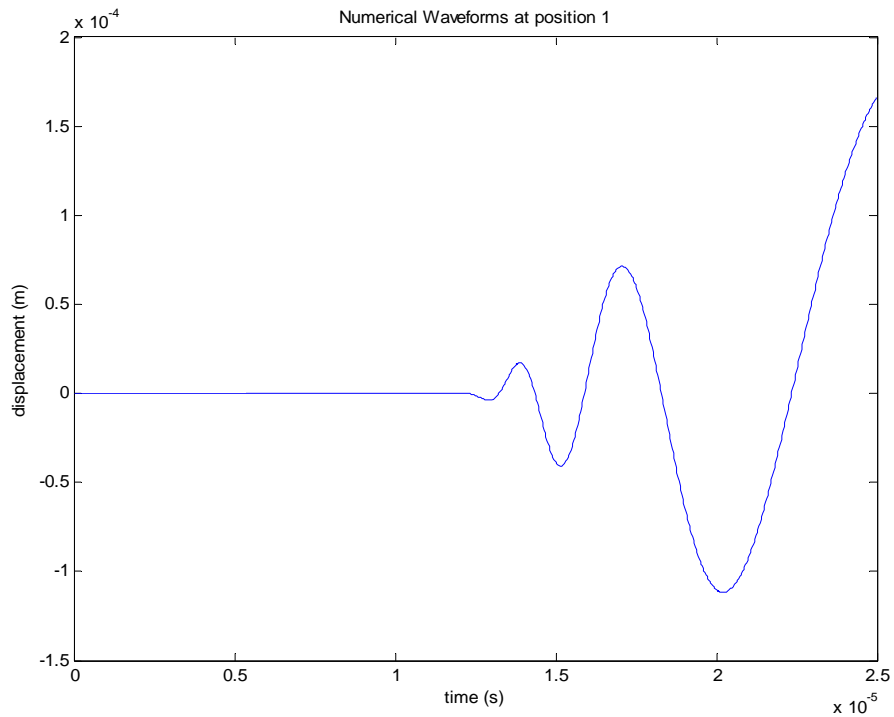


Fig. 6.34. Numerical waveform at position 1 corresponds to $P=1 \times 10^6$ N/m, $T=25^\circ\text{C}$ and $d=1$ mm

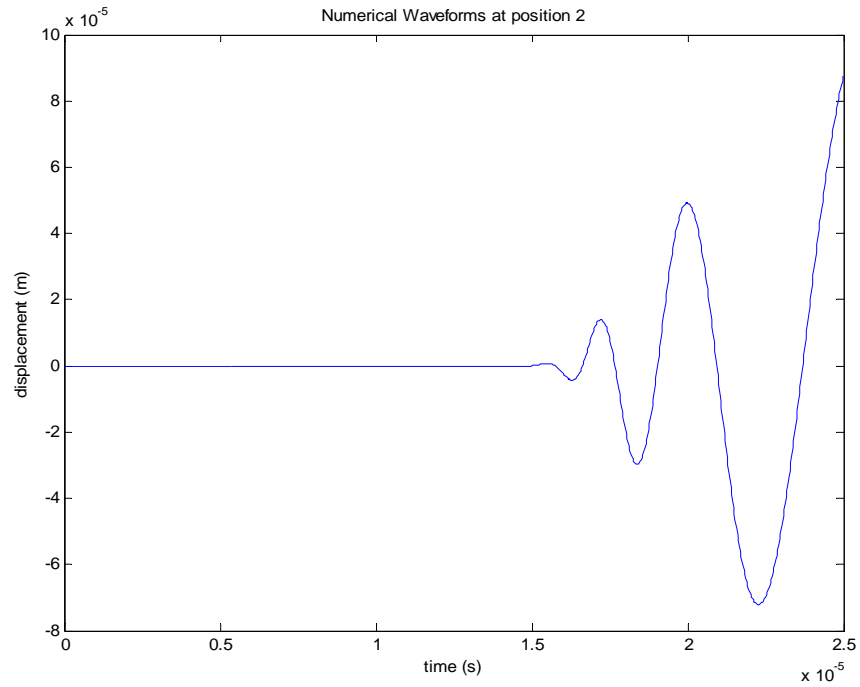


Fig. 6.35. Numerical waveform at position 2 corresponds to $P=1 \times 10^6$ N/m, $T=25^\circ\text{C}$ and $d=1$ mm

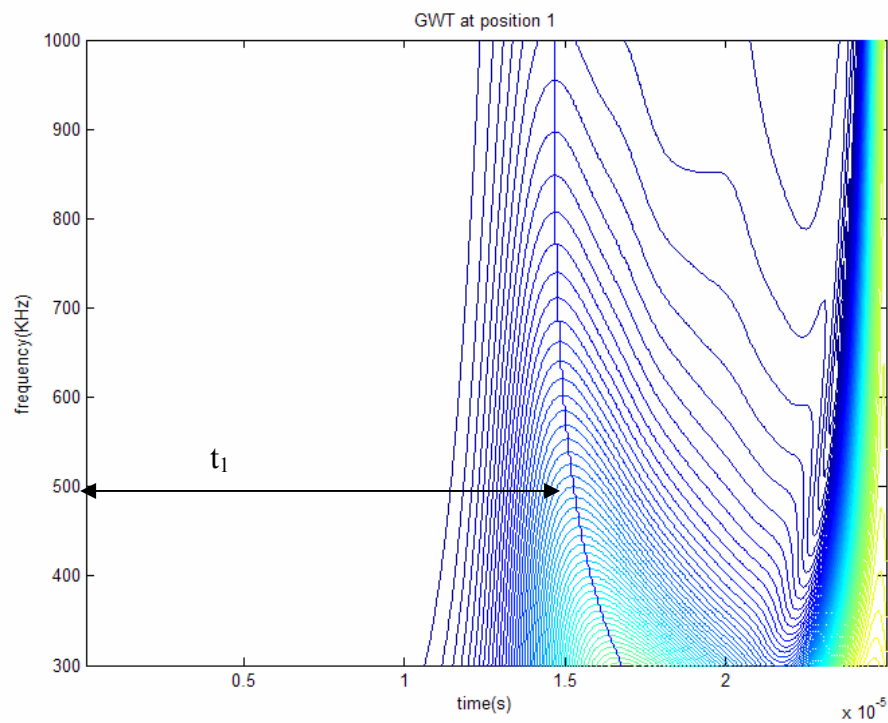


Fig. 6.36. GWT of the waveform in Fig. 6.34

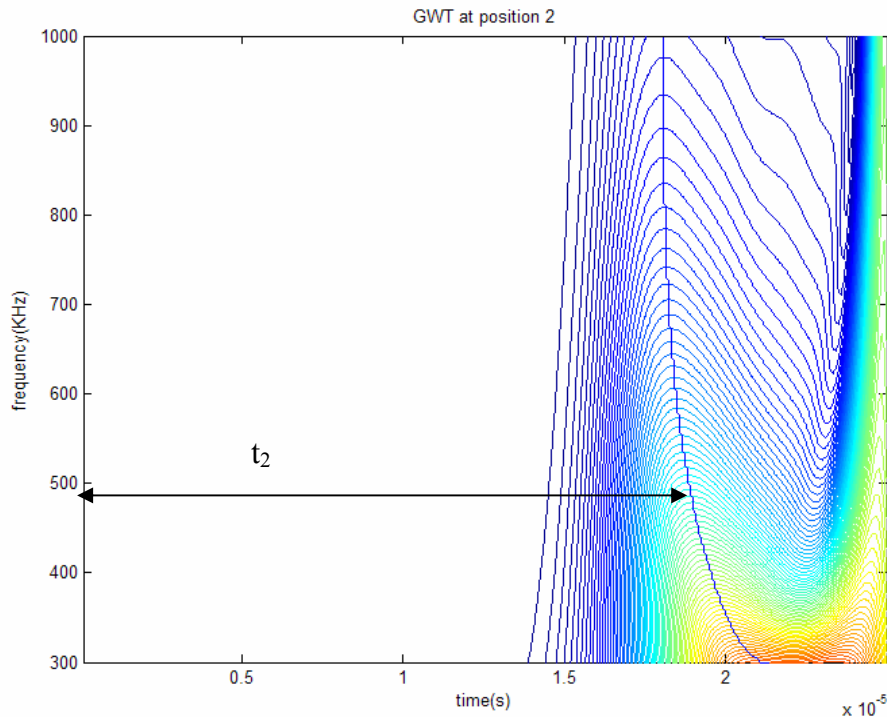


Fig. 6.37. GWT of the waveform in Fig. 6.35

6.5. Wave Dispersion at Different Pressures

Figs.6.38-6.41 show the dispersion curves for three different pressures at $d=1\text{mm}$ and $T=25^\circ\text{C}$, 50°C , 100°C and 300°C . Figs. 6.42-6.45 present the dispersion curves for the same pressures and temperatures at $d=1.5\text{mm}$. The dispersion curves correspond to the same pressures and temperatures at $d=2.0\text{mm}$ are found in Figs. 6.46-6.49. In all figures, the horizontal axis represents the frequency in kHz and the vertical axis represents the group velocity in m/s. The frequency range considered is 300-500 kHz.

It can be observed from Figs. 6.38-6.49 that the differences between the dispersion curves in response to different pressures are small. However, one can still conclude that smaller the thickness, the easier it is to identify the pressure induced effects. From Figs. 6.38, 6.42 and 6.46, which show the dispersion curves correspond to three different pressures at $T= 25^\circ\text{C}$ and $d=1\text{mm}$, 1.5mm and 2mm , one can see that dispersion curves are more sensitive to the thinner plate ($d=1.0\text{mm}$) than to thicker plates ($d=1.5\text{mm}$ and 2.0mm .) This is consistent for all the temperatures considered except for $T=300^\circ\text{C}$. One

other conclusion is that, in thin plates, higher the pressure, lower the wave group velocity, as is evident from Figs. 6.38-6.40. It should be noted that the intersection of dispersion curves seen in Figs. 6.39 and 6.40 is due to numerical errors.

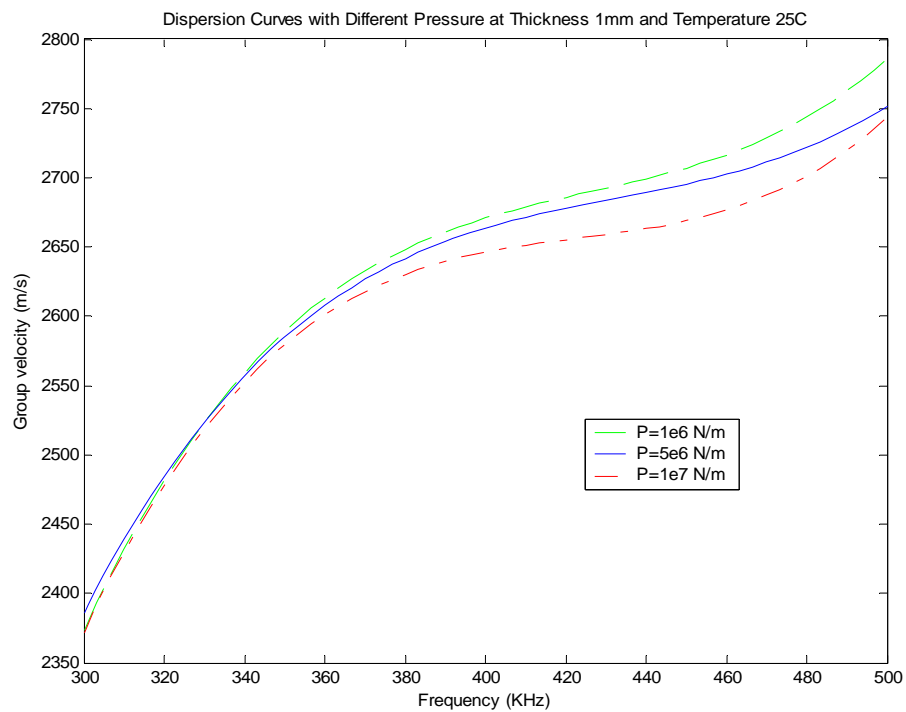


Fig. 6.38. Dispersion curves for three different pressures at $d=1.0\text{mm}$ and $T=25^\circ\text{C}$

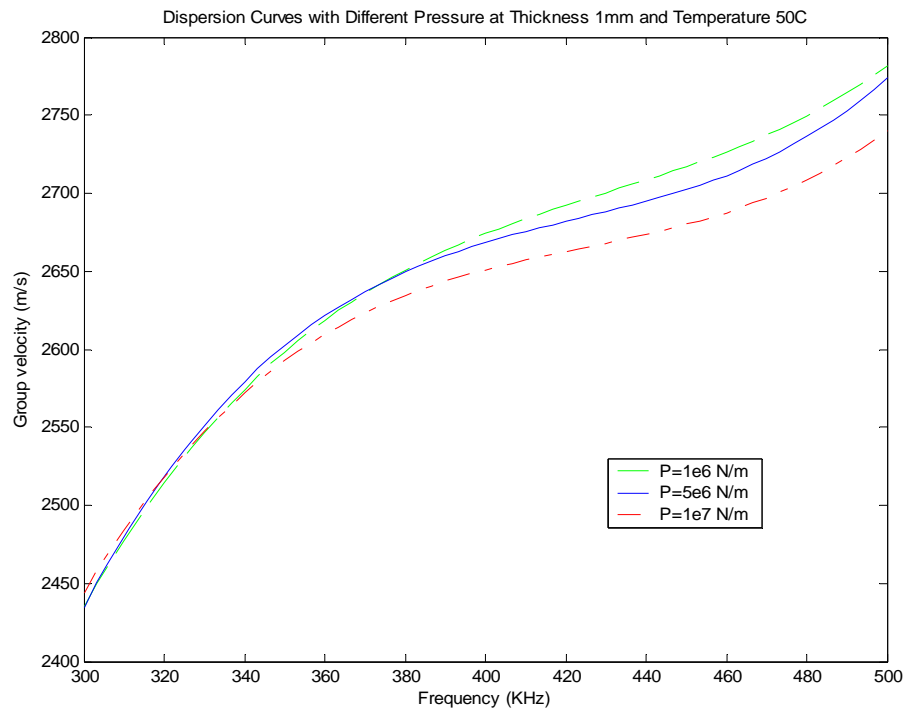


Fig. 6.39. Dispersion curves for three different pressures at $d=1.0\text{mm}$ and $T=50^\circ\text{C}$

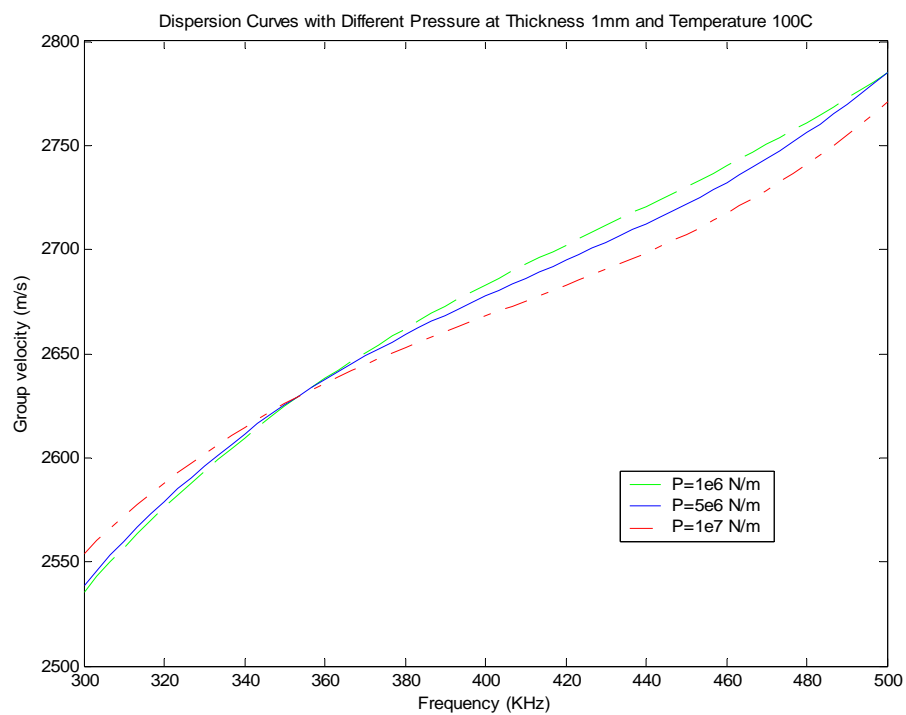


Fig. 6.40. Dispersion curves for three different pressures at $d=1.0\text{mm}$ and $T=100^\circ\text{C}$

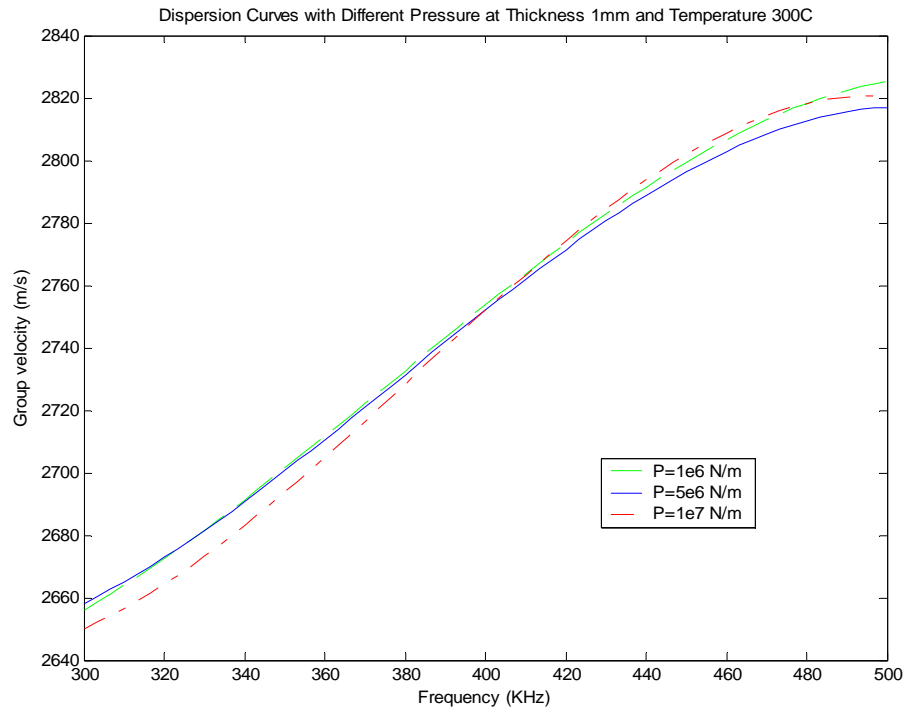


Fig. 6.41. Dispersion curves for three different pressures at $d=1.0\text{mm}$ and $T=300^\circ\text{C}$

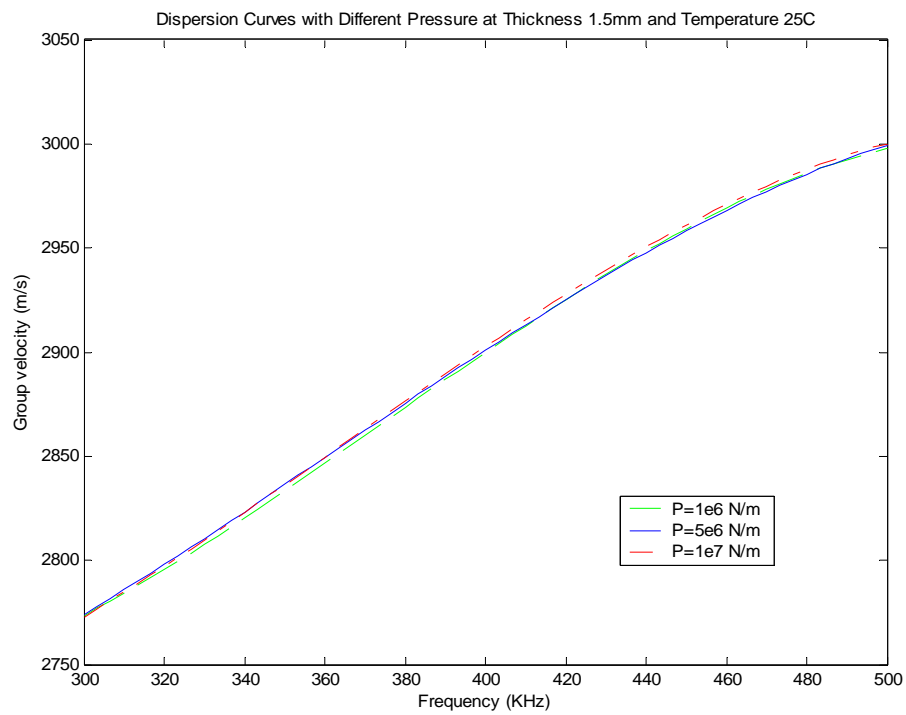


Fig. 6.42. Dispersion curves for three different pressures at $d=1.5\text{mm}$ and $T=25^\circ\text{C}$

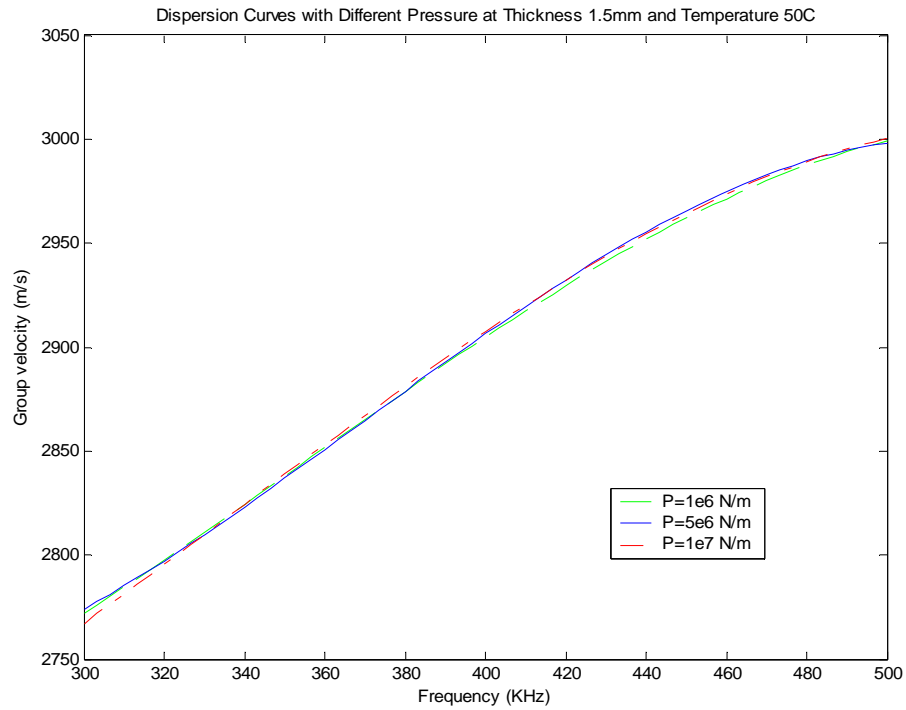


Fig. 6.43. Dispersion curves for three different pressures at $d=1.5\text{mm}$ and $T=50^\circ\text{C}$

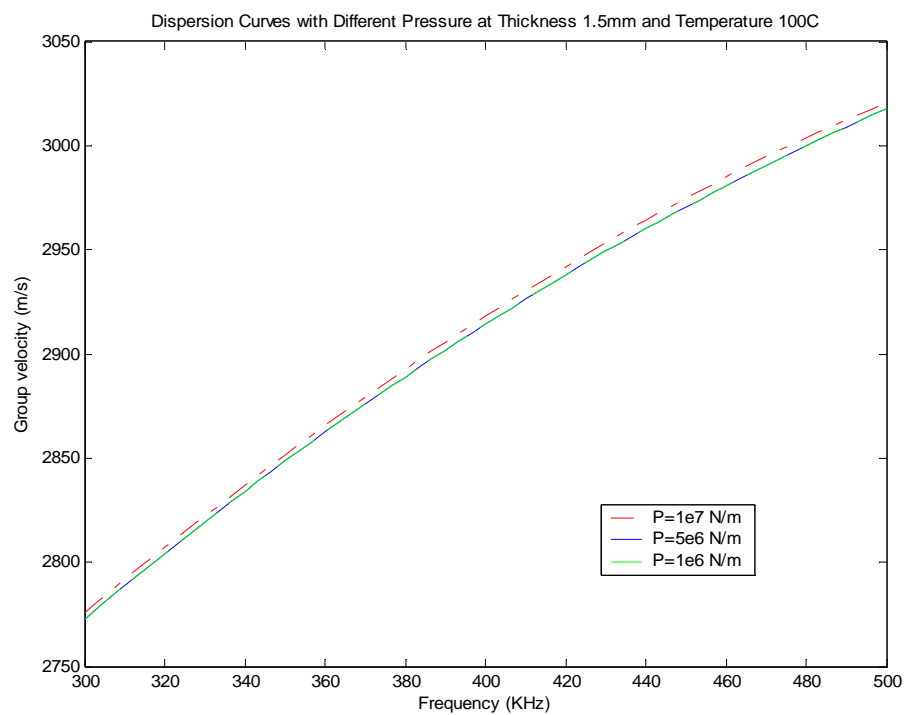


Fig. 6.44. Dispersion curves for three different pressures at $d=1.5\text{mm}$ and $T=100^\circ\text{C}$

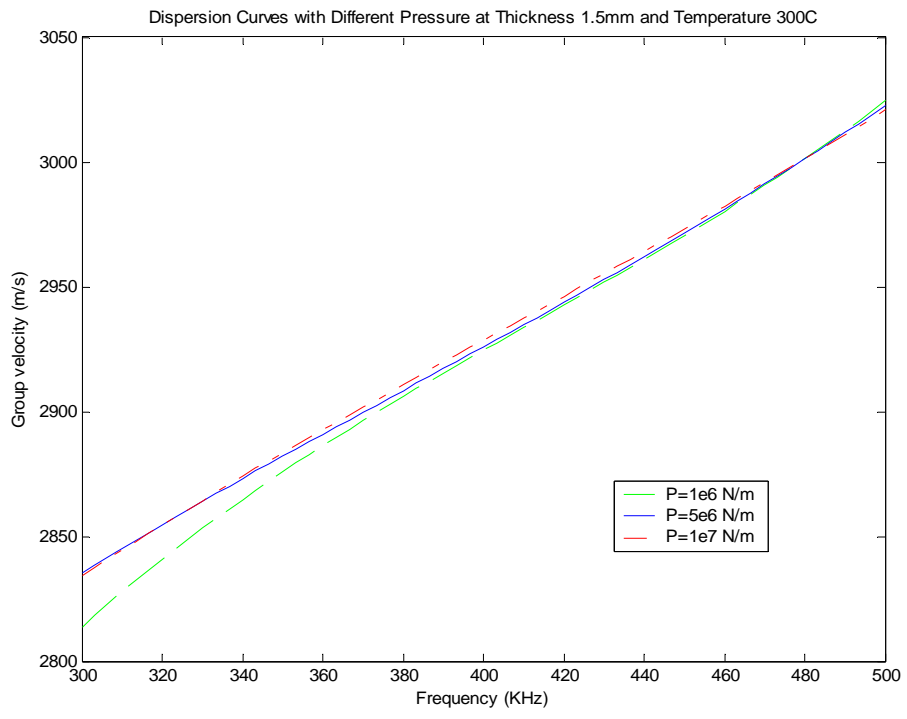


Fig. 6.45. Dispersion curves for three different pressures at $d=1.5\text{mm}$ and $T=300^\circ\text{C}$

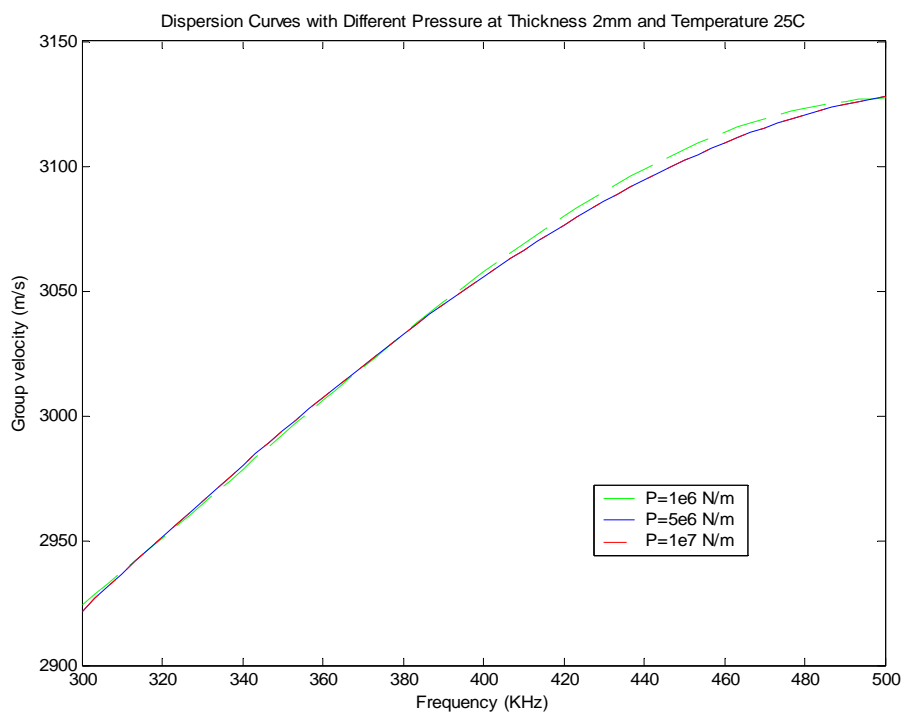


Fig. 6.46. Dispersion curves for three different pressures at $d=2.0\text{mm}$ and $T=25^\circ\text{C}$

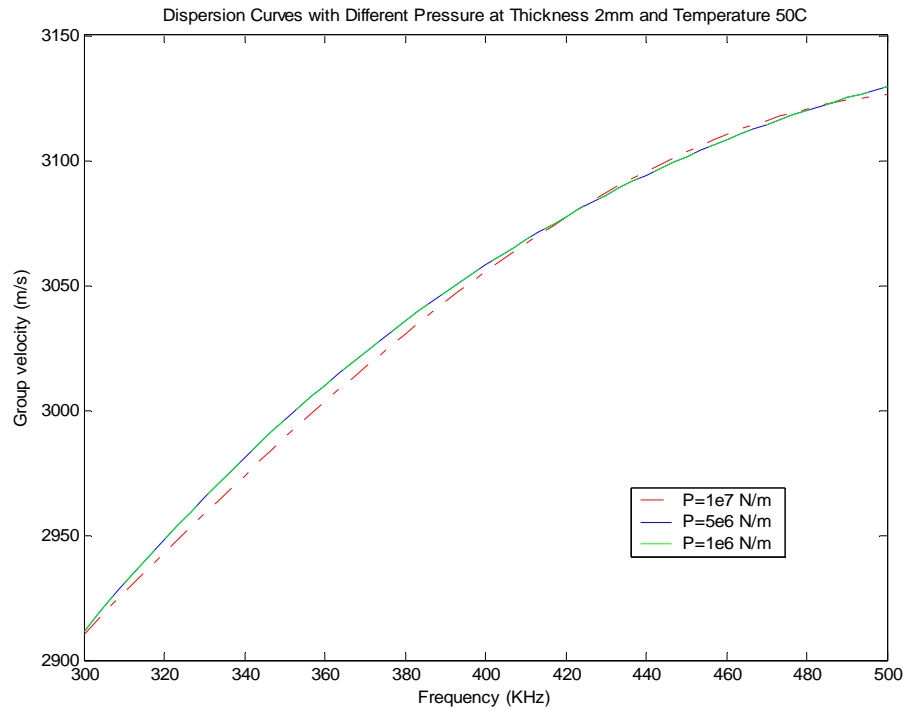


Fig. 6.47. Dispersion curves for three different pressures at $d=2.0\text{mm}$ and $T=50^\circ\text{C}$

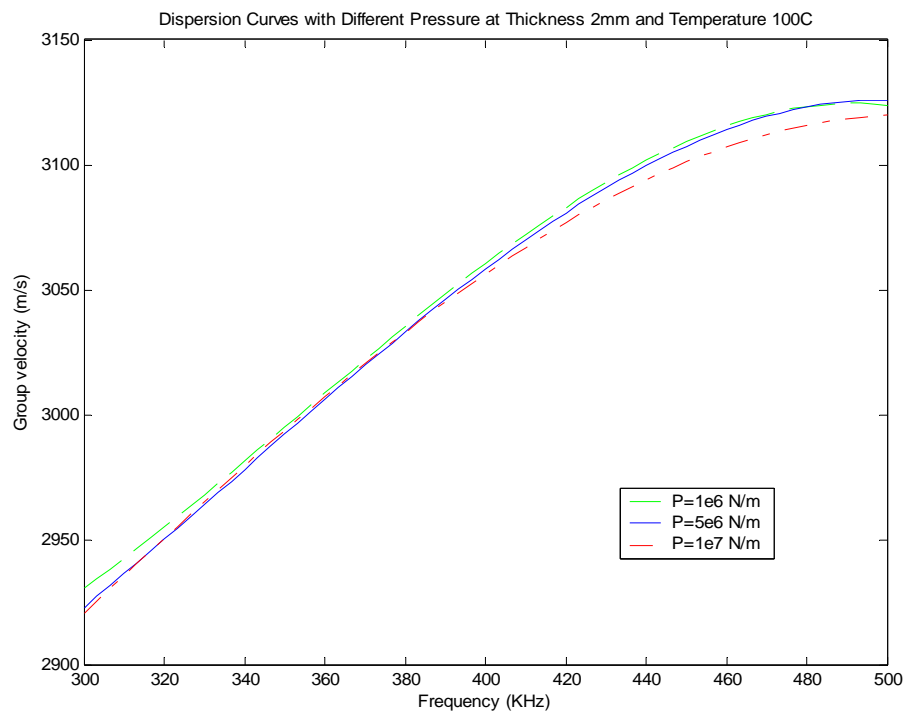


Fig. 6.48. Dispersion curves for three different pressures at $d=2.0\text{mm}$ and $T=100^\circ\text{C}$

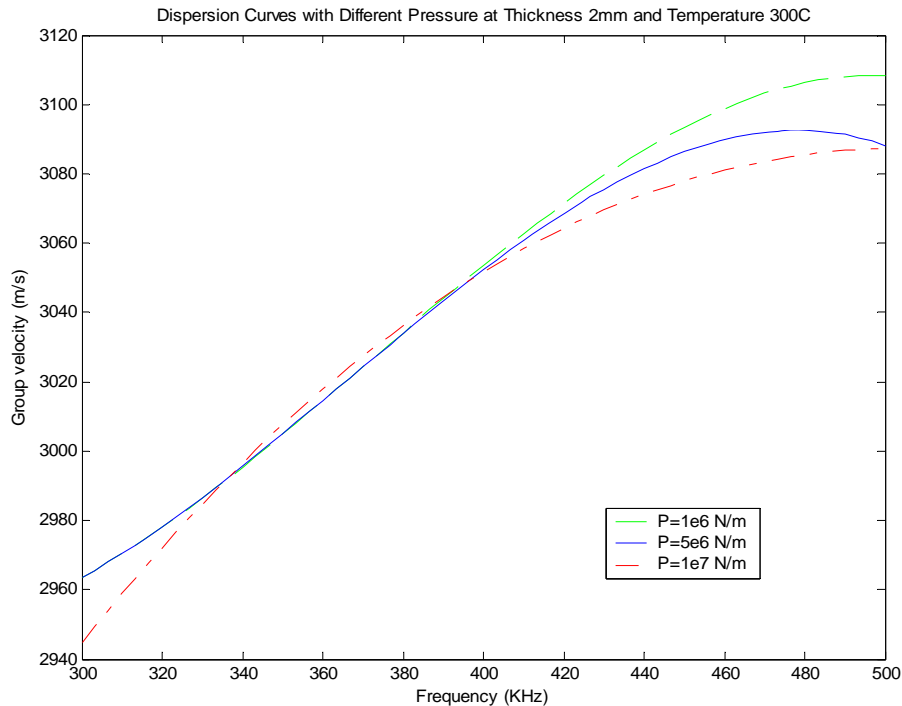


Fig. 6.49. Dispersion curves for three different pressures at $d=2.0\text{mm}$ and $T=300^\circ\text{C}$

6.6. Wave Dispersion at Different Temperatures

The dispersion curves for four different temperatures at a specific pressure and thickness are presented in the section. Figs. 6.50-6.52 show the dispersion curves for four different temperatures at $d=1\text{mm}$ and $P=1 \times 10^6 \text{ N/m}$, $5 \times 10^6 \text{ N/m}$ and $1 \times 10^7 \text{ N/m}$. Figs. 6.53-6.55 present the dispersion curves for the same temperatures and pressures at $d=1.5\text{mm}$. The dispersion curves correspond to the same temperatures and pressures at $d=2.0\text{mm}$ are given in Figs. 6.56-6.58. In all figures, again, the horizontal axis represents the frequency in kHz and the vertical axis represents the group velocity in m/s. The frequency range between 300kHz and 500kHz is again considered.

The differences between dispersion curves in response to different temperatures are prominent in Fig. 6.50-6.58. From Figs. 6.50, 6.53 and 6.56, one can conclude that smaller the thickness, the easier it is to resolve temperature. In addition, as can be observed from Figs. 6.50-6.52 that for thin plates, higher the temperature, higher the wave group velocity.

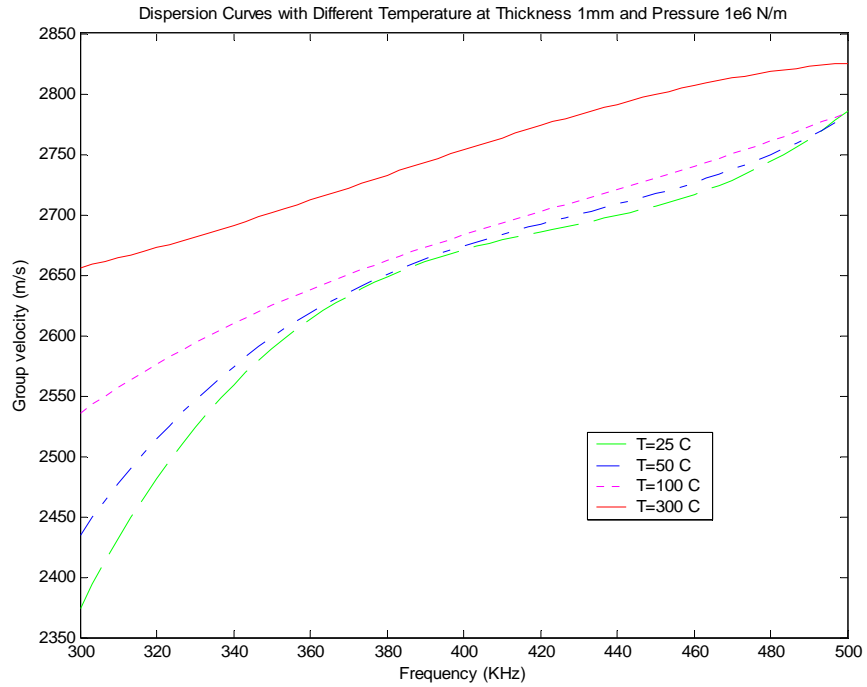


Fig. 6.50. Dispersion curves for four different temperatures at $d=1.0\text{mm}$ and $P=1 \times 10^6 \text{ N/m}$

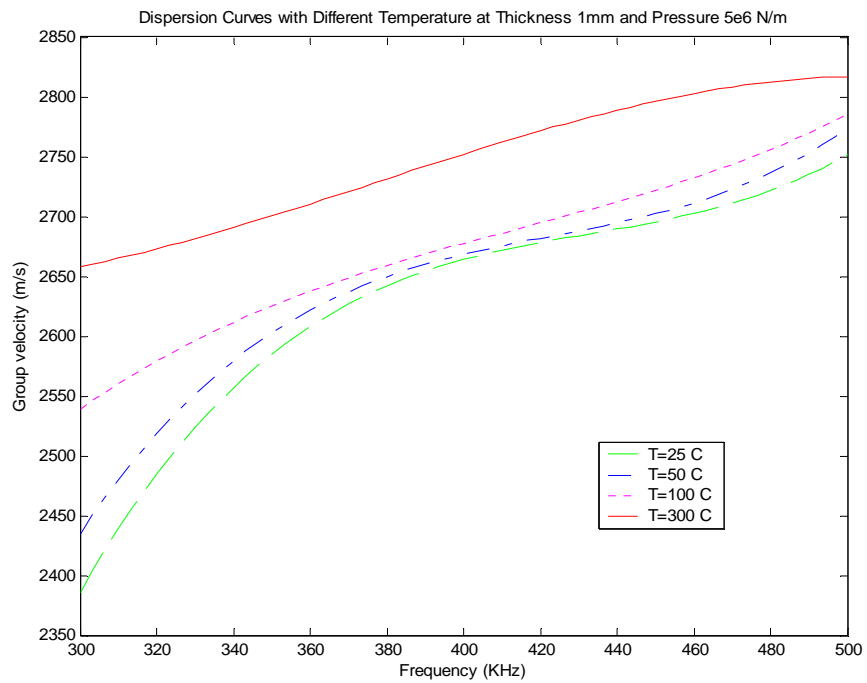


Fig. 6.51. Dispersion curves for four different temperatures at $d=1.0\text{mm}$ and $P=5 \times 10^6 \text{ N/m}$

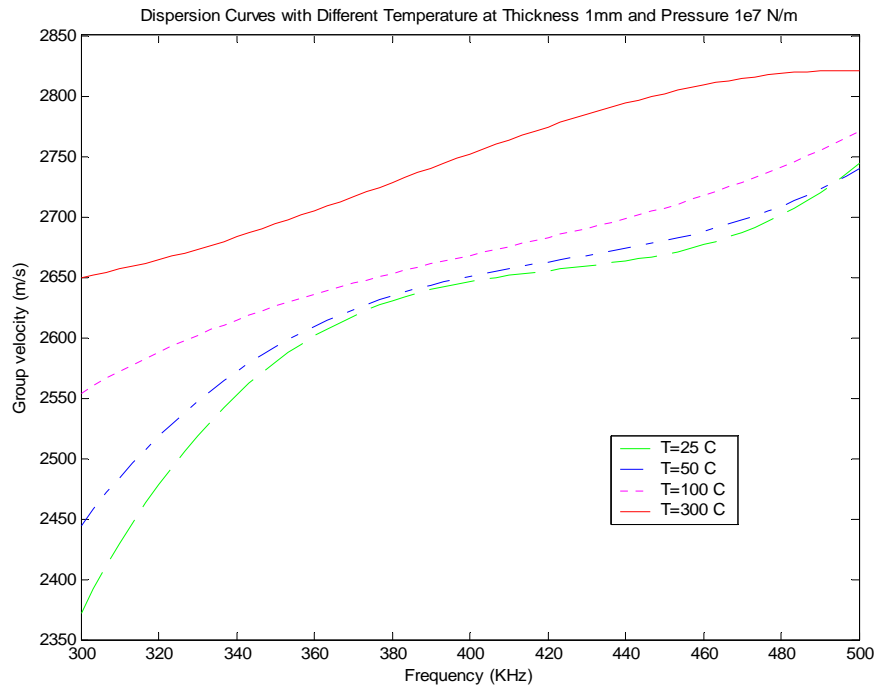


Fig. 6.52. Dispersion curves for four different temperatures at $d=1.0\text{mm}$ and $P=1 \times 10^7$ N/m

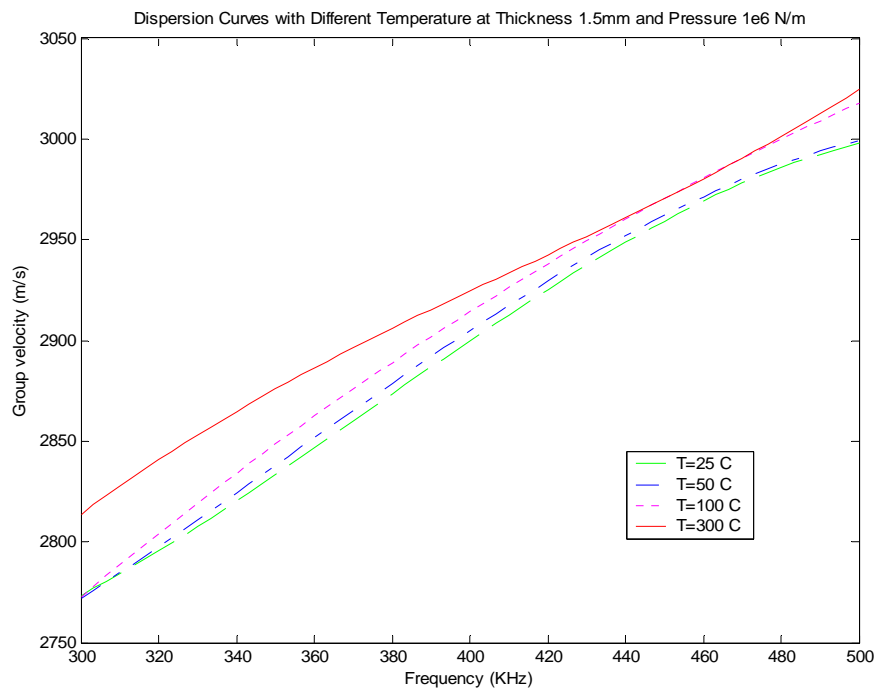


Fig. 6.53. Dispersion curves for four different temperatures at $d=1.5\text{mm}$ and $P=1 \times 10^6$ N/m

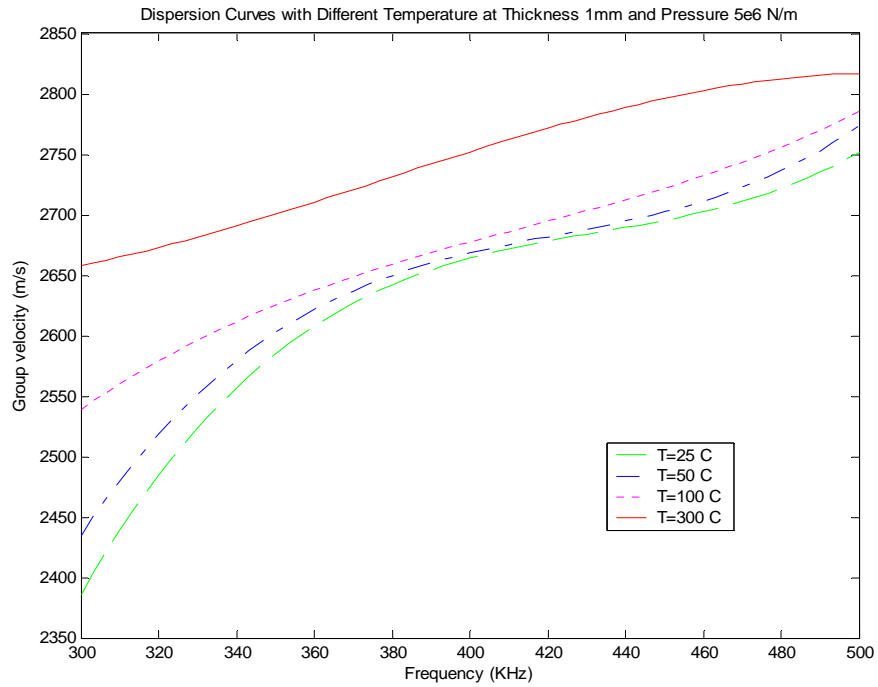


Fig. 6.54. Dispersion curves for four different temperatures at $d=1.5\text{mm}$ and $P=5 \times 10^6 \text{ N/m}$

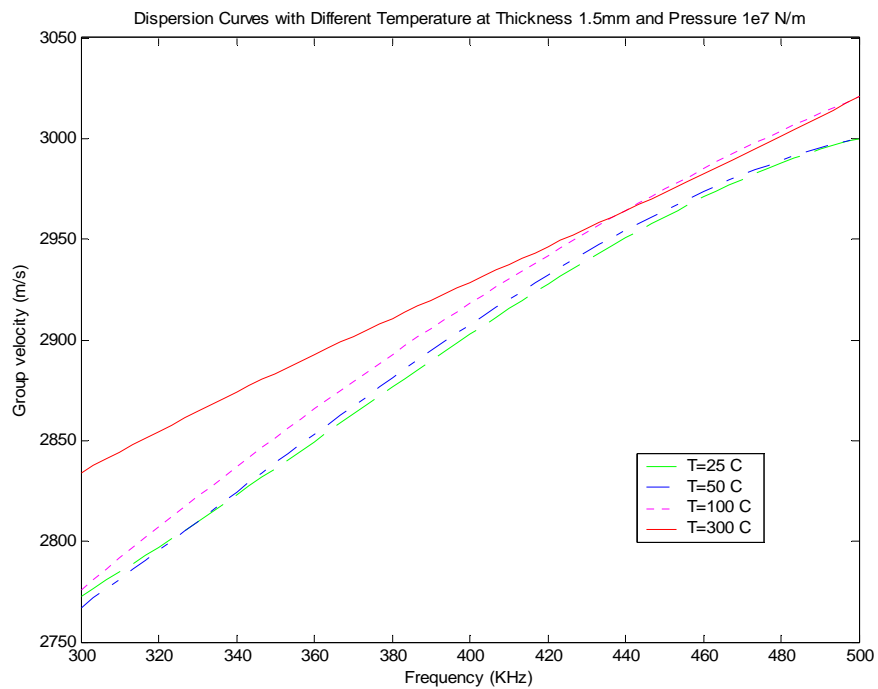


Fig. 6.55. Dispersion curves for four different temperatures at $d=1.5\text{mm}$ and $P=1 \times 10^7 \text{ N/m}$

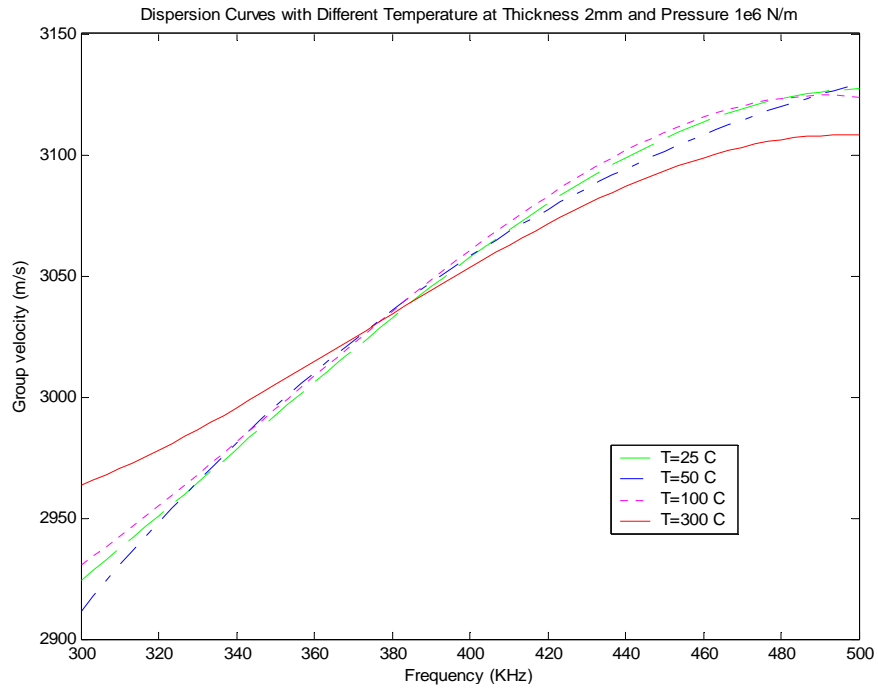


Fig. 6.56. Dispersion curves for four different temperatures at $d=2.0\text{mm}$ and $P=1 \times 10^6 \text{ N/m}$

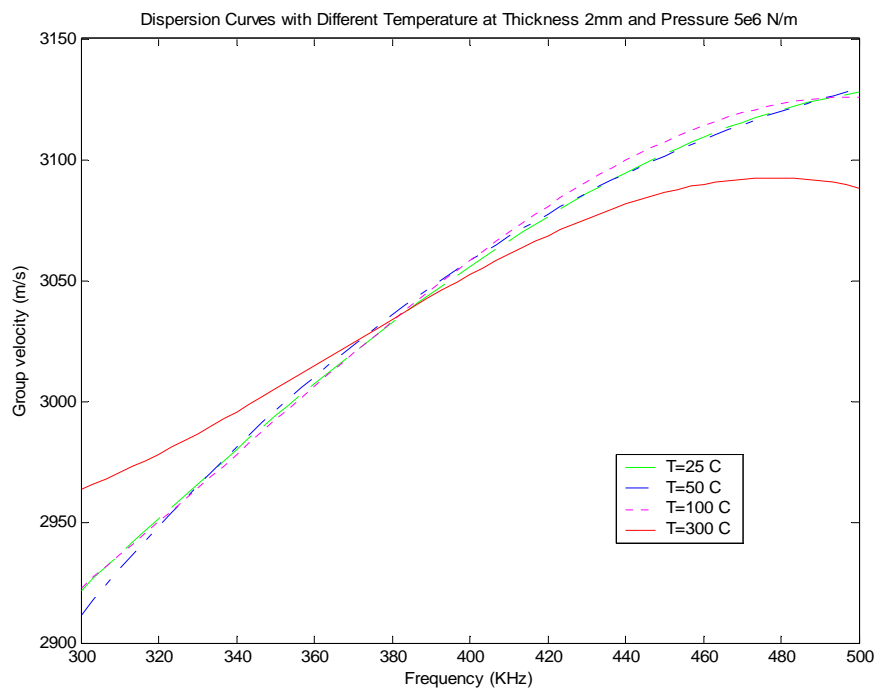


Fig. 6.57. Dispersion curves for four different temperatures at $d=2.0\text{mm}$ and $P=5 \times 10^6 \text{ N/m}$

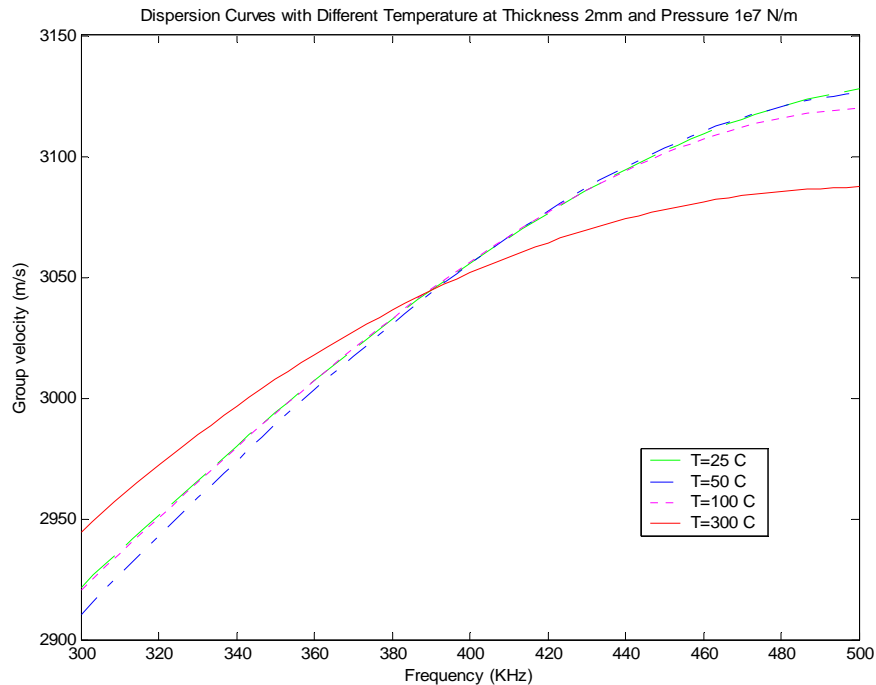


Fig. 6.58. Dispersion curves for four different temperatures at $d=2.0\text{mm}$ and $P=1 \times 10^7 \text{ N/m}$

6.7. Wave Dispersion at Different Thicknesses

The dispersion curves for three different thicknesses at a specific pressure and temperature are presented in the followings. Figs.6.59-6.61 show the dispersion curves for three different thicknesses at $T=25^\circ\text{C}$ and $P=1 \times 10^6 \text{ N/m}$, $5 \times 10^6 \text{ N/m}$ and $1 \times 10^7 \text{ N/m}$. Figs. 6.62-6.64 present the dispersion curves for the same thicknesses and pressures at $T=50^\circ\text{C}$. The dispersion curves correspond to the same thicknesses and pressures at $T=100^\circ\text{C}$ and $T=300^\circ\text{C}$ are found in Figs. 6.65-6.67 and Figs. 6.68-6.70, respectively. Again, in all figures, the horizontal axis represents the frequency in kHz and the vertical axis represents the group velocity in m/s. The same range of frequency, 300-500kHz, is again considered.

The effect of plate thickness on dispersion curves is significant as can be readily seen in Figs. 6.59-6-70. One observation is that thicker the plate, higher the wave group velocity regardless of the temperature and pressure conditions.

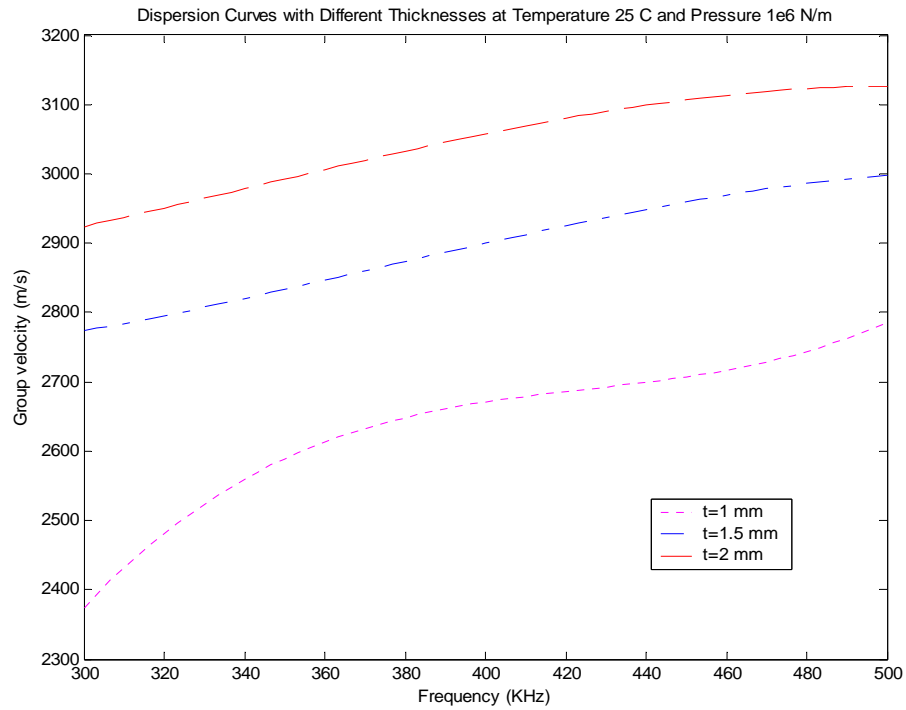


Fig. 6.59. Dispersion curves for three different thicknesses at $T=25^{\circ}\text{C}$ and $P=1 \times 10^6 \text{ N/m}$

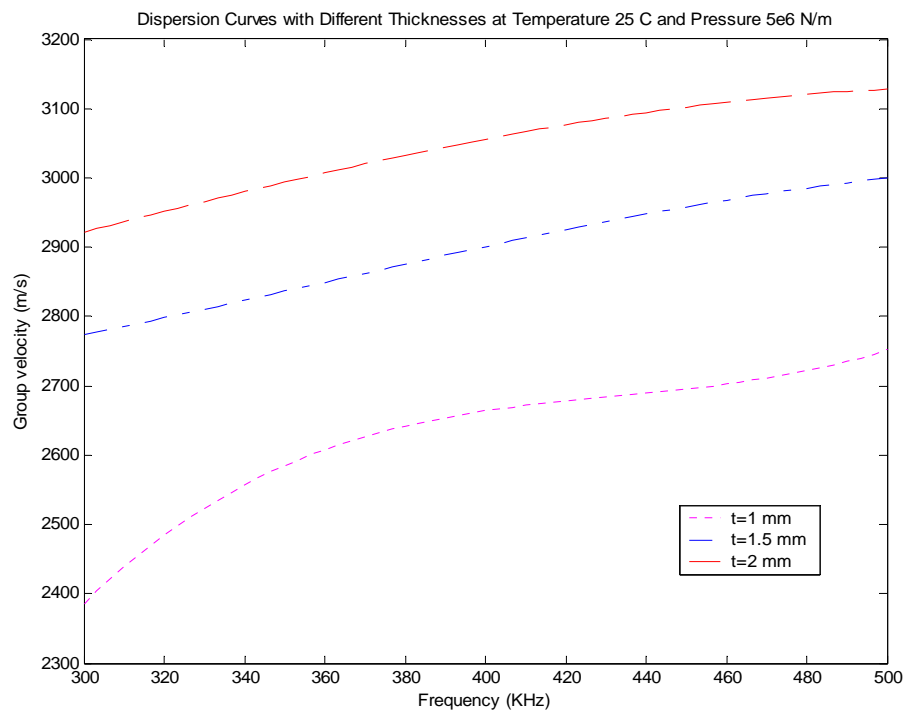


Fig. 6.60. Dispersion curves for three different thicknesses at $T=25^{\circ}\text{C}$ and $P=5 \times 10^6 \text{ N/m}$

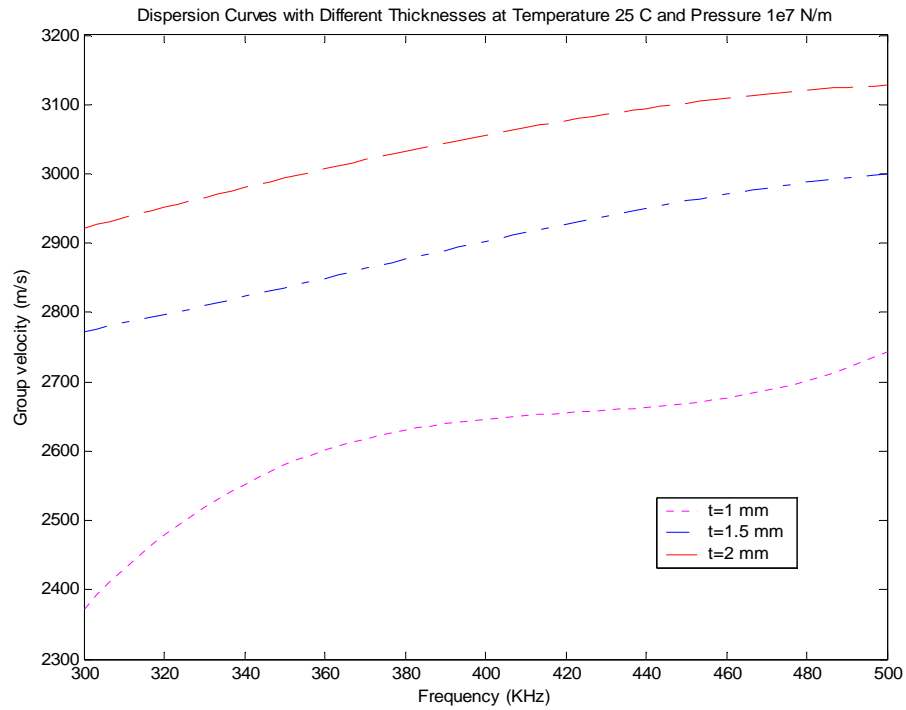


Fig. 6.61. Dispersion curves for three different thicknesses at $T=25^{\circ}\text{C}$ and $P=1 \times 10^7 \text{ N/m}$

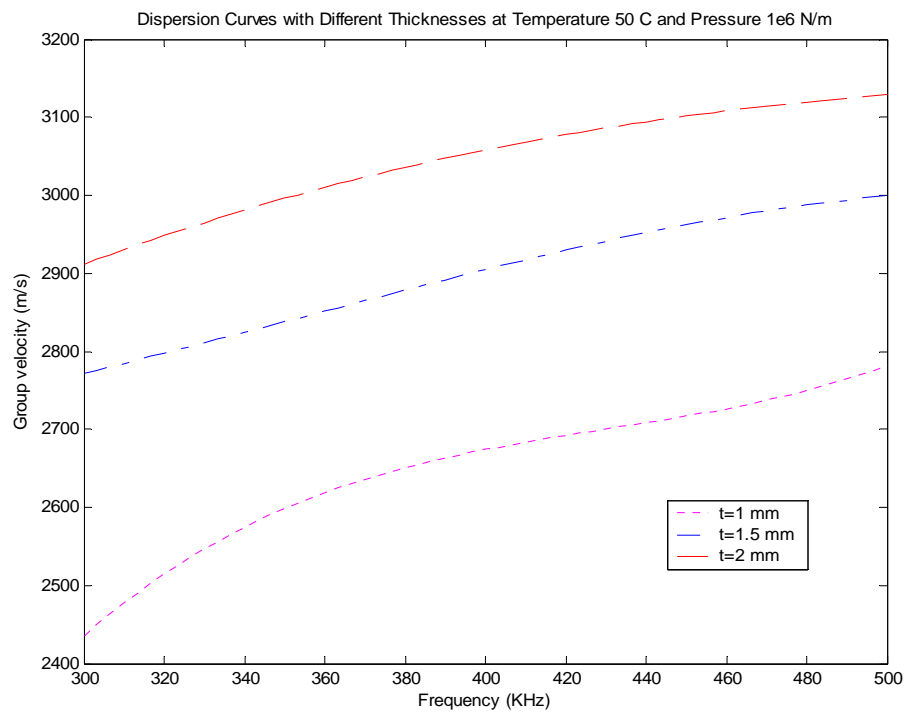


Fig. 6.62. Dispersion curves for three different thicknesses at $T=50^{\circ}\text{C}$ and $P=1 \times 10^6 \text{ N/m}$

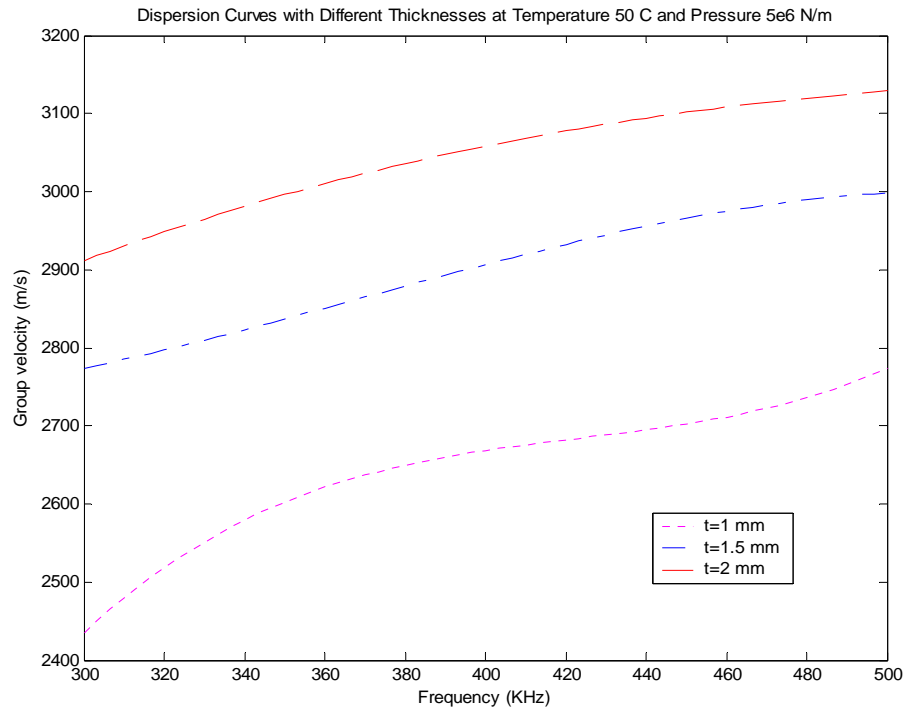


Fig. 6.63. Dispersion curves for three different thicknesses at $T=50^{\circ}\text{C}$ and $P=5 \times 10^6 \text{ N/m}$

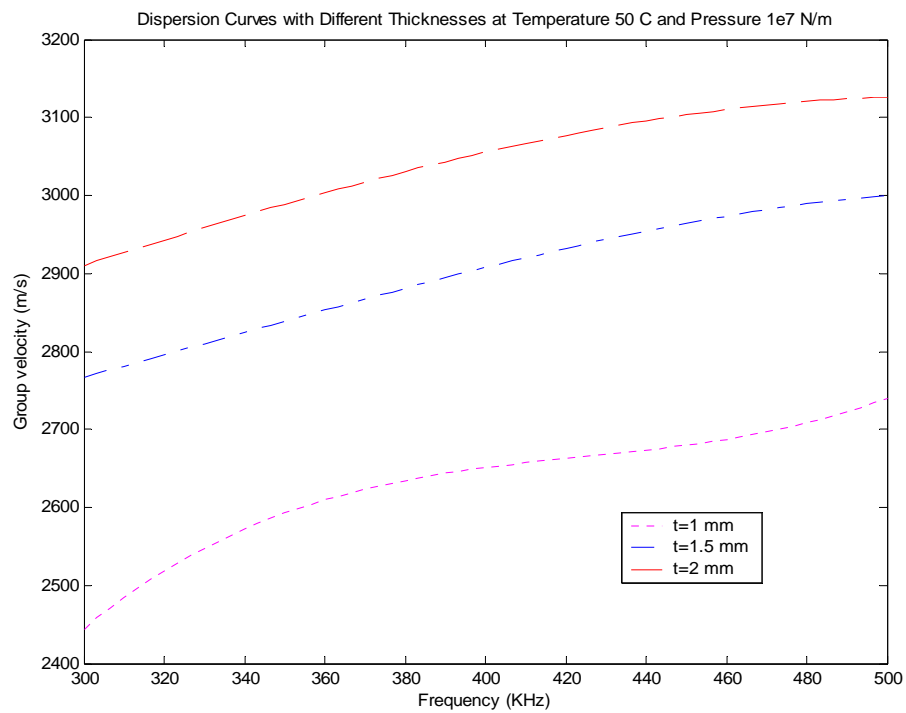


Fig. 6.64. Dispersion curves for three different thicknesses at $T=50^{\circ}\text{C}$ and $P=1 \times 10^7 \text{ N/m}$

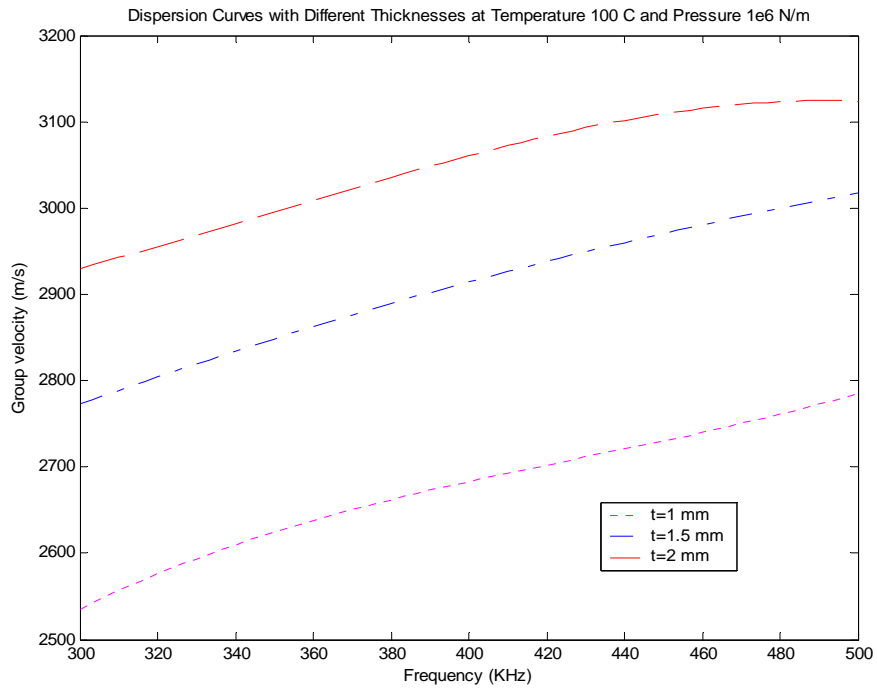


Fig. 6.65. Dispersion curves for three different thicknesses at $T=100^{\circ}\text{C}$ and $P=1 \times 10^6 \text{ N/m}$

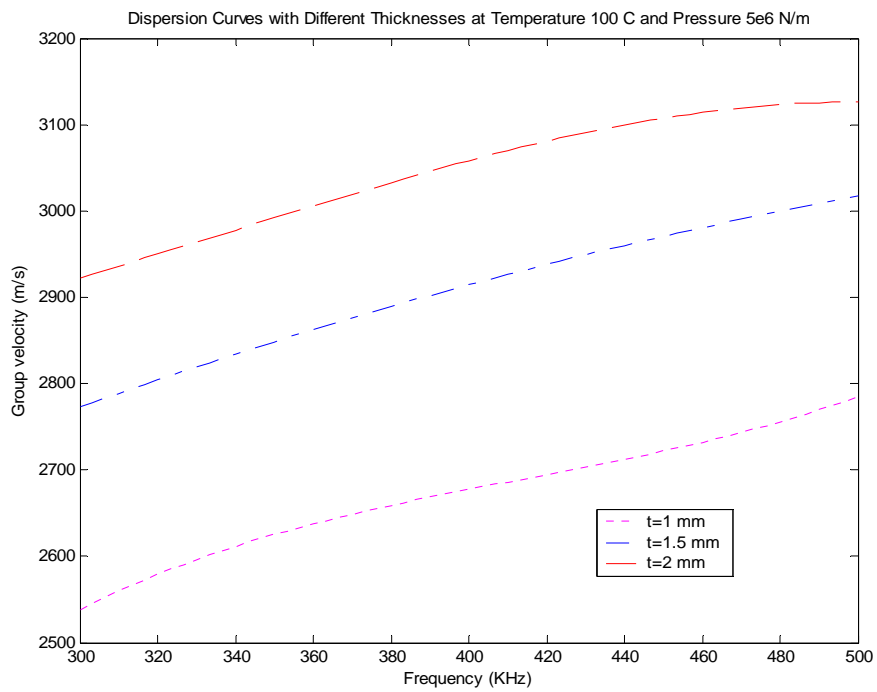


Fig. 6.66. Dispersion curves for three different thicknesses at $T=100^{\circ}\text{C}$ and $P=5 \times 10^6 \text{ N/m}$

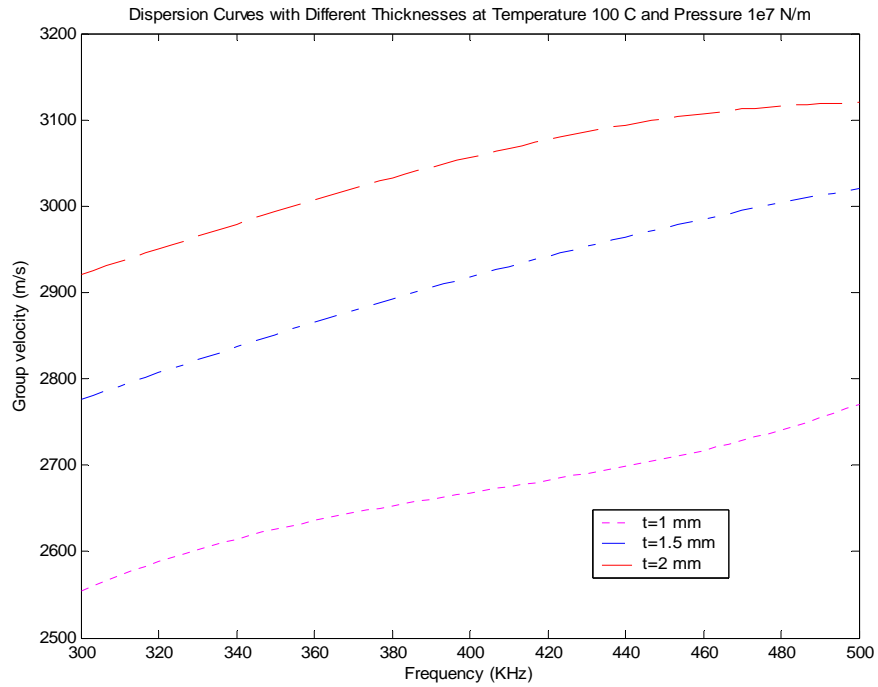


Fig. 6.67. Dispersion curves for three different thicknesses at $T=100^{\circ}\text{C}$ and $P=1 \times 10^7$ N/m

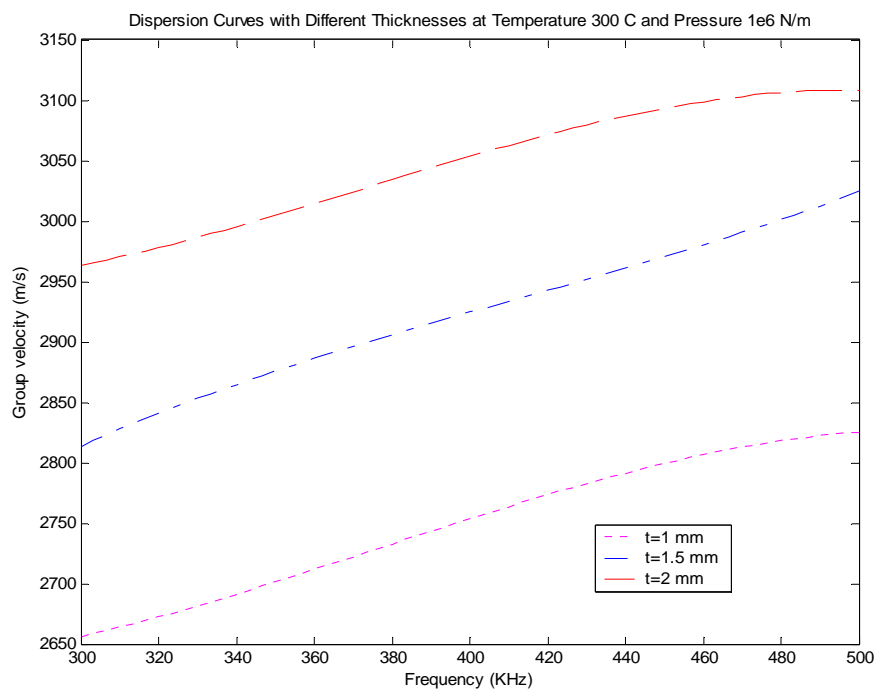


Fig. 6.68. Dispersion curves for three different thicknesses at $T=300^{\circ}\text{C}$ and $P=1 \times 10^6$ N/m

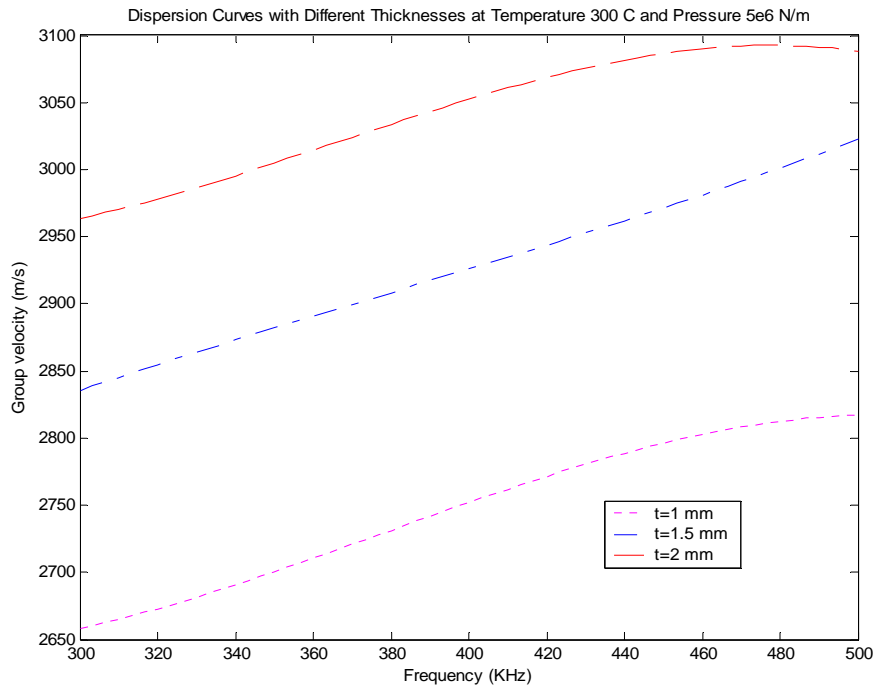


Fig. 6.69. Dispersion curves for three different thicknesses at $T=300^{\circ}\text{C}$ and $P=5 \times 10^6 \text{ N/m}$

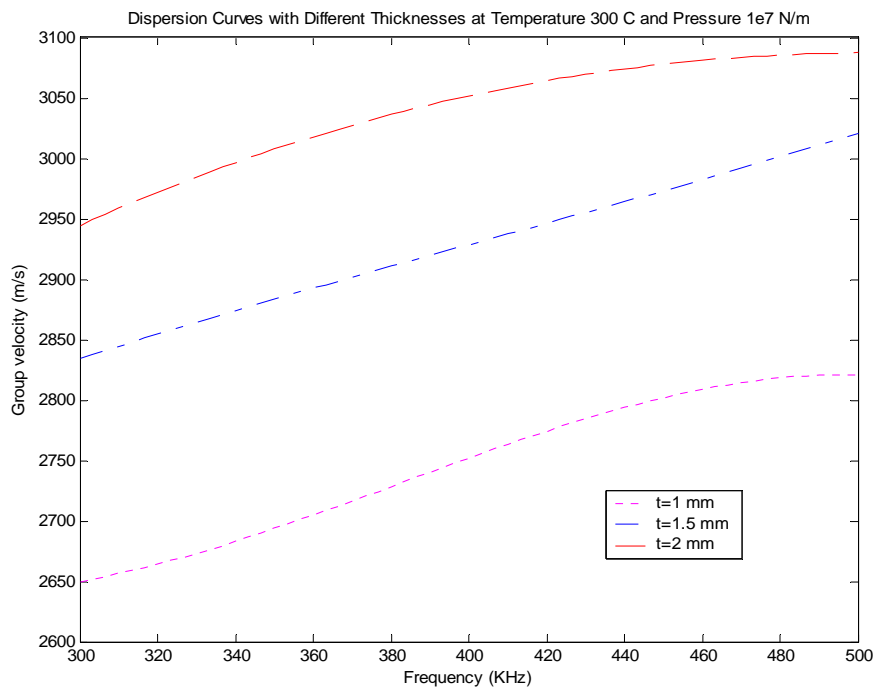


Fig. 6.70. Dispersion curves for three different thicknesses at $T=300^{\circ}\text{C}$ and $P=1 \times 10^7 \text{ N/m}$

6.8. Discussions

In order to easily compare the differences between dispersion curves corresponding to pressure, temperature and thickness effects, 36 dispersion curves are plotted in Fig. 6.71. Group A contains twelve dispersion curves that correspond to the four different temperatures and three different pressures at $d=1.0\text{mm}$. Similarly, Group B and Group C each contain twelve dispersion curves that correspond to the four different temperatures and three different pressures at $d=1.5\text{mm}$ and $d=2.0\text{mm}$, respectively. Groups A, B and C correspond to different plate thicknesses, and reversely, they can be used to resolve thickness. In each group, there are four distinct dispersion curves which correspond to different temperatures. These dispersion curves can be used to determine temperature. However, dispersion variations due to the pressure effect are too insignificant to be differentiated.

The intersections of dispersion curves in Groups B and C are not supposed to happen. By comparing the dispersion curves extracted from Position 1 (Fig. 6.72) with those extracted from Position 2 (Fig. 6.73), it can be concluded that the aforementioned discrepancy is the result of numerical errors. There are no intersections in either of the single-point dispersion curve and individual dispersion curves are easily identified. The errors are believed to be from calculating the wave group velocity using Eq. (6.2).

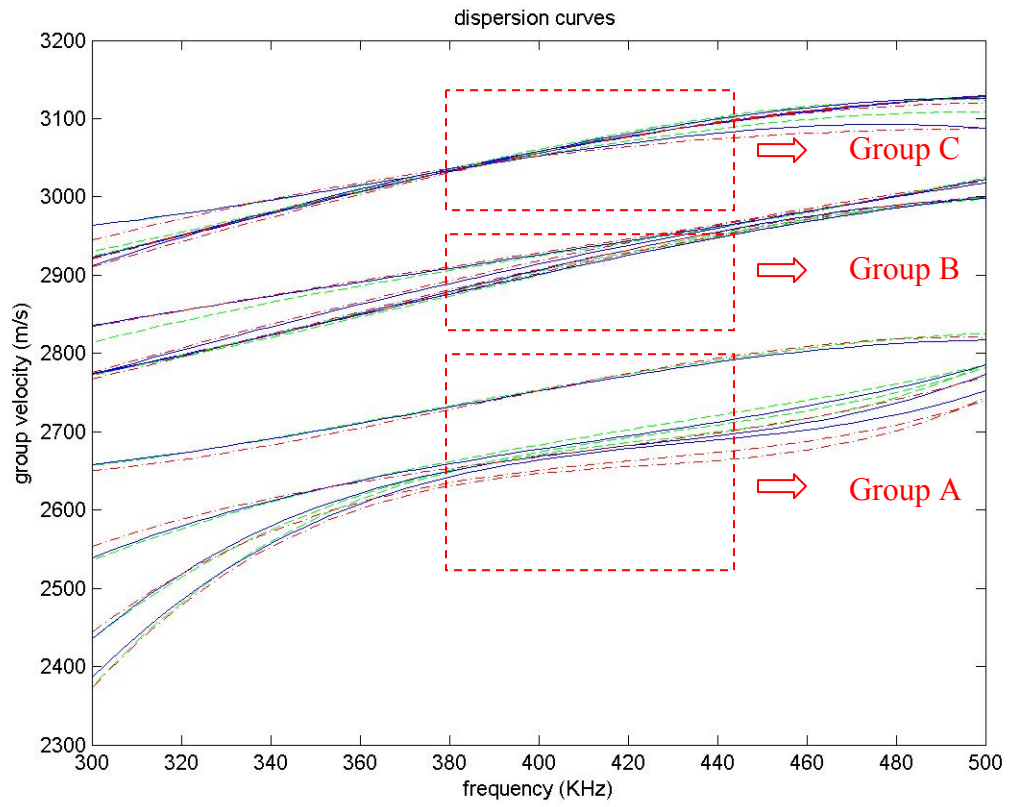


Fig. 6.71. All 36 dispersion curves extracted from both positions 1 and 2

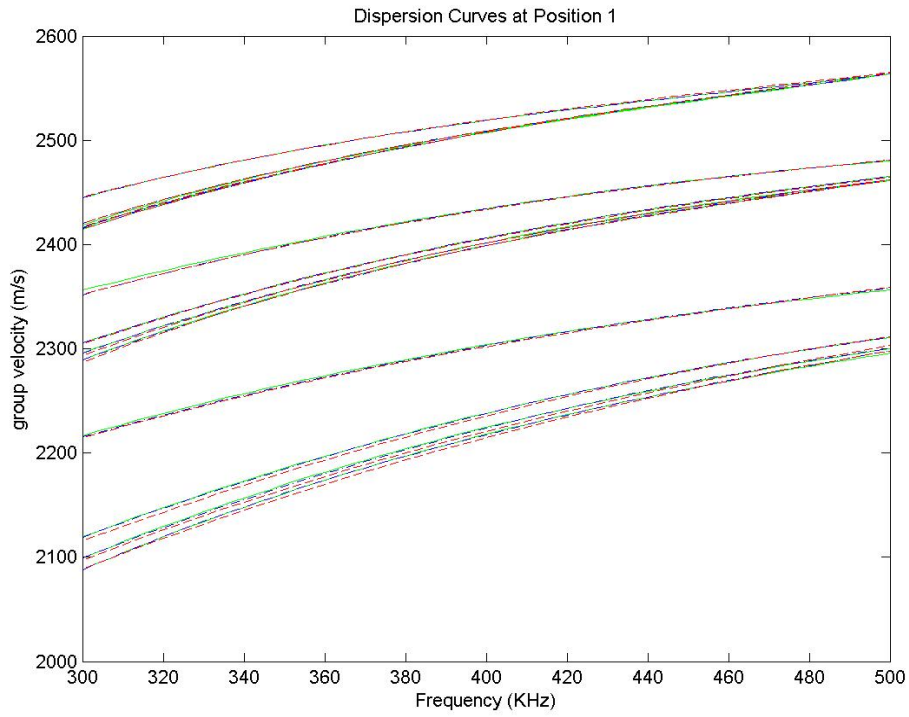


Fig. 6.72. All 36 dispersion curves extracted position 1 only

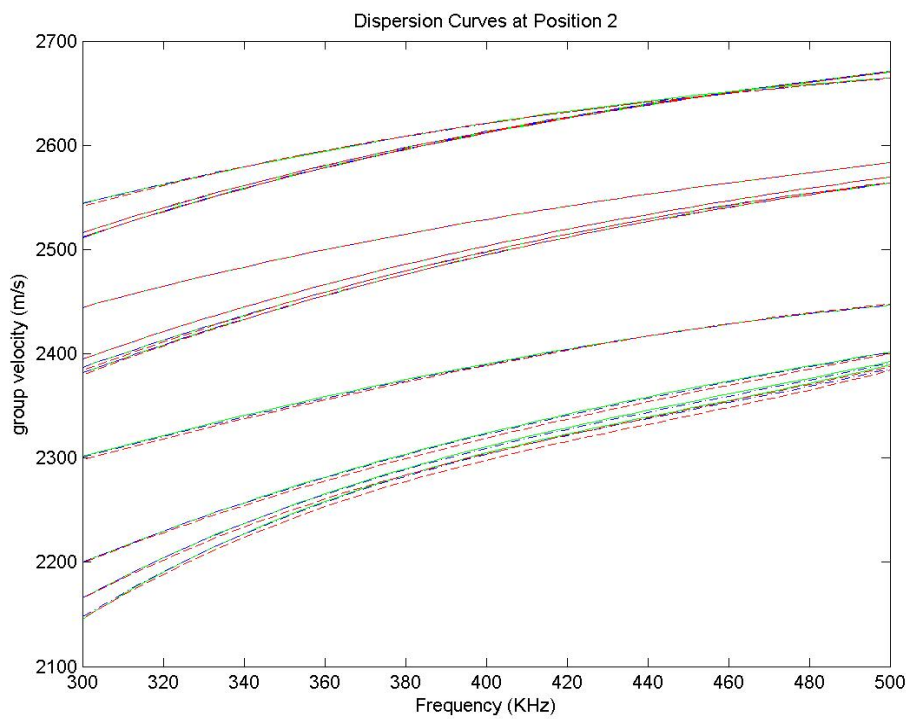


Fig. 6.73. All 36 dispersion curves extracted position 2 only

6.9. Summary

Using the model for modified wave propagation theory, numerical waveforms were successfully generated using the finite element method. All generated waveforms demonstrated higher sensitivity to temperature and thickness than to pressure. By applying Gabor Wavelet Transform to the numerical waveforms, dispersion curves corresponding to various mechanical, thermal and geometric conditions were successfully extracted. Availability of different dispersion curves as shown in Fig. 6.71 renders feasible the simultaneous determination of temperature, pressure and plate thickness.

The parameter range considered for the study was 300-500kHz for frequency, 25-300°C for temperature, 1-3mm for plate thickness and 1-10MPa for pressure. Three conclusions can be made from the resulted time waveforms and dispersion curves subject to these parameter ranges. The first is that smaller the plate thickness, more prominent of dispersion curve shift under the action of pressure. Frequency group velocity decreases with increasing pressure. The second is that thinner the plate, more significant the shift of dispersion curve due to thermal effect. Frequency group velocity increases with increasing temperature. The third is that thicker the plate, faster the group velocity. Since pressure, temperature and plate thickness were seen to affect wave dispersion, information about pressure, temperature and plate thickness can then be determined from dispersion curves. And, when plate thickness is over 1mm, it would be difficult to resolve pressure as wave dispersion becomes insensitive to pressure effects.

CHAPTER VII

CONCLUSIONS AND FUTURE WORK

The primary objective of the research was to create a new sensor concept for the simultaneous measurement of pressure, temperature and plate thickness without contacting or destructing the object being measured. To meet this need, Thermal–Acoustic-Photonic Nondestructive Evaluation (TAP-NDE) was adopted for the sensor design which employs a pulsed laser for dispersive plate wave generation and an optical interferometry known as FTI for wave sensing. By exploring the dispersion characteristics of propagating plate waves, pressure, temperature and thicknesses information of the plates through which the waves propagate can be resolved.

A theoretical analysis was performed to validate the new sensor concept and a modified wave propagation theory that considers pre-stress and temperature effects was formulated. The fundamental elasticity theory and classical wave propagation theory were the basis for deriving the modified theory. Using the modified wave propagation theory, a comprehensive 2D model applicable to linear elastic, homogeneous materials was developed. Since the governing differential equations of the model were too complex to render analytical solutions, FEM numerical procedures were instead attempted using the commercially available FEMLAB package. Numerical waveforms were successfully obtained for each parameter case considered. To extract dispersion curves from numerical waveforms, A Gabor Wavelet Transform (GWT) computer code was developed to resolve simultaneous time-frequency information. The code enabled the extraction of dispersion curves corresponding to three different pressures, four different temperatures and three different plate thicknesses. The differences in dispersion curves allow pressure, temperature and thickness to be established.

A new conceptual sensor body design was also created. This design integrated the wave generation and sensing components of TAP-NDE. Experimental investigation can be conducted through realizing this conceptual sensor body design.

All obtained dispersion curves were shown in Fig. 6.71. It was shown that dispersion curves are strong functions of plate thickness, followed by temperature and then lastly by

pressure, thus indicating that the three parameters considered in the study each have a different level of impact on plate wave dispersion. Within the parameter ranges considered for the investigation, i.e., 300-500kHz for frequency, 25-300°C for temperature, 1-3mm for plate thickness, and $1 \times 10^6 - 1 \times 10^7$ N/m for pressure, three conclusions were drawn from the extracted dispersion information. The first is that smaller the plate thickness, more prominent the pressure effect on wave dispersion. The frequency group velocity within this context was seen to decrease with increasing pressure. The second conclusion is that smaller the plate thickness, more sensitive dispersion curves are to temperature effect. The frequency group velocity within this context was seen to increase with increasing temperature. The third is that thicker the plate, faster the frequency group velocity. Results obtained for the research showed that plate wave dispersion can be correlated with pressure, temperature and plate thickness. Thus, proper information available from the dispersion curves can be used to determine the pressure, temperature, and thickness a thin plate are subjected to. It was also observed that when plate thickness is larger than 1mm, pressure effects are hard to be differentiated using dispersion curves.

Contributions of the thesis are many. First, the research provides a new non-contact, non-destructive sensor concept viable for multi-parameter measurement. Second, the research formulates a modified wave propagation theory along with its associated numerical model for studying plate wave dispersion subject to simultaneous thermal, mechanical and spatial effects. Third, the research also presents a new conceptual sensor body design. Availability of the results obtained and conclusions made in the research provides the necessary knowledge base for the design and development of multi-purpose sensors in the future.

Although the research has realized a multi-purpose sensor concept capable of simultaneous measurement of pressure, temperature and thickness in a non-contact fashion, however, more works are still needed. Since interrogating waves are initiated using a pulsed laser, the waves are fundamentally thermal-mechanical waves. Since the wave formulation derived for the research does not consider the influences of rapid, localized heating on plate wave propagation, investigation into establishing the impact of thermal wave propagation on plate wave dispersion is needed. Second, the heating of

high-power pulsed laser can cause extreme temporal and thermal gradients in the immediate proximity of the area of excitation. If and how these gradients would impact plate wave propagation and wave dispersion need be understood. Finally, experimental investigations need be conducted to validate the theoretical groundwork and the sensor concept developed in the thesis.

REFERENCES

- [1] J.D. Achenbach, Modeling for quantitative non-destructive evaluation, *Ultrasonics* 40 (2002) 1-10.
- [2] V.K. Varadan, V.V. Varadan, Microsensors, microelectromechanical systems (MEMS), and electronics for smart structures and systems, *Smart Material Structure* 9 (2000) 953-972.
- [3] C.S. Suh, G.A. Rabroker, C.P. Burger, R. Chona, Ultrasonic time-frequency characterization of silicon wafers at elevated temperatures, 1997 ASME Proceedings of Applications of Experimental Mechanics to Electronic Packaging, (1997) 37-43.
- [4] C.S. Suh, G.A. Rabroker, R. Chona, C.P. Burger, Lamb wave propagation as a temperature diagnostic in silicon wafer processing: Experimental Implementation and results, Proceedings of the 1998 SEM Spring Conference on Experimental Mechanics, (1998) 455-458.
- [5] C.S. Suh, G.A. Rabroker, R. Chona, C.P. Burger, Thermal-acousto-photonics for non-contact temperature measurement in silicon wafer processing, 1999 SPIE Proceedings of Optical Diagnostics for Fluids/Heat/Combustion and Photomechanics for Solids, (1999) 184-193.
- [6] D. Schneider, M.D. Tucker, Non-destructive characterization and evaluation of thin films by laser-induced ultrasonic surface waves, *Thin Solid Films* 290 (1996) 305-311.
- [7] D.M. Profunser, J. Vollmann, J. Dual, Determination of the material properties of microstructures by laser based ultrasound, *Ultrasonics* 42 (2004) 641-646.
- [8] I.C. Ume, and S. Liu, Vibration analysis based modeling and defect recognition for flip-chip solder-joint inspection, *Journal of Electronic Packaging* 124 (2002) 221-226.
- [9] C.P. Burger, T.D. Dudderar, J.A. Gilbert, B.R. Peters, J.A. Smith, B. Raj, Thermal acousto-optic excitation for non-contacting NDE, Proceedings of the 1986 SEM Spring Conference on Experimental Mechanics, (1986) 680-685.
- [10] C.P. Burger, N.A. Schumacher, C.E. Duffer, T.D. Knab, Fiber-optic techniques for generating and detecting ultrasonic waves for quantitative nde optics and lasers in engineering, *Optical and Lasers in Engineering*, 19 (1993) 121-140.
- [11] J. D. Achenbach, *Wave Propagation in Elastic Solids*, Elsevier, New York, 1976.
- [12] M. Kehlenbach, S. Das, Identifying damage in plates by analyzing Lamb wave propagation characteristics, *Proceeding of SPIE*, (2002) 364-375.
- [13] B.C Lee and W.J. Staszewski, Modelling of Lamb waves for damage detection in metallic structures: Part I. wave propagation, *Smart Materials and Structures* 12 (2003) 804-814.
- [14] M.Z. Silva, R. Gouyon, F. Lepoutre, Hidden corrosion detection in aircraft aluminum structures using laser ultrasonics and wavelet transform signal analysis, *Ultrasonics* 41 (2003) 301-305.

- [15] S.Y. Babich, A.N. Guz, Elastic waves in bodies with initial stresses, *Prikladnaya Mekhanika* 15 (4) (1979) 3-23.
- [16] J.F. Chai, T.T. Wu, Determination of surface wave velocities in a pre-stressed anisotropic solid, *NDT&E International* 29 (5) (1996) 281-292.
- [17] G.A. Rogerson, J.G. Murphy, Surface waves in slightly compressible, finitely deformed elastic media, *Mechanics Research Communications* 25 (5) (1998) 493-502.
- [18] D.A. Prikazchikov, G.A. Rogerson, On surface wave propagation in incompressible, transversely isotropic, pre-stressed elastic half-spaces, *International Journal of Engineering Science* 42 (2004) 967-986.
- [19] C.K. Chui, *An Introduction to Wavelets*, Academic Press, San Diego, CA, 1992.
- [20] K. Kishimoto, H. Lnoe, Time frequency analysis of dispersive waves by means of wavelet transform, *Journal of Applied Mechanics* 62 (1995) 841-846.
- [21] C.S. Suh, Numerical modeling of laser acoustic waves using finite element method and fast integral wavelet transform, Ph.D. dissertation, Texas A&M University, May 1997.
- [22] M.E. Baltazar-Lopez, application of TAP-NDE technique to non-contact ultrasonic inspection in tubulars, Ph.D. dissertation, Texas A&M University, December 2003.
- [23] V. Vedantham, In-situ temperature and thickness characterization for silicon wafers undergoing thermal annealing, M.S. thesis, Texas A&M University, August 2003.
- [24] W.S. Slaughter, *The Linearized Theory of Elasticity*, Birkhäuser, Boston, 2002.

VITA

Tzu-Wei (George) Lo was born on August 28, 1977 in Kaohsiung City, Taiwan. He is the son of Cheng-Jung Lo and Su-Kui Wang. He was an engineering student at Chang Gung University, Tao-Yuan, Taiwan, from which he received a B.S. in Mechanical Engineering in August 2000. After college, he went into mandatory military service and served for two years till May 2002 when he was honorably discharged. He joined Texas A&M University in January 2003, pursuing his Master of Science degree in Mechanical Engineering under the supervision of Dr. Chii-Der S. Suh. His research interests include mathematical and numerical modeling, dynamics and nondestructive evaluation (NDE) sensor design. Tzu-Wei Lo's permanent address is No. 18, Lane 599, Houchung Rd., Tzuoying Chiu, Kaohsiung, Taiwan.